2015

Design and synthesis of binary and ternary copper chalcogenide nanostructures for energy conversion

Xinqi Chen
University of Wollongong, xc067@uowmail.edu.au

DESIGN AND SYNTHESIS OF BINARY AND TERNARY COPPER CHALCOGENIDE NANOSTRUCTURES FOR ENERGY CONVERSION

This thesis is presented as part of the requirements for the award of the Degree of

DOCTOR OF PHILOSOPHY

From the

UNIVERSITY OF WOLLONGONG

By

XINQI CHEN, B. Sc., M. Sc., PhD Sc.

Institute for Superconducting and Electronic Materials

Faculty of Engineering and Information Sciences

September, 2015

CERTIFICATION

I, Xinqi Chen, declare that this thesis, submitted in fulfilment of the requirements for the award of Doctor of Philosophy, in the Institute for Superconducting and Electronic Materials, Faculty of Engineering and Information Sciences, University of Wollongong, is wholly my own work unless otherwise referenced or acknowledged. This document has not been submitted for qualifications at any other academic institution.

Xinqi Chen

September, 2015

ACKNOWLEDGEMENTS

Firstly, I would like to express my special appreciation to the China Scholarship Council for providing me with the opportunity and financial support to study at the University of Wollongong as a PhD candidate.

I would like to express my gratitude to my supervisors Prof. Shi Xue Dou and Prof. Zhen Li, for academic guidance, financial support, and constant encouragement during my study. I specially thank Prof. Zhen Li for supervising the experimental details and discussing academic writing.

I must acknowledge all the staff and technicians at the Institute for Superconducting and Electronic Materials (ISEM) and the Australian Institute for Innovative Materials (AIIM), including Prof. Hua Kun Liu, Prof. Xiao Lin Wang, Prof. Zai Ping Guo, A/Prof. Zhen Xiang Cheng, A/Prof. Alexey Pan, A/Prof. Jia Zhao Wang, Dr. Germans Peleckis, Dr. Tania Silver, Dr. Qiao Sun, Dr. Dong Qi Shi, Dr. Jian Li Wang, Dr. Sima Yamini, Dr. Kosta Konstantinov, Dr. Shu Lei Chou, Dr. Zi Qi Sun, Dr. Yi Du, Dr. Zhen Guo Huang, Dr. Xun Xu, Dr. Yun Zhang, Mrs. Crystal Mahfouz, Mrs. Narelle Badger, Ms. Joanne George, Dr. Candace Gabelish, Mr. Tony Romeo, Dr. Gilberto Casillas-Garcia, Mr. Mitchell Nancarrow, Dr. David Mitchell, Dr. David Wexler, Prof. Will Price, Mr. Paul Scully, and others for their kind assistance. Also, I am grateful to Prof. Lian Zhou Wang and Dr. Yang Bai for their collaboration and measurements at the University of

Queensland.

I would like to thank all the group members in Prof. Zhen Li’s group and fellow colleagues at ISEM, including Mr. Chao Han, Mr. Shao Hua Zhang, Ms. Jin Yan Xiong, Ms. Li Juan Zhang, Dr. Dan Li, Dr. Yun Xiao Wang, Ms. Xin Liang, Dr. Jian Ping Yang, Mr. Teng Fei Zhou, Dr. Qin Jun Chen, Dr. Anne Yonamine, Dr. Sara Dafe, Dr. Tomas Katkus, Dr. Victor Malgras, Dr. Igor Golovchaskiy, and others, for their generous help and friendship.

Finally, I would like to express my appreciation and love to my family, especially my parents and my husband, for their strong support, love, and understanding.

TABLE OF CONTENTS

LIST OF FIGURES

LIST OF TABLES

LIST OF SPECIAL NAMES

Symbol	Name	Unit
η	Efficiency	%
ΔG	Gibbs free energy	kJ mol^{-1}
S	Seebeck coefficient	μV K^{-1}
σ	Electrical conductivity	S cm^{-1}
κ	Thermal conductivity	W K^{-1} m^{-1}
T	Absolute temperature	K
d	Lattice spacing	m
λ	Wavelength	Å
θ	Diffraction angle	°
β	Half-peak width	°
D	Thermal diffusivity	m^2 s^{-1}
C_p	Heat capacity	J kg^{-1} K^{-1}
$\rho(2.4.2)$	Mass density	g ml^{-1}
K_{sp}	Solubility	Null
$\rho(4.3.5)$	Electrical resistivity	Ω·m
μ	Carrier mobility	cm^2 V^{-1} s^{-1}
n	Carrier concentration	cm^{-3}

e	Charge of the electron	Null
k	Boltzmann's constant	Null
r	Scattering factor	Null
N_0	Avogadro constant	Null
$E_{nanowire\text{-}ligand}$	Total energy of each complex	eV
$E_{nanowire}$	Energy of the isolated Cu NW	eV
E_{ligand}	Energy of selenothiolate (or thiosulphide)	eV
pK_a	Symbol for the acid dissociation constant at logarithmic scale	Null
V_{oc}	Open-circuit voltage	mV
FF	Fill factor	%
J_{sc}	Short-circuit current density	mA cm^{-2}
R_s	Series resistance	Ω
R_{ct}	Charge transfer resistance	Ω
Z_w	Warburg diffusion impedance	Ω
R	Gas constant	Null
F	Faraday constant	Null
L (5.3.8)	Spacer thickness	nm
C (5.3.8)	Sulfide concentration	mol L^{-1}
$\Delta_f H^0$ *(6.3.3)*	Enthalpy	kJ mol^{-1}

LIST OF ABBREVIATIONS

Abbreviation	Full name
a.u.	Arbitrary unit
BEs	Binding energies
BET	Brunauer-Emmett-Teller
BSE	Back-scattered electrons
CEs	Counter electrodes
CL	Cathodoluminescence
DSC	Differential scanning calorimetry
DNP	D-polarization functions
DSSCs	Dye-sensitized solar cells
EDS/EDX	Energy dispersive x-ray spectroscopy
EIS	Electrochemical impedance spectroscopy
fcc	Face centered cubic
FE-SEM	Field-emission scanning electron microscopy
FFT	Fast Fourier transform
FTO	Fluorine-doped tin oxide
HRTEM	High-resolution transmission electron microscopy
ICP-AES	Inductively coupled plasma − atomic emission spectroscopy
ICP-OES	Inductively coupled plasma − optical emission spectrometry
IPCE	Incident photon-to-current conversion efficiency
ITO	Tin-doped indium oxide
J-V	Photocurrent-voltage

LST/QST	Linear synchronous transit/quadratic synchronous transit
NIR	Near-infrared
NTs	Nanotubes
NWs	Nanowires
ORR	Oxygen reduction reaction
PEM	Proton exchange membrane
PF	Power factor
QDSSCs	Quantum-dot-sensitized solar cells
SAED	Selected area electron diffraction
SBE	Back-scattered electrons
SDS	Sodium dodecyl sulfate
SE	Secondary electrons
SEI	Secondary electron imaging
SEM	Scanning electron microscopy
SPS	Spark plasma sintering
TAA	Thioacetamide
TE	Thermoelectric
TEM	Transmission electron microscopy
TGA	Thermogravimetric analysis
TMCs	Transition metal chalcogenides
TOP	Trioctylphosphine
TOPO	Trioctylphosphine oxide
UV-vis	Ultraviolet-visible spectroscopy
XPS	X-ray photoelectron spectroscopy

XRD	X-ray diffraction
0D	Zero-dimensional
1D	One-dimensional
2D	Two-dimensional
3D	Three-dimensional

ABSTRACT

Energy conversion is one of the attracted research topics in recent years because solving energy crisis becomes an urgent task. As one of the transition metal chalcogenides (TMCs), copper chalcogenides are found in broad applications in energy conversion and storage and other areas. In order to enhance their favorable properties, a number of techniques and strategies have been developed to prepare different nanostructured copper chalcogenides. Nevertheless, the design and synthesis of hierarchical architectures for copper chalcogenides to enhance their performance in the areas mentioned above is still a challenge.

This thesis is devoted to the design and synthesis of binary and ternary copper chalcogenides in energy conversion applications related to thermoelectric conversion and Quantum-dot-sensitized solar cells (QDSSCs). Copper selenide, a *p*-type semiconductor with high electrical conductivity, low thermal conductivity, and changeable crystal structure has been explored as a thermoelectric conversion material. Most synthesis methods, however, (i.e., high-temperature solid state reaction method, ball milling, hydrothermal/solvothermal method) are not able to produce morphology-controlled and large-scale samples for thermoelectric research. Thus, a facile synthesis of copper selenide on a large scale with controlled morphology is desirable. This research aimed at the large-scale synthesis of surfactant-free copper selenide ($Cu_{2-x}Se$) nanostructures and

the thermoelectric properties of these $Cu_{2-x}Se$ nanostructures sintered by the spark plasma sintering (SPS) technique. Firstly, an aqueous route was developed to prepare the uniform and surfactant-free $Cu_{2-x}Se$ NWs. The effects of reaction parameters such as the Cu/Se precursor ratio, the Se/NaOH ratio, and the reaction time on the formation of NWs were comprehensively investigated. The results show that $Cu_{2-x}Se$ NWs were formed through the assembly of CuSe nanoplates, accompanied by their self-redox reactions. The resultant $Cu_{2-x}Se$ NWs were explored as a potential thermoelectric candidate in comparison with commercial copper selenide (Cu_2Se) powder.

Another facile and high yield fabrication method for $Cu_{2-x}Se$ nanostructure has been addressed. Grams of $Cu_{2-x}Se$ nanostructures were prepared from commercial copper and selenium powders in the presence of thiol ligands by a one-pot reaction at room temperature. The morphology of the nanostructures is strongly dependent on the ratio of thiol ligand to selenium powder. The resultant $Cu_{2-x}Se$ nanostructures were treated with hydrazine solution to remove the surface ligands and then explored as a potential thermoelectric candidate in comparison with commercial copper selenide powders. The results demonstrate that the synthetic samples from our novel approach exhibit similar thermoelectric properties to commercial Cu_2Se, which is similar to the result in the previous chapter, although $Cu_{2-x}Se$ retained its cubic structure, while commercial Cu_2Se was converted to a mixture of cubic and tetragonal structures after high-temperature measurement, so that the resultant $Cu_{2-x}Se$ has a more stable crystal structure than

commercial Cu_2Se.

These two parts of work indeed provide simple ways to prepare large-scale copper selenide nanostructures for thermoelectric applications. Nano grains clearly play an important role in reducing lattice thermal conductivity, by enhancing phonon scattering. In addition, the Cu-deficiency in $Cu_{2-x}Se$ increased the electrical conductivity compared to that in commercial Cu_2Se. However, the reduction in thermal conductivity cannot exceed the concomitant reduction in the power factor caused by electronic carrier scattering, which cannot turn into enhanced *ZT*. Meanwhile, unavoidable small holes inside nanostructured materials decrease the density of pellet after SPS sintering, which might lead to overestimating *ZT* of materials.

In the QDSSC application, the conventional noble metal counter electrodes (CEs) (Pt or Au) are unsuitable for QDSSC applications when polysulfide electrolytes are used, mainly because sulfur-containing (S^{2-} or thiol) compounds are absorbed preferentially and strongly on the Pt or Au surface, leading to surface passivation and decreasing conductivity of the electrodes. In contrast, copper-chalcogenide-based CEs show lower resistance and higher electrocatalytic activity towards the redox reaction of polysulfide, thus improving the conversion efficiency of QDSSCs. Current investigations in this field are mainly focused on copper sulfide CEs, although, there have been few reports on binary copper selenide CEs and no reports on ternary copper silver selenide CEs in QDSSCs, especially involving designed nanostructures for enhancing the conversion

efficiency of the QDSSCs. Based on the previous mentioned synthesis method, $Cu_{2-x}E$ (E = S, Se) NTs with a hierarchical architecture were prepared and assembled as CEs for QDSSCs. $Cu_{2-x}Se$ and $Cu_{2-x}S$ NTs were fabricated by using Cu NWs, and stable sulfur or selenium powder as precursors at room temperature. The influence of the reaction parameters (e.g., precursor ratio, ligands, ligand ratio, and reaction time) on the formation of the nanotubes was comprehensively investigated. The resultant $Cu_{2-x}E$ (E = S, Se) NTs were used as CEs in QDSSCs to achieve a conversion efficiency (η) of 5.02 % and 6.25 %, respectively, much higher than that of QDSSCs made with Au CEs (η = 2.94 %).

After obtaining $Cu_{2-x}Se$ NTs as CE of QDSSC, one-dimensional/two-dimensional (1D/2D) ternary CuAgSe NTs were successfully prepared from the $Cu_{2-x}Se$ NTs at room temperature within a short reaction time by the facile cation exchange approach. The cation exchange leads to the transformation of the crystal structure from cubic to orthorhombic and/or tetragonal with good retention of morphology. The exchange reactions are spontaneous due to the large negative changes in the Gibbs free energy (ΔG). The effects of parameters such as reaction time, precursor source, and precursor ratio on the exchange reaction were investigated. The resultant CuAgSe NTs were explored as CEs of QDSSCs and achieved much higher conversion efficiency (η = 5.61 %) than those of QDSSCs containing the noble-metal Au CEs (3.32 %), which was due to the higher mobility of both Cu^+ and Ag^+ ions in the CuAgSe NTs and the higher

stability of metal selenides in polysulfide electrolyte by avoiding corrosion and passivation than that of the Au CEs.

CHAPTER 1 Introduction and Literature Review

1.1 Energy conversion

The energy crisis has become to a global issue because of the shortage of the fossil fuel resources and their harmful by-products and emissions. Searching for clean and renewable energy sources has been an urgent task. Solar cells, fuel cells, thermoelectric devices, and lithium-ion batteries are current alternative eco-friendly energy sources and energy storage systems. They all have owned advantages. (1) Solar cells: based on unlimited sunlight, solar energy is a clean and renewable source of energy because of 1 hour of sunlight striking the earth equals the whole world's current annual energy consumption.[1] (2) Fuel cells powered by hydrogen and oxygen from secure and renewable sources are non-polluting, and extensive research on them has delivered prototype cars with impressive performances.[2] (3) Thermoelectric conversion (direct conversion of thermal energy to electrical energy and vice versa), a kind of all solid-state energy conversion, not only has recycled waste heat from factories or vehicles in motion, but also absorbed heat from the sun as a complementary device of solar cells.[3-5] (4) Lithium-ion batteries are rechargeable devices based on electricity, in which lithium ions move from the negative electrode to the positive electrode during discharge and back when charging.[6] Lithium-ion batteries are becoming a common replacement for the lead acid batteries in some utility vehicles. Recently, sodium-ion batteries have been under

development to partially replace lithium-ion batteries due to their low cost.

Energy exists in many forms: some of them may be used directly in natural processes (e.g., light or heat) or transformed into other forms for use in another aspect, such as in refrigeration or producing electricity. This process of changing one form of energy to one other is called energy conversion. For example, thermoelectric material devices can transform thermal energy into electrical energy. A solar cell converts the radiant energy of sunlight into electrical energy.

1.1.1 Thermoelectric conversion

The thermoelectric conversion is the direct conversion of heat into electricity and vice versa, and the driving force is the temperature difference between hot side and cold side of thermoelectric couples.[7] The discovery of this effect has been attributed to Thomas Johann Seebeck[8] who published his first observations on what he called then thermomagnetism in 1821.[9] This effect can be used to generate electricity, measure temperature, or change the temperature of objects. The term “thermoelectric effect” encompasses three separately identified effects: the Seebeck effect, the Peltier effect, and the Thomson effect.[7]

(1) Seebeck effect

The Seebeck effect is the direct conversion of temperature differences into electricity. Initially, this effect was discovered from the phenomenon that a closed loop would deflect a compass needle. This closed loop is formed by two joined pieces of different

metals with a temperature difference between the junctions.[7] The reason for this phenomenon was that the temperature difference induces the metals to respond in different ways, which creates a current in the circuit and a magnetic field.

(2) Peltier effect

The Peltier effect refers to the generation of cooling or heating. Jean Charles Athanase Peltier, in 1834, observed that when an electrical current passes through the junctions of a circuit composed of two different conductors, these junctions absorb or release heat. In a closed loop, charge carriers transport heat from one junction (cooling) to the other (heating) because they drift under the imposed electromotive force.

(3) Thomson effect

The Thomson effect describes the heating or cooling of a current-carrying conductor that is exposed to a temperature gradient. In 1851, William Thomson (Lord Kelvin) predicted and subsequently observed this effect. The three thermoelectric effects are connected: a gradient in the Seebeck coefficient might result from a spatial gradient in temperature, which is due the variation of the Seebeck coefficient with temperature. A continuous version of Peltier effect will occur when a current is generated through this gradient.

The thermoelectric effect encompasses more than one of the above effects in a consistent and rigorous way, which can be shown by thermoelectric materials in a strong or convenient form. Thermoelectric materials are semiconductors with high electrical

conductivity and low thermal conductivity that can directly convert thermal energy into electricity in the presence of a temperature difference.[5] The energy conversion efficiency of thermoelectric technology is mainly limited by the materials' performance, as described by the dimensionless thermoelectric figure of merit, *ZT*.

$$ZT = \frac{S^2 \sigma T}{\kappa} \tag{1.1}$$

where *S* is the Seebeck coefficient, σ is the electrical conductivity, κ is the thermal conductivity, and *T* is the absolute temperature.[4,10-11] Thermoelectric generator module, a device that converts thermal energy into electric energy directly, consists of many *n*-type and *p*-type semiconductor materials cuboids connecting electrically in series and thermally in parallel. This whole system is mounted between two ceramic plates, which not only supports and contains the structure mechanically but also provides electrical insulation for the individual elements from external mounting surfaces (Figure 1.1). In the presence of a heat gradient on the surface of a thermocouple, charge carriers tend to migrate from the hot side towards the cold side. At the *n*-type leg, the flow of electrons results in the current flowing from the cold side to the hot side. This movement of the electron flow causes a negative charge built up on the cold side. At the *p*-type leg, the migration of the holes results in the current flowing from the hot end to the cold end. As a consequence, a positive charge builds up occurs on the cold side. A current can be observed in an external circuit by connecting the two junctions through a metallic interconnect.

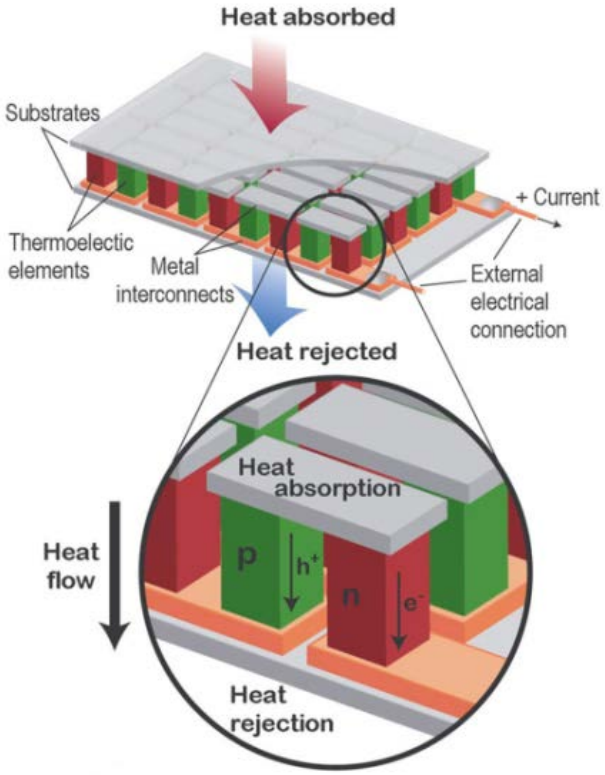

Figure 1.1 Thermoelectric generator module.[12]

1.1.2 Solar energy

A solar cell is an electrical device that converts the radiant energy of sunlight into electrical energy. A solar cell generates electric power from both the current and voltage producing by light irradiation. To achieve this conversion, the semiconductor materials in solar cell absorb light and raise inner electrons to higher energy states, and these higher energy electrons move to an external electronic loop, in which they dissipate energy and return to the solar cell. Generally, many materials and processes can achieve this energy conversion theoretically, although most photovoltaic devices are based on semiconductor

materials in the form of a *p-n* junction.[13]

Quantum-dot-sensitized solar cells (QDSSCs) are a type of solar cell that uses quantum dots as the absorbing photovoltaic material, which is a promising non-toxic upgrade from the dye-sensitized solar cells (DSSCs) and low-cost alternative to existing crystalline silicon solar cells and thin inorganic films solar cells. A whole QDSSC consists of four parts: photoelectrode, quantum dots (QDs), an electrolyte, and a counter electrode (CE) [Figure 1.2 (a)]. The photoelectrode commonly uses mesoporous oxide film like TiO_2 or ZnO film because they have a wide band gap. QDs can be semiconductor nanocrystals such as CdS, CdSe, CdTe, $CuInS_2$, Cu_2S, PbS, PbSe, InP, InAs, Ag_2S, Bi_2S_3, and Sb_2S_3 and work as a sensitizer.[1] One outstanding advantage of QDSSCs is that the band gaps of QDs are tunable across a wide range of energy levels by controlling their size with low-cost producing methods.[1] The electrolytes contain iodide/triiodide or S^{2-}/S_n^{2-} redox couples. CEs are noble metals like Au or Pt. As reported by Tian at al. [Figure 1.2 (b)]: "photons are captured by QDs, yielding electron-hole pairs that are rapidly separated into electrons and holes at the interface between processes employing S^{2-}/S_n^{2-} as the redox couple: (1) charge injection from an excited QD into TiO_2, (2) transport of electrons to the collecting electrode surface, (3) hole transfer to the redox couple, (4) regeneration of the redox couple, (5) recombination of electrons from the QD and the oxidized form of the redox couple, and (6) interfacial recombination of electrons from TiO_2 and the oxidized form of the redox couple."[14]

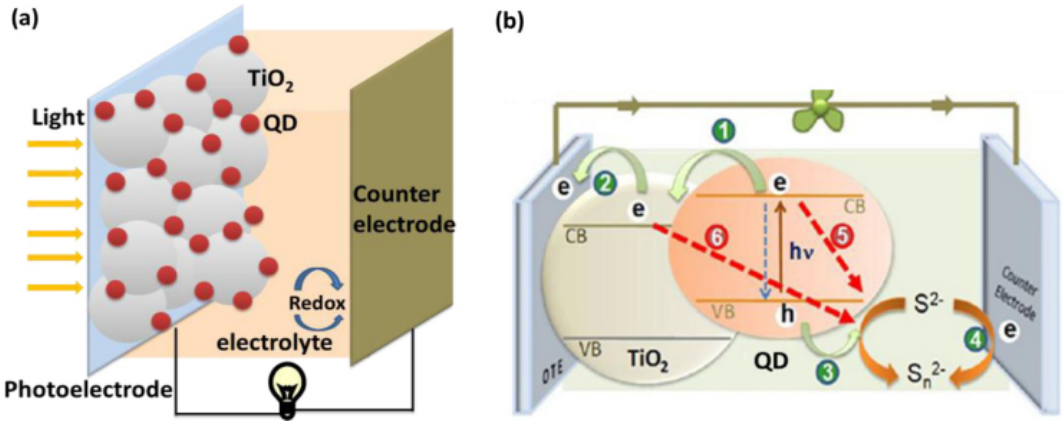

Figure 1.2 (a) Schematic illustration of the structure of a QDSSC; and (b) schematic illustration of photoinduced charge transfer processes following a laser pulse excitation.[14]

1.1.3 Other forms of energy conversion

Fuel cells can convert chemical potential energy (energy stored in molecular bonds) into electrical energy. Compared to conventional technologies such as internal combustion engines, they enhance conversion efficiency (50%−60% to ~35%). So they are attractive for a variety of applications ranging from portable to automotive to stationary power.[15] At the current stage, hydrogen gas (H_2) and oxygen gas (O_2), the recyclable elements, have been used as fuel in Proton Exchange Membrane (PEM) cells. The products after the reaction in the cell are electricity and heat, and the by-product is non-toxic water (Figure 1.3). The equations for the reaction are as follows:

Cathode: $O_2 + 4H^+ + 4e^- \rightarrow 2H_2O$ (1.2)

Anode: $2H_2 \rightarrow 4H^+ + 4e^-$ (1.3)

Overall: $2H_2 + O_2 \rightarrow 2H_2O$ (1.4)

In a PEM fuel cell, the anode, cathode, electrolyte, and catalyst are the four basic elements. Among these four elements, the catalyst is the most important part of the fuel cell, which is usually made of a very thin layer of platinum nanoparticles coated on a soft conductive substrate (i.e., carbon paper or cloth), which is rough and porous so that the maximum surface area of the platinum can be exposed to the hydrogen or oxygen.

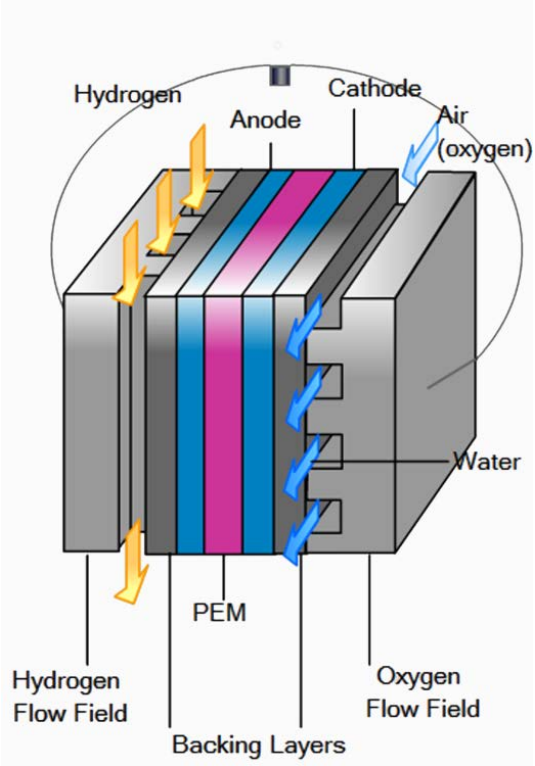

Figure 1.3 Unit cell cross section in a fuel-cell stack.[16]

Lithium-ion batteries, energy storage devices, can combine with other clean energy conversion devices for storing excess electric energy. A lithium-ion battery cell contains a cathode and an anode soaked in an electrolyte solution with dissociated salts, which enable ion move between the two electrodes. When the lithium-ion battery cell is

discharged, Li^+ ions are extracted by the anode, pass through the electrolyte and are inserted into the cathode, while at the same time, electrons flow from the anode to the cathode through the external circuit. The process is reversed during charging when an external voltage is applied to the battery (Figure 1.4). Since Li^+ ions shuttle between the two electrodes, the inherent properties of the electrode materials play a crucial role that determines the overall performance of batteries.

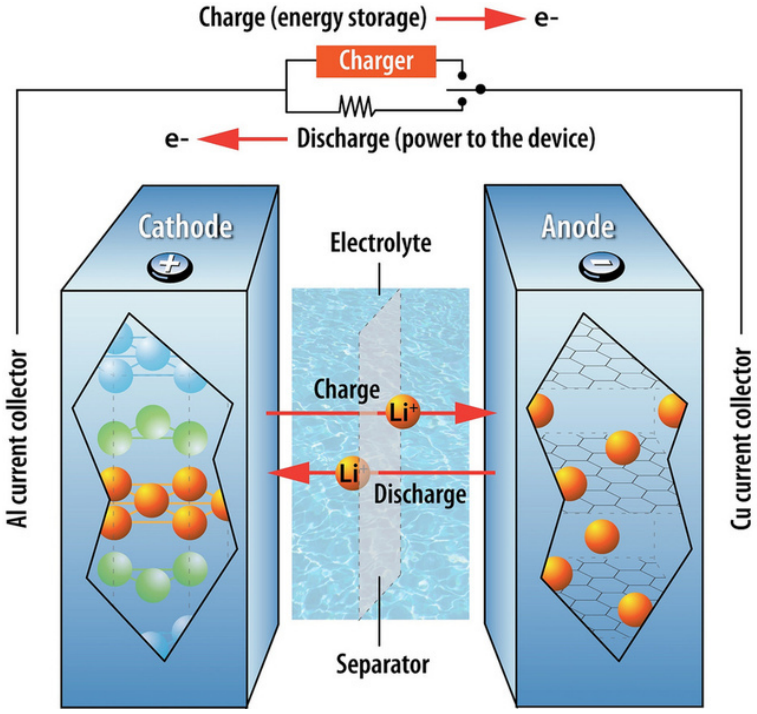

Figure 1.4 Structure of Lithium-ion battery.[17]

However, energy coming from the energy conversion and storage devices mentioned above occupies less than 1% of current average global primary power consumption.[15] In an economical aspect, renewable energy conversion devices cost massively on a large

scale. Meanwhile, low energy conversion efficiency is another restriction for extensive use. For example, “solar power currently provides only a very small fraction of global electric power generation and remains significantly more expensive than other electric power sources.”[15] Thus, the nanotechnology-based low-cost and high-performance energy conversion materials are paramount importance.

1.2 Properties and applications of transition metal chalcogenide nanostructures

To achieve improved function and efficiency, the introduction of nanomaterials and the connections between nanotechnology and energy need to be appreciated. Transition metal chalcogenide (TMC) nanostructures, as potential candidates, have revealed excellent performance in many green energy devices. They display many stoichiometries in various structures.[18] The simplest stoichiometry of metal to chalcogenides is 1:1 or 1:2. In metal-rich TMCs, there is extensive metal-metal bonding, while in chalcogen-rich TMCs, the material contains extensive chalcogen-chalcogen bonding.[19] In some cases, the chalcogenide is treated as a dianion (S^{2-}, Se^{2-}, or Te^{2-}). From their semiconducting properties, however, TMCs are highly covalent, not ionic.[18] As one of the TMCs, copper chalcogenide has attracted much attention due to its advantageous properties, environmental compatibility and low toxicity. Their suitable properties, especially in the copper-deficiency structures, and low cost have made copper chalcogenides and their

doped or ternary compounds promising candidates as sustainable energy materials, which have been investigated for various broad applications, including CEs for QDSSCs,[20-22] potential fuel cells due to their high electrocatalytic performance,[23] thermoelectric conversion materials,[24-25] electrodes for lithium-ion or sodium-ion battery,[26-27] and photothermal therapy[28-31].

1.2.1 Thermoelectric properties

Copper sulphides and copper selenides, well-known *p*-type semiconductors, have been studied for many years for applications of thermoelectric technology.[9,32] In recent years, they have displayed considerable performance in thermoelectric conversion. Liu at al. reported a *ZT* of 1.5 at 1000 K for undoped $Cu_{2-x}Se$ in the *β*-phase.[24] Another paper by Yu et al. reported a *ZT* of 1.6 at 700 °C achieved in *β*-phase Cu_2Se.[25] Recently, this *ZT* value of bulk $Cu_{2-x}Se$ was surpassed by Zhao et al. who demonstrated 1.7-1.8 at 973 K.[33] These high *ZT* values are attributed to the unique structure of $Cu_{2-x}Se$ with its face-centered cubic (fcc) crystal structure and structural symmetry corresponding to the $Fm\bar{3}m$ space group (Figure 1.5), in which the lattice frame of selenium atoms provide a pathway for movement of semiconducting electrons, and the highly disordered copper ions move through the selenium lattice frame with “liquid-like mobility”. This extraordinary and special structure of $Cu_{2-x}Se$ forms an intrinsically low lattice thermal conductivity, which can result in high *ZT* based on equation (1.1). So retaining the same properties at the Seebeck coefficient and the electrical conductivity, the lower total thermal conductivity is

good criteria for an ideal thermoelectric material. The results discover “a new strategy and direction for high-efficiency thermoelectric materials by exploring structures where a crystalline sublattice frames for electronic movement surrounded by liquid-like ions”.[34-36]

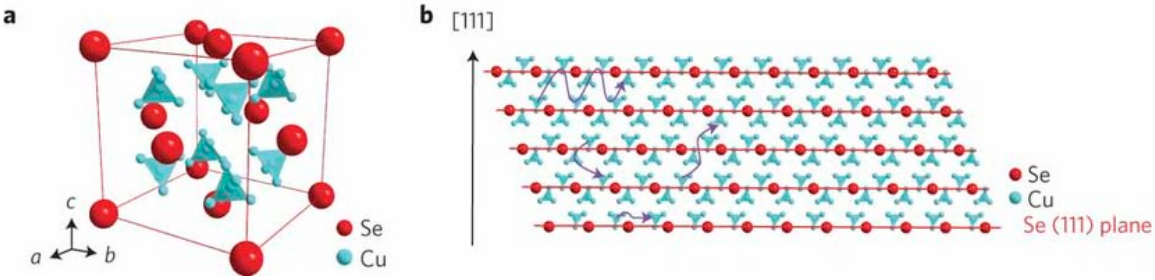

Figure 1.5 Crystal structure of Cu_2Se at high temperatures (β-phase) with a cubic anti-fluorite structure.[24]

1.2.2 Counter electrodes for quantum-dot-sensitized solar cells

Conventional CE materials in QDSSCs are Pt or Au, which are unsuitable electrocatalysts when polysulfide electrolytes are used, mainly because sulfur-containing (S^{2-} or thiol) compounds are absorbed preferentially and strongly at Pt or Au surface, leading to decreased surface activity and conductivity of the electrodes.[37-39] Compared with Pt or Au CEs, copper chalcogenide based counter electrodes with low resistance and high electrocatalytic activity towards the redox reaction of polysulfide can enhance the conversion efficiency of QDSSCs,[20,38,40] which has been confirmed by examples of CuS/CoS CE boosting the conversion efficiency of CdS/CdSe QDSSCs to 4.1% in contrast to Pt CE (3.0%) and a CuS nano-pea film CE revealing remarkable higher conversion efficiency of 4.01% compared to Pt with 1.07%.[41-42] Furthermore, the

morphology of copper chalcogenide in assembled CEs also influences the conversion efficiency of QDSSCs. A 3-Dimensional (3D) skeletal Cu_7S_4 nanocages CE exhibited a conversion efficiency of 4.43% under 1 sun (100 mW cm^{-2}) irradiation in CdS/CdSe QDSSCs, higher than those of QDSSCs made with preformed 18 facet-Cu_7S_4 and Pt CE.[43] Core–shell nanowire (NW) arrays with tin-doped indium oxide (ITO) nanowire cores and Cu_2S nanocrystal shells (ITO@Cu_2S) increased the power conversion efficiency of QDSSCs by 84.5 and 33.5% compared to those with planar Au and Cu_2S CEs, respectively (Figure 1.6) because of the improvement in charge collection and transport in this 3D structure of NW arrays.[20] Both these two structures provided a higher surface area for more active catalytic sites and easy accessibility for an electrolyte, which then resulted in better performance. The composition-dependent electrocatalytic activity of Cu_xS with tunable stoichiometry has been investigated. The results demonstrated that the ratios of Cu:S influenced the electrocatalytic activity of samples, in which the performance of different Cu_xS CEs was in the order of CuS > $Cu_{1.12}S$ > $Cu_{1.75}S$ > $Cu_{1.8}S$.[44] As analogues of copper sulphide ($Cu_{2-x}S$, $0 \leq x \leq 1$), copper selenide ($Cu_{2-x}Se$, $0 \leq x \leq 1$) compounds has been expected to display similarity in this field. In recent reports, $Cu_{1.8}Se$ and Cu_xSe were also found to be chemically stable with a polysulfide electrolyte and were even better than Cu_2S as CE material for QDSSCs. The power conversion efficiency is 5% and 3.8% for CdS/CdSe QDSSCs, respectively, when using the $Cu_{1.8}Se$ CE.[21-22] The better performance and lower cost of copper chalcogenides make them

alternative CEs to the noble metal Pt and Au analogues used in QDSSCs. Apart from being CEs for QDSSCs, $Cu_{2-x}Se$ can be a candidate for some optoelectronics devices or photodetectors because $Cu_{2-x}Se$ films made from its nanocrystals exhibited a 12.6-times increase in detection current between light and dark.[45]

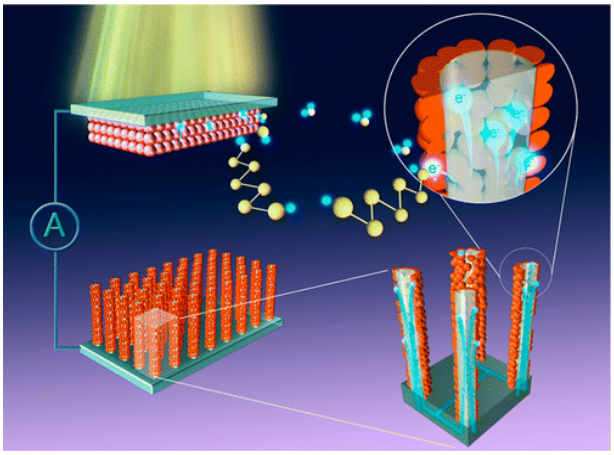

Figure 1.6 Core-shell NW arrays with tin-doped indium oxide (ITO) NW core and Cu_2S nanocrystal shell (ITO@Cu_2S) as new efficient CEs for QDSSCs.[20]

1.2.3 Electrocatalytic performance for fuel cells

One strategy for promoting utilization of fuel cells and decreasing the cost of production is exploring and synthesizing non-Pt electrocatalysts. Cu_2Se nanostructures are expected to possess good electrocatalytic activity towards the Oxygen Reduction Reaction (ORR) because of the mixture of Cu^+ and Cu^{2+} valence and the good ORR catalytic performance of some Cu-based nanostructures (e.g., Cu_3N nancubes[46] and Cu_2O nanocrystals[47]) in alkaline electrolyte. A recent report has demonstrated that the catalytic activity and stability show much better in the tetragonal phase of Cu_2Se NWs than in the

cubic phase. Moreover, this catalytic performance in tetragonal phase Cu_2Se NWs even can compare to or better than those of commercial Pd/C and some other recently reported non-Pt electrocatalysts.[23] This work also explores how phase structure can influence ORR performance.

1.2.4 Electrodes for Li/Ni-ion battery

Beyond to above three types of energy conversion in devices, the lithium-ion battery has been applied in a broad range of devices from electronic equipment (e.g., cell phones and computers) to electrical vehicles due to its high energy density. Elements such as Co and Mn are usually used as electrodes in commercialized lithium-ion batteries, which are expensive for large-scale application. In order to reduce the cost, many materials with high electrical conductivity and suitable crystal structure for lithium ion migration have been investigated and developed for lithium-ion battery applications.[48-49] Cuprous oxides (Cu_2O) have been reported as anode materials with high capacity and good capacity retention in cycling.[50-53] CuO/Cu_2O hollow polyhedra with porous shells exhibited a reversible lithium storage capacity as high as 740 mA h g^{-1} at 100 mA h g^{-1} after 250 cycles.[50] For improvement of capacity, other morphologies of CuO or Cu_2O have been used as well. Fine CuO nanorods as anode material in a lithium-ion battery exhibited a high electrochemical capacity of 766 mA hg^{-1}.[51] Cu_2O nanorod arrays have also been used in lithium-ion batteries as anode and showed a capacity of 330 mA h g^{-1} after 100 cycles.[52] As belonging to the same group of compounds, copper sulphide and copper

selenide have also been reported in the lithium ion battery area. The liquid-like Cu ions in the fcc structure of copper chalcogenide, as mentioned previously, can provide high-speed ion mobilities and free vacancies for lithium ions migrate into/out of the compound. The superiority of the Li/CuS cathode battery, having a specific volumetric energy of 470 Wh dm^{-3} [greater than that can be obtained with the HgO/Zn battery of (350 Wh dm^{-3})] was been reported in 1972.[54] Most recently, copper sulfides with "copper excess" as anode material for lithium-ion batteries have shown high rate charge-discharge capability.[55] Copper selenides, $CuSe_2$, CuSe and Cu_2Se thin films have been successfully fabricated from mixed targets of Cu and Se, and utilized as cathode materials with capacities of 201.7 mA hg^{-1}, 258.4 mA hg^{-1}, and 210.2 mA hg^{-1}, respectively.[56] Unlike the Cu_2O, however, the application of CuS in lithium-ion battery is limited by irreversible recharge process. To avoiding this disadvantage, the array structure has been utilized due to its high transfer speed of electrons and the stability of the materials in the structure. For example, Cu_2S nanowire arrays have been fabricated on copper substrates as promising cathodes for lithium ion battery, with stable lithium ion insertion/extraction reversibility, high reversible lithium storage capacity, long life cycle, and outstanding cycling stability (Figure 1.7).[27] $Cu_{2-x}Se$-coated CuO NT arrays on a copper substrate displayed a high cycling capacity for 764 mA hg^{-1} after 100 cycles at a current density of 0.08 mA cm^{-2}.[57]

Recently, the sodium has replaced the lithium in batteries because it is about ten times

cheaper than the lithium. From the commercial perspective, the low-cost sodium-ion battery will be more promising than the current lithium-ion battery. Because of the large ionic radius of sodium, however, the selected cathode materials need crystal structures with open frameworks and larger interstitial volumes for the movement of the sodium ions. The basic electrochemical properties of Na/Cu_2S rechargeable batteries have been investigated at room temperature. The results show that it has the first discharge capacity of 294 mAh g^{-1}, which decreases to 220 mAh g^{-1} after the 20th cycle.[58] Stoichiometric Cu_2Se has also been applied as a cathode material for sodium ion battery and exhibited large reversible capacity, good cycling stability and low polarization.[26]

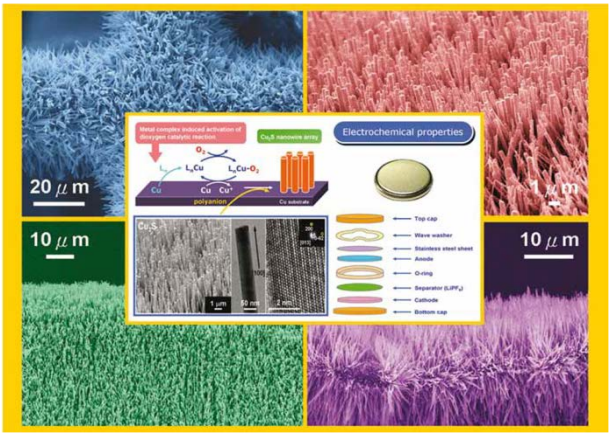

Figure 1.7 Highly ordered large-scale Cu_2S nanowire arrays on copper as cathodes show stable lithium-ion insertion/extraction reversibility, and high reversible lithium storage capability in lithium-ion battery applications.[27]

1.2.5 Photothermal therapy

Photothermal therapy utilizes the large absorption of nanomaterials (especially small

nanoparticles) in the NIR region for the treatment of various medical conditions, including destroying tumor cells. Owing to weak absorption of NIR radiation by tissues, it is able to penetrate the skin without causing much damage to normal tissues, so that it can be used to treat specific cells targeted by the nanomaterials.[59] A series of traditional nanomaterials strongly absorb NIR radiation, including gold nanoshells,[60] gold nanorods,[61] gold nanocages,[62-63] and single-walled carbon nanotubes,[64] which have been demonstrated to have potential therapeutic applications. Copper chalcogenide nanocrystals, with low-cost and facile synthesis compared to noble metals, were explored for photothermal therapy.[31,65-66] Specifically, CuS nanoparticles, under irradiation from a NIR laser beam at 808 nm, induced photothermal destruction of human cervical cancer HeLa cells in a laser dose- and nanoparticle concentration-dependent manner, while displaying minimal toxic effects with a profile similar to that of gold nanoparticles.[30] $Cu_{2-x}Se$ nanocrystals excited by NIR light at 800 nm led to significant human colorectal cancer cell death, which demonstrated that the $Cu_{2-x}Se$ nanocrystals have similar photothermal transduction efficiency to CuS (Figure 1.8).[29]

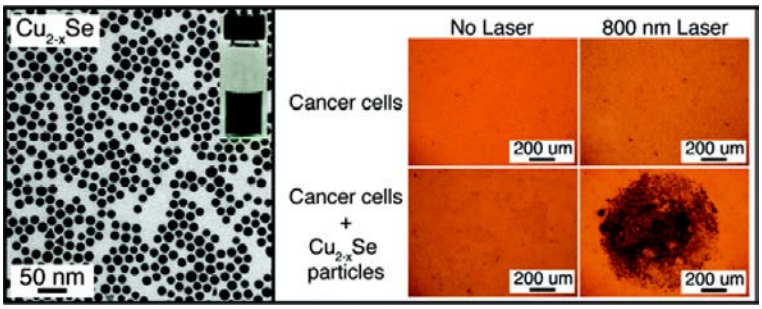

Figure 1.8 Transmission electron microscope (TEM) image of $Cu_{2-x}Se$ nanocrystals (left)

and comparison of photothermal destruction of human colorectal cancer cells without and with the addition of 2.8×10^{15} $Cu_{2-x}Se$ nanocrystals/L (right).[29]

1.3 Current synthesis approaches for copper chalcogenides

1.3.1 Hydrothermal or solvothermal method

The hydrothermal method is usually carried out in steel pressure vessels (autoclaves) with or without Teflon liners inside. These containers place in aqueous solution under controlled temperature and/or pressure conditions. The temperature of reaction circumstance can be increased above the boiling point of water, reaching the pressure of vapor saturation. The internal pressure of reaction circumstance also can be adjusted by setting temperature and the amount of solution added to the autoclave. The solvothermal method is similar to the hydrothermal method, except replacing solvent to non-aqueous. In the solvothermal system, the temperature can be elevated much higher than in the hydrothermal method because organic solvents have high boiling points. Based on this trait, the range of temperature of reaction circumstance is determined by choosing organic solvents with various boiling points. More specifically, the solvothermal method provides better control than the hydrothermal method of the size and shape distributions and the crystallinity of the copper chalcogenide because of higher reaction temperature. Metal oxides are commonly synthesized by these hydrothermal or solvothermal methods.

Similarly, as oxygen group elements, metal sulfide or metal selenide can be fabricated by imitating these methods as well. For the fabrication of Cu_xS nanocrystals, the reagents in aqueous solution or organic solvents are Cu precursors (i.e., $CuCl_2$, copper acetates) and sulfur sources (i.e., S^{2-}, $S_2O_3^{2-}$ or thiourea).[31,67-73] For the synthesis of Cu_xSe nanocrystals, Cu precursors are reacted with Na_2SeSO_3, Na_2SeO_3, Se, or selenourea in aqueous solutions or organic solvents.[29,74-80]. The morphology of the nanostructures can be controlled by solvents, pressure and temperature in the hydrothermal or solvothermal system (Figure 1.9).[81-95] In conclusion, these methods can synthesize highly crystallized copper chalcogenide nanostructures, but their sizes are relatively big and not uniform.[96-98]

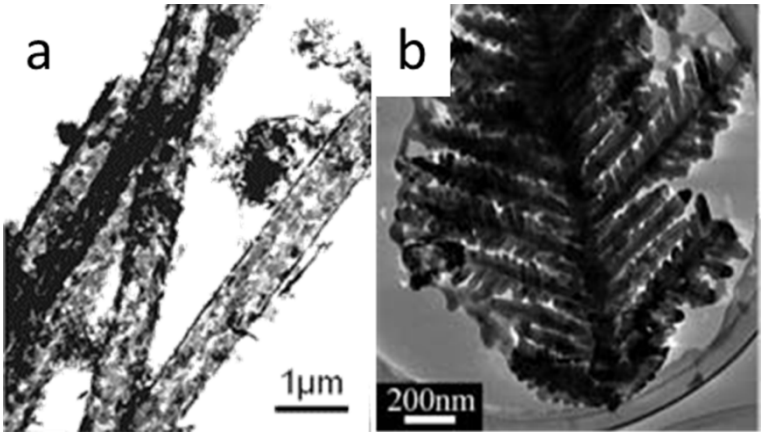

Figure 1.9 TEM images of (a) CuS microtubes and (b) $Cu_{2-x}Se$ dendrites synthesized by hydrothermal and solvothermal methods, respectively.[70,92]

1.3.2 Standard Schlenk line technique

The Schlenk line is a type of chemistry apparatus that is used for safely and successfully manipulating air-sensitive compounds. This technique is suitable for

avoiding oxidation of metallic precursors because of the sealed heating system and hot injection.[99-100] The earlier reports on this method are focused on the fabrication of different morphologies of CdSe nanostructures (i.e., rod-, arrow-, teardrop-, tetrapod-, and branched tetrapod-shaped) (Figure 1.10)[101-103] As this a general synthesis strategy, Cu_xS or Cu_xSe nanoparticles were also prepared under inert conditions using a standard Schlenk line (Figure 1.11).[30,104-105] The most suitable solvents are alkyl amines or alkyl thiols, because they have high melting point, which can reach more than 300 ˚C, much higher than in using hydrothermal and solvothermal methods. The Cu precursors could be Cu(II) acetylacetonate or regular copper salts (i.e., $CuNO_3$ and $Cu(CH_3CO_2)_2$.) The sulfur or selenium precursors can be organic compounds containing sulfur or selenium or prepared by directly dissolving sulfur or selenium powder into trioctylphosphine (TOP), trioctylphosphine oxide (TOPO) [104,106] or alkyl amines (i.e., oleylamine)[92,105]. At high temperature, the sizes of copper chalcogenide nanostructures are easier to control and keep smaller than 10 nm, and the particles have good distributions. Ternary $CuInSe_2$ nanoplatelets were synthesized by heating a mixture of the reactants in oleylamine by this method.[107]

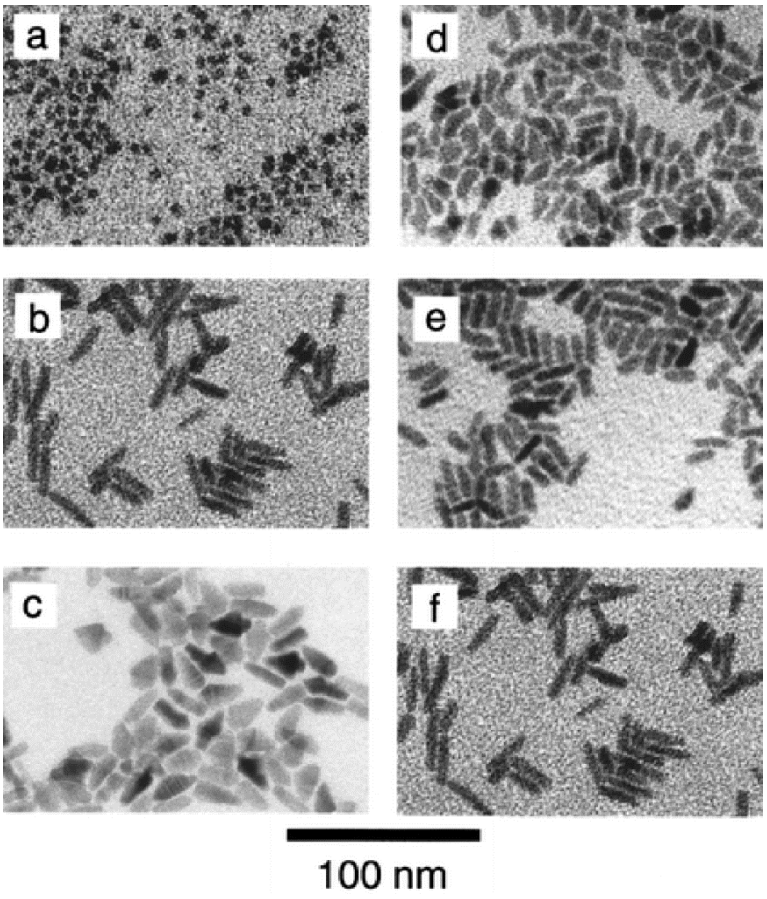

Figure 1.10 TEM images of different morphologies of CdSe from single-injection experiments.[102]

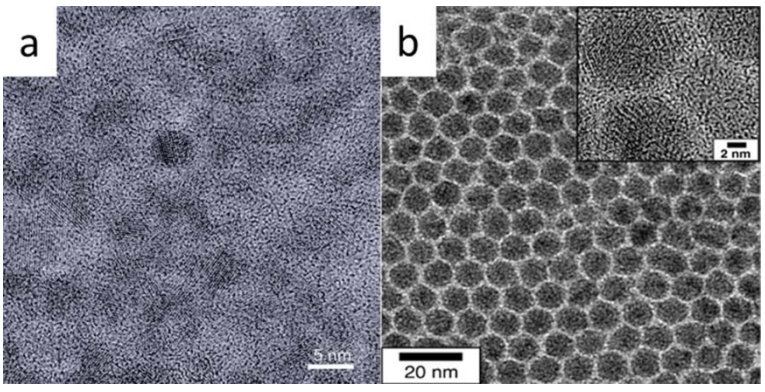

Figure 1.11 TEM images of CuS (left) and $Cu_{2-x}Se$ nanoparticles (right).[30,104]

1.3.3 Thermolysis methods

Apart from those that have been fabricated by high pressure, high temperature or air-proof methods, copper chalcogenide nanostructures have also been synthesized by thermolysis of an as-formed precursor of a copper thiolate complex. In the typical preparation of Cu_xS nanocrystals, copper salt and thiol substances are mixed and heated for achieving products with different morphologies and sizes. For example, Cu_2S nanodisks can be directly synthesized by adding the as-prepared copper precursor to dodecanethiol and then heating [Figure 1.12(a)].[100] Other morphologies of CuS or Cu_2S nanocrystals, such as nanoribbons, nanorods, nanoplatelets, and small nanoparticles, also can be synthesized either by solvent-less thermolysis of the single precursor[108-113] or thermolysis of the precursor in an organic solvent under high temperatures.[114-116] $Cu_{2-x}Se$ nanowires have been prepared by thermolysis of the as-formed CuSe as single precursor [Figure 1.12(b)].[95] Based on these $Cu_{2-x}Se$ nanowires, $CuInSe_2/CuInS_2$ core/shell nanowire bundles have been prepared by the hydrothermal method.[117]

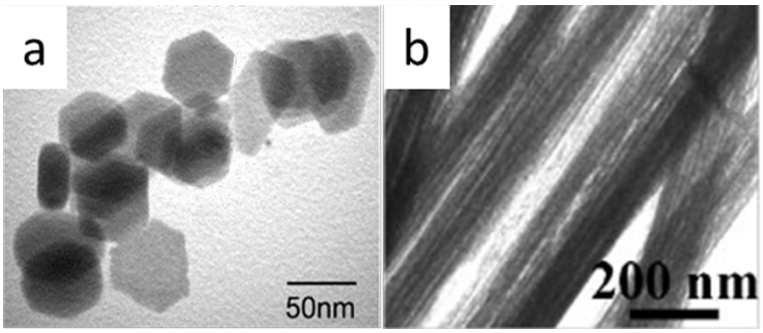

Figure 1.12 TEM images of Cu_2S nanodisks (left) and $Cu_{2-x}Se$ nanowires (right).[95,100]

1.3.4 Microwave method

Alternatively, irradiation with high-frequency electromagnetic waves can be a heating method for the preparation of nanocrystals in a short time. The principle of this method is that electric and magnetic components of microwaves change in direction rapidly and apply a force on charged particles as a result of their movements, which creates friction and collisions of the molecules. The major advantages of using microwaves for industrial processing are rapid heat transfer and volumetric and selective heating. For example, Cu_9S_8 nanorods were prepared by this microwave-assisted method from a previously formed precursor, which was made from a composite of $[Cu(NO_3)_2{\cdot}3H_2O]$ - sodium dodecyl sulfate (SDS) - thioacetamide (TAA).[118] Similarly, copper-enriched or sulfur-enriched copper sulfide nanostructures (e.g. spheres, nanotubes, and nanoparticles) were synthesized by using the same mechanism with changing precursor composition (Figure 1.13).[119-121] For the synthesis of copper selenides, the precursor contains copper salt and a selenium source with organic solvents. Then, the mixture is put into a microwave oven at different powers and for different times in air.[122-123]

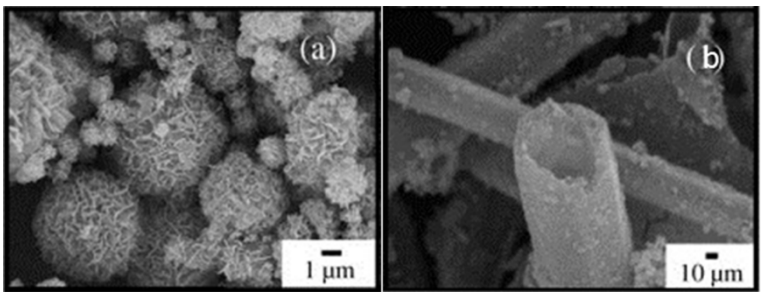

Figure 1.13 Scanning electron microscope (SEM) images of (a) CuS spheres and (b) CuS nanotubes.[119]

1.3.5 Sonochemical method

In contrast to the traditional high-temperature methods, the sonochemical method utilizes ultrasound oscillations to generate pressure waves as the result of acoustic cavitation instead of the movement of the molecules. Cavitation collapse produces intense local heating (~5000 K), high pressures (~1000 atm), and enormous heating and cooling rates (>10^9 K/s). This method is not confined to the preparation of different components of materials, such as alloys, carbides, oxides, and colloids of transition metals. Copper chalcogenide nanocrystals also have been prepared by this sonochemical approach.[75,92,109,124-131] For example, different copper selenide phases, such as $Cu_{2-x}Se$, β-CuSe, and Cu_3Se_2 have been produced from copper iodide and sodium selenate.[75] This method has not been widely applied due to certain disadvantages, such as irregular morphology and the danger to people from ultrasound irradiation.

1.3.6 Eletrodeposition

Electrodeposition is a universal route for coating on a surface by the action of reduction at the cathode. In a typical system, the metallic ions, from an electrolyte which contains the salt of the metal, are attracted to the cathode due to the current in the system. In the case where the as-prepared products are serving as electrodes in devices or for measurements, electrodeposition saves the process of assembling the materials on a substrate. Copper chalcogenide film can be grown by anodic oxidation or cathodic reduction methods from their salt solutions.[132-133] For instant, copper sulfide with

different morphologies (i.e., flakes, nanorods, and nanowires) has been deposited on a substrate film or with template assistance [Figure 1.14(a-c)].[134-136] By the same principle, the electrodeposition of copper selenide nanocubes or nanoparticles has been achieved from copper salt aqueous solution at room temperature [Figure 1.14(d)].[137-138] Ternary $CuInSe_2$ layers were grown on substrates in an acid solution containing the Cu, In, and Se by electrodeposition.[139]

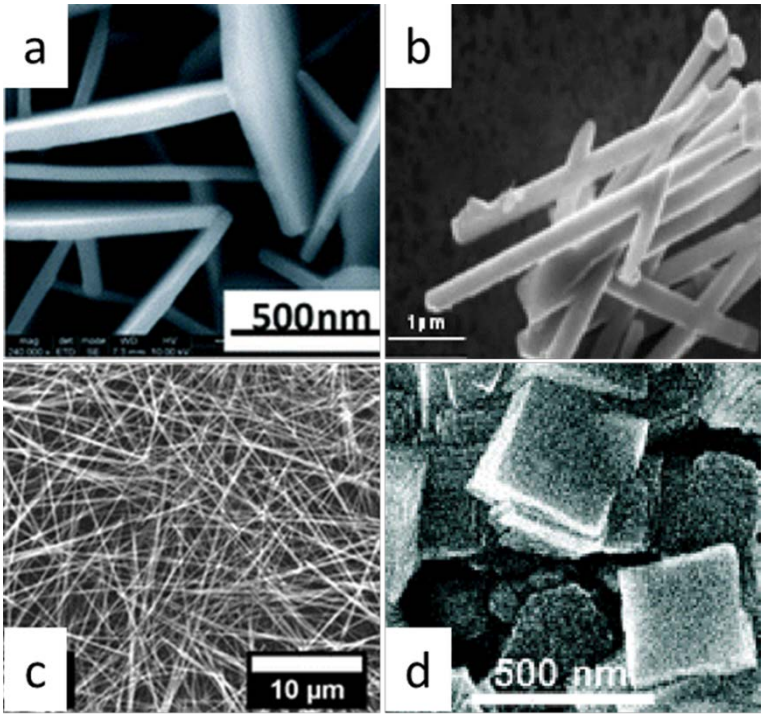

Figure 1.14 SEM and TEM images of (a) CuS flakes, (b) CuS nanorods, (c) CuS NWs, and (d) $Cu_{2-x}Se$ nanocubes.[134-137]

1.3.7 Melting and ball milling method

These two methods are used for preparing large-scale and exact-stoichiometric

samples. Copper chalcogenide crystals with different stoichiometry can be prepared by melting the elements Cu and S (or Se, Te) in quartz tubes at high temperature (over 1000 K) in vacuum, and then slowly cooling down to room temperature over several days.[140-141] The elemental stoichiometry and phase of the products are easily tuned by the ratio of initial elements, with processing by a high-energy ball-milling method. For example, tetragonal $Cu_{1.92}S$-$Cu_{1.99}S$, rhombohedral $Cu_{1.71}S$-$Cu_{1.89}S$, CuS, various selenides (β-$Cu_{2-x}Se$, Cu_3Se_2, γ-CuSe, $CuSe_2$), and tellurides ($Cu_{2-x}Te$, Cu_3Te_2) have been prepared from mixtures of the elements.[25,142]

1.3.8 Cation exchange reaction

Cation exchange has emerged as particularly powerful and promising method to prepare well-defined nano-architectures, as it can retain the size, shape, and anionic framework of the parent nanostructures by replacing their cationic sublattice with a different metal ion.[143-151] Alivisatos et al. first reported a complete and fully reversible cationic exchange that occurred in colloidal CdS, CdSe and CdTe nanocrystals, nanorods, and tetrapods.[144] This research shows that the cation exchange reaction is a facile route for accessing more materials in nanostructures with diverse compositions, structures, and shapes via rapid, low-temperature transformations in the solid state, without having to develop new synthetic methods to produce each individual nanostructure. The promising advantage of the cation exchange reaction is that it is extremely fast compared to other fabrication methods, and this strategy has been successfully applied to prepare

heterostructured, doped, alloyed, and core-shell nanocrystals.[146,151-156] For example, a dual interface heterostructured copper sulfide layer capped with zinc sulfide grains in spherical nanocrystals was synthesized, and the extent of the cation exchange can be precisely manipulated to tune the thickness of the internal layer down to the single atom level.[157] Very recently, phase-selective cation exchange enabled the successful transformation of CdS nanowires into $Cu_{2-x}S$ nanowires with the tunable crystal structure.[158] It is particularly suitable for preparation of late-transition-metal chalcogenide (e.g. $Cu_{2-x}E$, E = S, Se, and Te) nanostructures due to their significant ionic character and capability for cation diffusion into and out of the lattice (Figure 1.15).[159-160] For example, hollow and cave containing nanoparticles $Cu_{2-x}S_ySe_{1-y}$ nanoparticles were prepared from core/shell $Cu_{2-x}Se/Cu_{2-x}S$ nanocrystals by the diffusion of Cu^+ from the $Cu_{2-x}Se$ core into the $Cu_{2-x}S$ shell.[161] These partially exchanged nano-architectures even display advanced performance in various applications.[162-163]

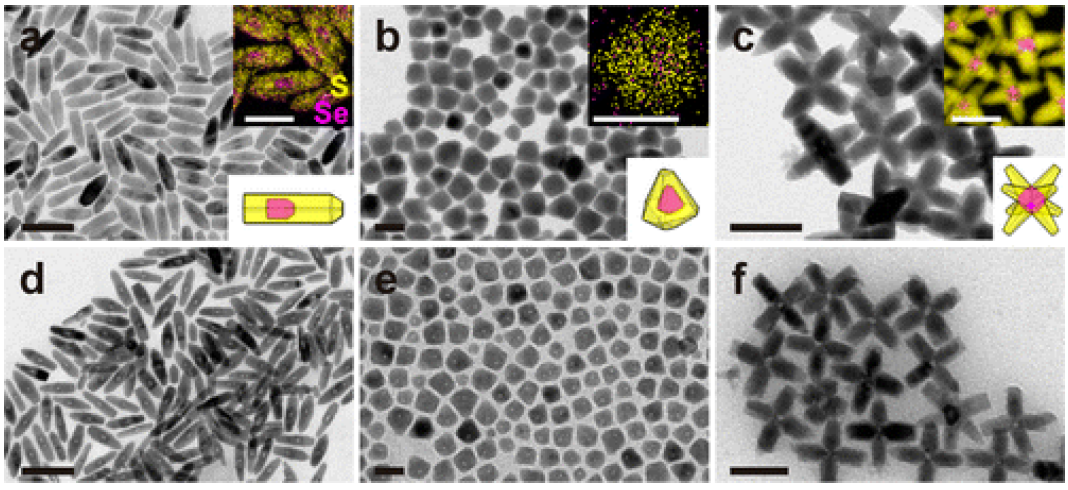

Figure 1.15 Shapes and geometries for $Cu_{2-x}Se/Cu_{2-x}S$ core/shell nanocrystals.[160]

1.4 Need for designed copper chalcogenide nanostructures in energy conversion

Based on the above investigation, nanostructured copper chalcogenides have much potential for sustainable energy devices, especially in the aspect of energy conversion. Thermoelectric conversion or counter electrodes for QDSSCs still have space for improvement.

Thermoelectric materials are semiconductors with high electrical conductivity and low thermal conductivity that can directly convert thermal energy into electricity in the presence of a temperature difference. The research about the electrical and thermal behavior of copper selenides has a long history.[9] In the recent years, copper selenides have been rediscovered in the thermoelectric area and displayed an enhanced performance. For example, non-doped β-phase Cu_2Se and $Cu_{2-x}Se$ fabricated by a high-temperature solid state reaction have a *ZT* values of around 1.5 at 1000 K, which is the highest value among the bulk materials. This value was notably enhanced to 1.7-1.8 at 700 ˚C by the introduction of nanoscale precipitates through fast quenching of their liquids in a later report. Most methods, however, are not able to produce large-scale samples for thermoelectric research. Thus, a facile synthesis of copper selenide on a large scale is desirable.

QDSSCs include a photoelectrode, CE, sensitizer, and electrolyte. Using semiconductor quantum-dots with narrow band gaps sensitize working electrode

semiconductors with wide band gaps has enhanced energy conversion efficiency. Currently, the conventional noble metal CEs (Pt or Au) are unsuitable for QDSSC applications when polysulfide electrolytes are used, mainly because sulfur-containing (S^{2-} or thiol) compounds are absorbed preferentially and strongly on the Pt or Au surface, leading to surface passivation and decrease in the conductivity of electrodes. In contrast, copper-chalcogenide-based CEs show lower resistance and higher electrocatalytic activity towards the redox reaction of polysulfide, thus improving the conversion efficiency of QDSSCs. Current investigations in this field are mainly focused on zero-dimensional (0D) copper sulfides, but their 1D counterparts show better performance. For example, the power conversion efficiency of QDSSCs with the designed ITO@Cu_2S CEs increased by 84.5 % and 33.5 % compared to planar Au and Cu_2S CEs, respectively.[20] There have been few reports on copper selenides CEs, however, so their nanostructures have not too much enhancement in terms of the conversion efficiency of QDSSCs. Thus, the design and synthesis of copper selenides with large surface area and benefits from electron transport are highly desirable.

In this thesis, the design and synthesis of binary and ternary copper chalcogenides for thermoelectric conversion and QDSSCs applications are investigated.

1.5 Thesis structure

Chapter 1 simply introduces the general background, various broad applications and

synthesis approaches for copper chalcogenides, as well as discussing major problems, and the significance and objectives of this study.

Chapter 2 contains the chemicals and methods used for preparation of materials and the instrumental analysis techniques for characterization of the copper chalcogenide nanostructures, including X-ray diffraction (XRD), scanning electron microscopy (SEM), transmission electron microscopy (TEM), X-ray photoelectron spectroscopy (XPS), inductively coupled plasma − atomic emission spectroscopy (ICP-AES), differential scanning calorimetry (DSC), Brunauer-Emmett-Teller (BET) surface area measurements, Raman spectroscopy, and ultraviolet-visible (UV-vis) spectroscopy.

Chapter 3 reports on research aimed at the large-yield synthesis of surfactant-free $Cu_{2-x}Se$ NWs by the hydrothermal approach and the thermoelectric properties of these $Cu_{2-x}Se$ powders sintered by the spark plasma sintering (SPS) technique. Uniform, surfactant-free $Cu_{2-x}Se$ NWs were prepared via an aqueous route. The effects of reaction parameters, such as the Cu/Se precursor ratio, the Se/NaOH ratio, and the reaction time, on the formation of NWs are comprehensively investigated. The results show that $Cu_{2-x}Se$ NWs are formed through the assembly of CuSe nanoplates, accompanied by their self-redox reactions. The resultant $Cu_{2-x}Se$ NWs are explored as a potential thermoelectric candidate in comparison with commercial copper selenide (Cu_2Se) powder. Both synthetic and commercial samples have a similar performance, and their figures of merit (*ZT*) are 0.29 and 0.38 at 480 ˚C, respectively. Although the *ZT* of

$Cu_{2-x}Se$ has not been observably increased compared to the *ZT* of commercial Cu_2Se, the introduction of nanocrystals of $Cu_{2-x}Se$ decreased the thermal conductivity, because the enhancement of phonon scattering by nanocrystals can decrease the lattice thermal conductivity at high temperature. In addition, the Cu-deficiency in $Cu_{2-x}Se$ increased the electrical conductivity compared to that in commercial Cu_2Se.

Chapter 4, based on the previous chapter, is devoted to searching for a facile and high yield fabrication method for copper selenide, which is an issue for thermoelectric application. Grams of $Cu_{2-x}Se$ nanostructures were prepared from commercial copper and selenium powders in the presence of thiol ligands by a one-pot reaction at room temperature. The morphology of the nanostructures is strongly dependent on the ratio of thiol ligand to selenium powder. The resultant $Cu_{2-x}Se$ nanostructures were treated with hydrazine solution to remove the surface ligands and then explored as a potential thermoelectric candidate in comparison with commercial copper selenide powders. The results demonstrated that the synthetic samples from our novel approach have similar thermoelectric properties to commercial Cu_2Se, which is similar to the results in the previous chapter, although $Cu_{2-x}Se$ retained its cubic structure, while commercial Cu_2Se was converted to a mixture of cubic and tetragonal structures after high-temperature measurements, so that the resultant $Cu_{2-x}Se$ has a more stable crystal structure than commercial Cu_2Se.

In Chapter 5, the universal synthesis method mentioned in Chapter 4 was

demonstrated by a computational method. Using this ambient facile method, $Cu_{2-x}E$ (E = S, Se) NTs with a hierarchical architecture and assembled as CEs for QDSSCs. $Cu_{2-x}Se$ and $Cu_{2-x}S$ NTs were fabricated by using Cu NWs, and stable sulfur or selenium powder as precursors at room temperature. The influence of the reaction parameters (e.g., precursor ratio, ligands, ligand ratio, and reaction time) on the formation of the nanotubes was comprehensively investigated. The resultant $Cu_{2-x}E$ (E = S, Se) NTs were used as CEs in QDSSCs to achieve a conversion efficiency (η) of 5.02 % and 6.25 %, respectively, much higher than that of QDSSCs made with Au CEs (η = 2.94 %).

In Chapter 6, one-dimensional/two-dimensional (1D/2D) ternary CuAgSe NTs were successfully prepared from the $Cu_{2-x}Se$ NTs synthesized at room temperature within a short reaction time by the facile cation exchange approach. The cation exchange leads to the transformation of the crystal structure from cubic to orthorhombic and/or tetragonal with good retention of morphology. The exchange reactions are spontaneous due to the large negative changes in the Gibbs free energy (ΔG). The effects of parameters such as reaction time, precursor source, and precursor ratio on the exchange reaction were investigated. The resultant CuAgSe NTs were explored as CEs of QDSSCs and achieved much higher conversion efficiency (η = 5.61 %) than those of QDSSCs containing the noble-metal Au CEs (3.32 %), which was due to the higher mobility of both Cu^+ and Ag^+ ions in the CuAgSe NTs and the higher stability of metal selenides in polysulfide electrolyte, which was achieved by avoiding corrosion and passivation than that of the

Au CEs.

References

[1] Ruhle, S.; Shalom, M.; Zaban, A. *ChemPhysChem* **2010**, *11*, 2290.

[2] Debe, M. K. *Nature* **2012**, *486*, 43.

[3] Service, R. F. *Science* **2004**, *306*, 806.

[4] Poudel, B.; Hao, Q.; Ma, Y.; Lan, Y. C.; Minnich, A.; Yu, B.; Yan, X. A.; Wang, D. Z.; Muto, A.; Vashaee, D.; Chen, X. Y.; Liu, J. M.; Dresselhaus, M. S.; Chen, G.; Ren, Z. F. *Science* **2008**, *320*, 634.

[5] Bell, L. E. *Science* **2008**, *321*, 1457.

[6] Poizot, P.; Laruelle, S.; Grugeon, S.; Dupont, L.; Tarascon, J. M. *Nature* **2000**, *407*, 496.

[7] Wikipedia, Thermoelectric effect; *Retrieved from https://en.wikipedia.org/wiki/Thermoelectric_effect*.

[8] Seebeck, T. J. *Ann. Phys.* **1821**, *82*, 133.

[9] Dennler, G.; Chmielowski, R.; Jacob, S.; Capet, F.; Roussel, P.; Zastrow, S.; Nielsch, K.; Opahle, I.; Madsen, G. K. H. *Adv. Energy Mater.* **2014**, *4*, 1301581.

[10] Ma, Y.; Hao, Q.; Poudel, B.; Lan, Y. C.; Yu, B.; Wang, D. Z.; Chen, G.; Ren, Z. F. *Nano Lett.* **2008**, *8*, 2580.

[11] Joshi, G.; Lee, H.; Lan, Y. C.; Wang, X. W.; Zhu, G. H.; Wang, D. Z.; Gould, R.

W.; Cuff, D. C.; Tang, M. Y.; Dresselhaus, M. S.; Chen, G.; Ren, Z. F. *Nano Lett.* **2008**, *8*, 4670.

[12] David Penalva, Thermoelectric stove; *Retrieved from http://davidpenalva.com/thermoelectric-stove/.*

[13] PV EDUCATION.ORG, Solar Cell Structure; *Retrieved from http://www.pveducation.org/pvcdrom/solar-cell-operation/solar-cell-structure.*

[14] Tian, J. J.; Cao, G. Z. *Nano Reviews* **2013**, *4*, 22578.

[15] Baxter, J.; Bian, Z. X.; Chen, G.; Danielson, D.; Dresselhaus, M. S.; Fedorov, A. G.; Fisher, T. S.; Jones, C. W.; Maginn, E.; Kortshagen, U.; Manthiram, A.; Nozik, A.; Rolison, D. R.; Sands, T.; Shi, L.; Sholl, D.; Wu, Y. Y. *Energ. Environ. Sci.* **2009**, *2*, 559.

[16] HYDROGENICS, Fuel Cells; *Retrieved from http://www.hydrogenics.com/technology-resources/hydrogen-technology/fuel-cells.*

[17] Flickr, How a lithium-ion battery works bu Argonne National Laboratory; *Retrieved from http://www.flickr.com/photos/argonne/5029455937.*

[18] Vaughan, D. J.; Craig, J. R. *Mineral Chemistry of Metal Sulfides, Cambridge University Press, Cambridge* **1978**.

[19] Timothy, H. *J. Alloy Compd.* **1995**, *229*, 40.

[20] Jiang, Y.; Zhang, X.; Ge, Q. Q.; Yu, B. B.; Zou, Y. G.; Jiang, W. J.; Song, W. G.;

Wan, L. J.; Hu, J. S. *Nano Lett.* **2014**, *14*, 365.

[21] Bo, F.; Zhang, C. F.; Wang, C. L.; Xu, S. H.; Wang, Z. Y.; Cui, Y. P. *J. Mater. Chem. A* **2014**, *2*, 14585.

[22] Choi, H. M.; Ji, I. A.; Bang, J. H. *ACS Appl. Mater. Interfaces* **2014**, *6*, 2333.

[23] Liu, S. L.; Zhang, Z. S.; Bao, J. C.; Lan, Y. Q.; Tu, W. W.; Han, M.; Dai, Z. H. *J. Phys. Chem. C* **2013**, *117*, 15164.

[24] Liu, H. L.; Shi, X.; Xu, F. F.; Zhang, L. L.; Zhang, W. Q.; Chen, L. D.; Li, Q.; Uher, C.; Day, T.; Snyder, G. J. *Nat. Mater.* **2012**, *11*, 422.

[25] Yu, B.; Liu, W. S.; Chen, S.; Wang, H.; Wang, H. Z.; Chen, G.; Ren, Z. F. *Nano Energy* **2012**, *1*, 472.

[26] Yue, J. L.; Sun, Q.; Fu, Z. W. *Chem. Commun.* **2013**, *49*, 5868.

[27] Lai, C. H.; Huang, K. W.; Cheng, J. H.; Lee, C. Y.; Hwang, B. J.; Chen, L. J. *J. Mater. Chem.* **2010**, *20*, 6638.

[28] Anker, J. N.; Hall, W. P.; Lyandres, O.; Shah, N. C.; Zhao, J.; Van Duyne, R. P. *Nature Materials* **2008**, *7*, 442.

[29] Hessel, C. M.; Pattani, V. P.; Rasch, M.; Panthani, M. G.; Koo, B.; Tunnell, J. W.; Korgel, B. A. *Nano Lett.* **2011**, *11*, 2560.

[30] Li, Y. B.; Lu, W.; Huang, Q. A.; Huang, M. A.; Li, C.; Chen, W. *Nanomedicine* **2010**, *5*, 1161.

[31] Zhou, M.; Zhang, R.; Huang, M. A.; Lu, W.; Song, S. L.; Melancon, M. P.; Tian,

M.; Liang, D.; Li, C. *J. Am. Chem. Soc.* **2010**, *132*, 15351.

[32] Brown, D. R.; Day, T.; Caillat, T.; Snyder, G. J. *J. Electron. Mater.* **2013**, *42*, 2014.

[33] Zhao, L. L.; Wang, X. L.; Wang, J. Y.; Cheng, Z. X.; Dou, S. X.; Wang, J. L.; Liu, L. Q. *Scientific Reports* **2015**, *54*, 7671.

[34] Heyding, R. D.; Murray, R. M. *Can. J. Chem.* **1976**, *54*, 841.

[35] Oliveria, M.; Mcmullan, R. K.; Wuensch, B. J. *Solid State Ionics* **1988**, *28*, 1332.

[36] Stevels, A. L. N.; Wiegers, G. A. *Recl. Trav. Chim. Pays-Bas* **1971**, *90*, 352.

[37] Lee, Y. L.; Lo, Y. S. *Adv. Funct. Mater.* **2009**, *19*, 604.

[38] Hodes, G.; Manassen, J.; Cahen, D. *J. Electrochem. Soc.* **1980**, *127*, 544.

[39] Yang, Z. S.; Chen, C. Y.; Liu, C. W.; Chang, H. T. *Chem. Commun.* **2010**, *46*, 5485.

[40] Gonzalez-Pedro, V.; Xu, X. Q.; Mora-Sero, I.; Bisquert, J. *ACS Nano* **2010**, *4*, 5783.

[41] Yang, Z. S.; Chen, C. Y.; Liu, C. W.; Li, C. L.; Chang, H. T. *Adv. Energy Mater.* **2011**, *1*, 259.

[42] Kim, H. J.; Kim, J. H.; Kumar, C. P.; Punnoosea, D.; Kim, S. K.; Gopia, C. V.; Rao, S. S. *J. Electroanal. Chem.* **2015**, *739*, 20.

[43] Chen, W. L.; Wang, M.; Qian, T. Y.; Cao, H. L.; Huang, S. S.; He, Q. Q.; Liang, N.; Wang, C.; Zai, J. T. *Nano Energy* **2015**, *12*, 186.

[44] Kim, C. S.; Choi, S. H.; Bang, J. H. *ACS Appl. Mater. Interfaces* **2014**, *6*, 22078.

[45] Wang, W. L.; Zhang, L.; Chen, G. H.; Jiang, J.; Ding, T.; Zuo, J.; Yang, Q. *CrystEngComm* **2015**, *17*, 1975.

[46] Wu, H. B.; Chen, W. *J. Am. Chem. Soc.* **2011**, *133*, 15236.

[47] Li, Q.; Xu, P.; Zhang, B.; Tsai, H.; Zheng, S. J.; Wu, G.; Wang, H. L. *J. Phys. Chem. C* **2013**, *117*, 13872.

[48] Tarascon, J. M.; Armand, M. *Nature* **2001**, *414*, 359.

[49] Yoo, E.; Kim, J.; Hosono, E.; Zhou, H.; Kudo, T.; Honma, I. *Nano Lett.* **2008**, *8*, 2277.

[50] Hu, L.; Huang, Y. M.; Zhang, F. P.; Chen, Q. W. *Nanoscale* **2013**, *5*, 4186.

[51] Gao, X. P.; Bao, J. L.; Pan, G. L.; Zhu, H. Y.; Huang, P. X.; Wu, F.; Song, D. Y. *J. Phys. Chem. B* **2004**, *108*, 5547.

[52] Lee, Y. H.; Leu, I. C.; Liao, C. L.; Chang, S. T.; Wu, M. T.; Yen, J. H.; Fung, K. Z. *Electrochem. Solid-State Lett.* **2006**, *9*, A207.

[53] Morales, J.; Sanchez, L.; Bijani, S.; Martinez, L.; Gabas, M.; Ramos-Barrado, J. R. *Electrochem. Solid-State Lett.* **2005**, *8*, A159.

[54] Gabano, J. P.; Gerbier, G.; Jammet, J.; Dechenau.V *J. Electrochem. Soc.* **1972**, *119*, 459.

[55] Wang, X. X.; Wang, Y. H.; Li, X.; Liu, B.; Zhao, J. B. *J. Power Sources* **2015**, *281*, 185.

[56] Xue, M. Z.; Zhou, Y. N.; Zhang, B.; Yu, L.; Zhang, H.; Fu, Z. W. *J. Electrochem. Soc.* **2006**, *153*, A2262.

[57] Zhang, W. X.; Zhou, Z. Y.; Zhao, W. R.; Yang, Z. H.; Yang, X. N. *J. Mater. Chem. A* **2014**, *2*, 5800.

[58] Kim, J. S.; Kim, D. Y.; Cho, G. B.; Nam, T. H.; Kim, K. W.; Ryu, H. S.; Ahn, J. H.; Ahn, H. J. *J. Power Sources* **2009**, *189*, 864.

[59] Kim, J.; Park, S.; Lee, J. E.; Jin, S. M.; Lee, J. H.; Lee, I. S.; Yang, I.; Kim, J. S.; Kim, S. K.; Cho, M. H.; Hyeon, T. *Angew. Chem., Int. Ed.* **2006**, *45*, 7754.

[60] Oldenburg, S. J.; Averitt, R. D.; Westcott, S. L.; Halas, N. J. *Chem. Phys. Lett.* **1998**, *288*, 243.

[61] Huang, X. H.; Neretina, S.; El-Sayed, M. A. *Adv. Mater.* **2009**, *21*, 4880.

[62] Chen, J. Y.; Wang, D. L.; Xi, J. F.; Au, L.; Siekkinen, A.; Warsen, A.; Li, Z. Y.; Zhang, H.; Xia, Y. N.; Li, X. D. *Nano Lett.* **2007**, *7*, 1318.

[63] Chen, J. Y.; Glaus, C.; Laforest, R.; Zhang, Q.; Yang, M. X.; Gidding, M.; Welch, M. J.; Xia, Y. N. *Small* **2010**, *6*, 811.

[64] Huang, X. H.; El-Sayed, I. H.; Qian, W.; El-Sayed, M. A. *J. Am. Chem. Soc.* **2006**, *128*, 2115.

[65] Zha, Z. B.; Zhang, S. H.; Deng, Z. J.; Li, Y. Y.; Li, C. H.; Dai, Z. F. *Chem. Commun.* **2013**, *49*, 3455.

[66] Ku, G.; Zhou, M.; Song, S. L.; Huang, Q.; Hazle, J.; Li, C. *ACS Nano* **2012**, *6*,

7489.

[67] Kalyanikutty, K. P.; Nikhila, M.; Maitra, U.; Rao, C. N. R. *Chem. Phys. Lett.* **2006**, *432*, 190.

[68] Roy, P.; Srivastava, S. K. *Mater. Lett.* **2007**, *61*, 1693.

[69] Puspitasari, I.; Gujar, T. P.; Jung, K. D.; Joo, O. S. *Mater. Sci. Eng., B* **2007**, *140*, 199.

[70] Ni, Y.; Liu, H.; Wang, F.; Yin, G.; Hong, J.; Ma, X.; Xu, Z. *Appl. Phys. A* **2004**, *79*, 2007.

[71] Ratanatawanate, C.; Bui, A.; Vu, K.; Balkus, K. J. *J. Phys. Chem. C* **2011**, *115*, 6175.

[72] Gong, J. Y.; Yu, S. H.; Qian, H. S.; Luo, L. B.; Liu, X. M. *Chem. Mater.* **2006**, *18*, 2012.

[73] Dixit, S. G.; Mahadeshwar, A. R.; Haram, S. K. *Colloid Surf., A* **1998**, *133*, 69.

[74] Zhang, W. X.; Zhang, X. M.; Zhang, L.; Wu, J. X.; Hui, Z. H.; Cheng, Y. W.; Liu, J. W.; Xie, Y.; Qian, Y. T. *Inorg. Chem.* **2000**, *39*, 1838.

[75] Xie, Y.; Zheng, X. W.; Jiang, X. C.; Lu, J.; Zhu, L. Y. *Inorg. Chem.* **2002**, *41*, 387.

[76] Ingole, P. P.; Joshi, P. M.; Haram, S. K. *Colloid Surf., A* **2009**, *337*, 136.

[77] Garcia, V. M.; Nair, P. K.; Nair, M. T. S. *J. Cryst. Growth* **1999**, *203*, 113.

[78] Vinod, T. P.; Jin, X.; Kim, J. *Mater. Res. Bull.* **2011**, *46*, 340.

[79] Zheng, X. W.; Hu, Q. T. *Appl. Phys. A* **2009**, *94*, 805.

[80] Yang, Y. J.; Hu, S. S. *J. Solid State Electrochem.* **2009**, *13*, 477.

[81] Su, H. L.; Xie, Y.; Qiao, Z. P.; Qian, Y. T. *Mater. Res. Bull.* **2000**, *35*, 1129.

[82] Wang, W. Z.; Yan, P.; Liu, F. Y.; Xie, Y.; Geng, Y.; Qian, Y. T. *J. Mater. Chem.* **1998**, *8*, 2321.

[83] Li, B.; Xie, Y.; Huang, J. X.; Liu, Y.; Qian, Y. T. *Chem. Mater.* **2000**, *12*, 2614.

[84] Zhang, Y.; Hu, C. G.; Zheng, C. H.; Xi, Y.; Wan, B. Y. *J. Phys. Chem. C* **2010**, *114*, 14849.

[85] Roy, P.; Srivastava, S. K. *J. Nanosci. Nanotechnol.* **2008**, *8*, 1523.

[86] Roy, P.; Srivastava, S. K. *Cryst. Growth Des.* **2006**, *6*, 1921.

[87] Qin, A. M.; Fang, Y. P.; Ou, H. D.; Liu, H. Q.; Su, C. Y. *Cryst. Growth Des.* **2005**, *5*, 855.

[88] Nan, Z. D.; Wang, X. Y.; Zhao, Z. B. *J. Cryst. Growth* **2006**, *295*, 92.

[89] Ni, Y. H.; Liu, R.; Cao, X. F.; Wei, X. W.; Hong, H. M. *Mater. Lett.* **2007**, *61*, 1986.

[90] An, C. H.; Wang, S. T.; He, J.; Wang, Z. X. *J. Cryst. Growth* **2008**, *310*, 266.

[91] Gao, J. N.; Li, Q. S.; Zhao, H. B.; Li, L. S.; Liu, C. L.; Gong, Q. H.; Qi, L. M. *Chem. Mater.* **2008**, *20*, 6263.

[92] Kumar, P.; Singh, K.; Srivastava, O. N. *J. Cryst. Growth* **2010**, *312*, 2804.

[93] Zhuang, Z. B.; Peng, Q.; Zhang, B.; Li, Y. D. *J. Am. Chem. Soc.* **2008**, *130*, 10482.

[94] Li, D. P.; Zheng, Z.; Lei, Y.; Ge, S. X.; Zhang, Y. D.; Zhang, Y. G.; Wong, K. W.; Yang, F. L.; Lau, W. M. *CrystEngComm* **2010**, *12*, 1856.

[95] Xu, J.; Zhang, W. X.; Yang, Z. H.; Ding, S. X.; Zeng, C. Y.; Chen, L. L.; Wang, Q.; Yang, S. H. *Adv. Funct. Mater.* **2009**, *19*, 1759.

[96] Zhu, Y. C.; Mei, T.; Wang, Y.; Qian, Y. T. *J. Mater. Chem.* **2011**, *21*, 11457.

[97] Zhuang, Z. B.; Peng, Q.; Li, Y. D. *Chem. Soc. Rev.* **2011**, *40*, 5492.

[98] Han, Z. H.; Li, Y. P.; Zhao, H. Q.; Yu, S. H.; Yin, X. L.; Qian, Y. T. *Mater. Lett.* **2000**, *44*, 366.

[99] Li, W.; Zamani, R.; Ibáñez, M.; Cadavid, D.; Shavel, A.; Morante, J. R.; Arbiol, J.; Cabot, A. *J. Am. Chem. Soc.* **2013**, *135*, 4664.

[100] Du, X. S.; Yu, Z. Z.; Dasari, A.; Ma, J.; Meng, Y. Z.; Mai, Y. W. *Chem. Mater.* **2006**, *18*, 5156.

[101] Peng, X. G.; Manna, L.; Yang, W. D.; Wickham, J.; Scher, E.; Kadavanich, A.; Alivisatos, A. P. *Nature* **2000**, *404*, 59.

[102] Manna, L.; Scher, E. C.; Alivisatos, A. P. *J. Am. Chem. Soc.* **2000**, *122*, 12700.

[103] Murray, C. B.; Norris, D. J.; Bawendi, M. G. *J. Am. Chem. Soc.* **1993**, *115*, 8706.

[104] Riha, S. C.; Johnson, D. C.; Prieto, A. L. *J. Am. Chem. Soc.* **2011**, *133*, 1383.

[105] Deka, S.; Genovese, A.; Zhang, Y.; Miszta, K.; Bertoni, G.; Krahne, R.; Giannini, C.; Manna, L. *J. Am. Chem. Soc.* **2010**, *132*, 8912.

[106] Choi, J.; Kang, N.; Yang, H. Y.; Kim, H. J.; Son, S. U. *Chem. Mater.* **2010**, *22*,

3586.

[107] Bi, W. T.; Zhou, M.; Ma, Z. Y.; Zhang, H. Y.; Yu, J. B.; Xie, Y. *Chem. Commun* .**2012**, *48*, 9162.

[108] Ma, G. X.; Zhou, Y. L.; Li, X. Y.; Sun, K.; Liu, S. Q.; Hu, J. Q.; Kotov, N. A. *ACS Nano* **2013**, *7*, 9010.

[109] Zhao, Y. X.; Pan, H. C.; Lou, Y. B.; Qiu, X. F.; Zhu, J. J.; Burda, C. *J. Am. Chem. Soc.* **2009**, *131*, 4253.

[110] Ghezelbash, A.; Korgel, B. A. *Langmuir* **2005**, *21*, 9451.

[111] Chen, L.; Chen, Y. B.; Wu, L. M. *J. Am. Chem. Soc.* **2004**, *126*, 16334.

[112] Sigman, M. B.; Ghezelbash, A.; Hanrath, T.; Saunders, A. E.; Lee, F.; Korgel, B. A. *J. Am. Chem. Soc.* **2003**, *125*, 16050.

[113] Larsen, T. H.; Sigman, M.; Ghezelbash, A.; Doty, R. C.; Korgel, B. A. *J. Am. Chem. Soc.* **2003**, *125*, 5638.

[114] Lou, Y. B.; Samia, A. C. S.; Cowen, J.; Banger, K.; Chen, X. B.; Lee, H.; Burda, C. *Phys. Chem. Chem. Phys.* **2003**, *5*, 1091.

[115] Liu, Y. S.; Qin, D. H.; Wang, L.; Cao, Y. *Mater. Chem. Phys.* **2007**, *102*, 201.

[116] Kumar, P.; Gusain, M.; Nagarajan, R. *Inorg. Chem.* **2011**, *50*, 3065.

[117] Xu, J.; Lee, C. S.; Tang, Y. B.; Chen, X.; Chen, Z. H.; Zhang, W. J.; Lee, S. T.; Zhang, W. X.; Yang, Z. H. *ACS Nano* **2010**, *4*, 1845.

[118] Liao, X. H.; Chen, N. Y.; Xu, S.; Yang, S. B.; Zhu, J. J. *J. Cryst. Growth* **2003**,

252, 593.

[119] Thongtem, T.; Phuruangrat, A.; Thongtem, S. *Mater. Lett.* **2010**, *64*, 136.

[120] Zhu, J. F.; Zhu, Y. J.; Ma, M. G.; Yang, L. X.; Gao, L. *J. Phys. Chem. C* **2007**, *111*, 3920.

[121] Mu, C. F.; Yao, Q. Z.; Qu, X. F.; Zhou, G. T.; Li, M. L.; Fu, S. Q. *Colloid Surf., A* **2010**, *371*, 14.

[122] Zhu, J. J.; Palchik, O.; Chen, S. G.; Gedanken, A. *J. Phys. Chem. B* **2000**, *104*, 7344.

[123] Zhang, Y.; Qiao, Z. P.; Chen, X. M. *J. Mater. Chem.* **2002**, *12*, 2747.

[124] Xu, S.; Wang, H.; Zhu, J. J.; Chen, H. Y. *J. Cryst. Growth* **2002**, *234*, 263.

[125] Behboudnia, M.; Khanbabaee, B. *J. Cryst. Growth* **2007**, *304*, 158.

[126] Xu, H. L.; Wang, W. Z.; Zhu, W.; Zhou, L. *Nanotechnology* **2006**, *17*, 3649.

[127] Cao, H. L.; Qian, X. F.; Zai, J. T.; Yin, J.; Zhu, Z. K. *Chem. Commun.* **2006**, *43*, 4548.

[128] Kumar, P.; Singh, K. *Struct. Chem.* **2011**, *22*, 103.

[129] Low, K. H.; Li, C. H.; Roy, V. A. L.; Chui, S. S. Y.; Chan, S. L. F.; Che, C. M. *Chem. Sci.* **2010**, *1*, 515.

[130] Zhang, S. Y.; Fang, C. X.; Tian, Y. P.; Zhu, K. R.; Jin, B. K.; Shen, Y. H.; Yang, J. X. *Cryst. Growth Des.* **2006**, *6*, 2809.

[131] Xu, C. Q.; Zhang, Z. C.; Ye, Q.; Liu, X. *Chem. Lett.* **2003**, *32*, 198.

[132] Mazor, H.; Golodnitsky, D.; Burstein, L.; Peled, E. *Electrochem. Solid-State Lett.* **2009**, *12*, A232.

[133] Engelken, R. D.; Mccloud, H. E. *J. Electrochem. Soc.* **1985**, *132*, 567.

[134] Chen, Y. H.; Davoisne, C.; Tarascon, J. M.; Guery, C. *J. Mater. Chem.* **2012**, *22*, 5295.

[135] Singh, K. V.; Martinez-Morales, A. A.; Andavan, G. T. S.; Bozhilov, K. N.; Ozkan, M. *Chem. Mater.* **2007**, *19*, 2446.

[136] Ghahremaninezhad, A.; Asselin, E.; Dixon, D. G. *J. Phys. Chem. C* **2011**, *115*, 9320.

[137] Yu, R.; Ren, T.; Sun, K. J.; Feng, Z. C.; Li, G. N.; Li, C. *J. Phys. Chem. C* **2009**, *113*, 10833.

[138] Thouin, L.; Rouquettesanchez, S.; Vedel, J. *Electrochim. Acta* **1993**, *38*, 2387.

[139] Izquierdo-Roca, V.; Saucedo, E.; Ruiz, C. M.; Fontane, X.; Calvo-Barrio, L.; Alvarez-Garcia, J.; Grand, P. P.; Jaime-Ferrer, J. S.; Perez-Rodriguez, A.; Morante, J. R.; Bermudez, V. *Phys. Status Solidi A* **2009**, *206*, 1001.

[140] Liu, H. L.; Shi, X.; Xu, F. F.; Zhang, L. L.; Zhang, W. Q.; Chen, L. D.; Li, Q.; Uher, C.; Day, T.; Snyder, G. J. *Nat. Mater.* **2012**, *11*, 422.

[141] Liu, H. L.; Shi, X.; Kirkham, M.; Wang, H.; Li, Q.; Uher, C.; Zhang, W. Q.; Chen, L. D. *Mater. Lett.* **2013**, *93*, 121.

[142] Ohtani, T.; Motoki, M.; Koh, K.; Ohshima, K. *Mater. Res. Bull.* **1995**, *30*, 1495.

[143] Rivest, J. B.; Jain, P. K. *Chem. Soc. Rev.* **2013**, *42*, 89.

[144] Son, D. H.; Hughes, S. M.; Yin, Y. D.; Alivisatos, A. P. *Science* **2004**, *306*, 1009.

[145] Jain, P. K.; Amirav, L.; Aloni, S.; Alivisatos, A. P. *J. Am. Chem. Soc.* **2010**, *132*, 9997.

[146] Robinson, R. D.; Sadtler, B.; Demchenko, D. O.; Erdonmez, C. K.; Wang, L. W.; Alivisatos, A. P. *Science* **2007**, *317*, 355.

[147] Sadtler, B.; Demchenko, D. O.; Zheng, H.; Hughes, S. M.; Merkle, M. G.; Dahmen, U.; Wang, L. W.; Alivisatos, A. P. *J. Am. Chem. Soc.* **2009**, *131*, 5285.

[148] Luther, J. M.; Zheng, H. M.; Sadtler, B.; Alivisatos, A. P. *J. Am. Chem. Soc.* **2009**, *131*, 16851.

[149] Deka, S.; Miszta, K.; Dorfs, D.; Genovese, A.; Bertoni, G.; Manna, L. *Nano Lett.* **2010**, *10*, 3770.

[150] Li, H. B.; Zanella, M.; Genovese, A.; Povia, M.; Falqui, A.; Giannini, C.; Manna, L. *Nano Lett.* **2011**, *11*, 4964.

[151] Miszta, K.; Dorfs, D.; Genovese, A.; Kim, M. R.; Manna, L. *ACS Nano* **2011**, *5*, 7176.

[152] Li, H. B.; Brescia, R.; Povia, M.; Prato, M.; Bertoni, G.; Manna, L.; Moreels, I. *J. Am. Chem. Soc.* **2013**, *135*, 12270.

[153] Mukherjee, B.; Peterson, A.; Subramanian, V. *Chem. Commun.* **2012**, *48*, 2415.

[154] Li, H. B.; Brescia, R.; Krahne, R.; Bertoni, G.; Alcocer, M. J. P.; D'Andrea, C.;

Scotognella, F.; Tassone, F.; Zanella, M.; De Giorgi, M.; Manna, L. *ACS Nano* **2012**, *6*, 1637.

[155] Tang, J. Y.; Huo, Z. Y.; Brittman, S.; Gao, H. W.; Yang, P. D. *Nat. Nanotechnol.* **2011**, *6*, 568.

[156] Yao, Q. H.; Arachchige, I. U.; Brock, S. L. *J. Am. Chem. Soc.* **2009**, *131*, 2800.

[157] Ha, D. H.; Caldwell, A. H.; Ward, M. J.; Honrao, S.; Mathew, K.; Hovden, R.; Koker, M. A.; Muller, D. A.; Hennig, H. G.; Robinson, R. D. *Nano Lett.* **2014**, *14*, 7090.

[158] Zhang, D. D.; Wong, A. B.; Yu, Y.; Brittman, S.; Sun, J. W.; Fu, A.; Beberwyck, B.; Alivisatos, A. P.; Yang, P. D. *J. Am. Chem. Soc.* **2014**, *136*, 17430.

[159] Stam, W.; Akkerman, Q. A.; Ke, X. X.; Huis, M. A.; Bals, S.; Donega, C. M. *Chem. Mater.* **2015**, *27*, 283.

[160] Kriegel, I.; Rodriguez-Fernandez, J.; Wisnet, A.; Zhang, H.; Waurisch, C.; Eychmuller, A.; Dubavik, A.; Govorov, A. O.; Feldmann, J. *Acs Nano* **2013**, *7*, 4367.

[161] Miszta, K.; Brescia, R.; Prato, M.; Bertoni, G.; Marras, S.; Xie, Y.; Ghosh, S.; Kim, M. R.; Manna, L. *J. Am. Chem. Soc.* **2014**, *136*, 9061.

[162] Pang, M. L.; Zeng, H. C. *Langmuir* **2010**, *26*, 5963.

[163] Cao, H. L.; Qian, X. F.; Wang, C.; Ma, X. D.; Yin, J.; Zhu, Z. K. *J. Am. Chem. Soc.* **2005**, *127*, 16024.

CHAPTER 2 Experimental Methods

2.1 Chemical reagents

Table 2.1 Chemicals and materials used in the thesis.

Materials/Chemicals	**Formula**	**Purity**	**Supplier**
Acetone	C_3H_6O	> 99.9%	Sigma-Aldrich
Anhydrous ethanol	C_2H_6O	> 99.5%	Sigma-Aldrich
Copper nitrate 3-hydrate	$Cu(NO_3)_2$	99.5%	Aldrich
Copper powder (-40 mesh)	Cu	99.5%	Aldrich
Copper powder (-150 mesh)	Cu	99.5%	Sigma-Aldrich
Copper(I) selenide	Cu_2Se	99.95%	Alfa Aesar
Cysteamine	C_2H_7NS	> 99.0%	Sigma-Aldrich
Ethylenediamine	$C_2H_4(NH_2)_2$	99.0%	Alfa Aesar
Hydrazine solution	NH_2NH_2	35 wt%	Sigma-Aldrich
Milli-Q water	H_2O	18.2 MΩ·cm	NA
Potassium chloride	KCl	> 99.9%	Sigma-Aldrich
Selenium powder (-325 mesh)	Se	99.5%	Alfa Aesar
Silver acetate	$AgC_2H_3O_2$	> 99.99%	Sigma-Aldrich
Silver nitrate	$AgNO_3$	> 99.0%	Sigma-Aldrich

Sodium hydroxide (low chloride)	NaOH	97.0%	Alfa Aesar
Sodium sulphide	Na_2S	> 99.0%	Sigma-Aldrich
Sulfur powder	S	> 99.5%	Sigma-Aldrich
Thioglycolic acid	$C_2H_4O_2S$	> 99.0%	Sigma-Aldrich
1-dodecanethiol	$C_{12}H_{26}S$	> 99.0%	Sigma-Aldrich
2-mercaptoethanol	$HO(CH_2)_2SH$	> 99.0%	Sigma-Aldrich
3-mercapto-1-propanol	$HS(CH_2)_3OH$	> 99.0%	Sigma-Aldrich
3-mercaptopropionic acid	$HSCH_2CH_2CO_2H$	> 99.0%	Sigma-Aldrich
4-mercapto-1-butanol	$HS(CH_2)_4OH$	> 99.0%	Sigma-Aldrich

2.2 Preparation approaches

The main preparation methods used in this thesis are aqueous solution thermolysis and magnetic stirring at room temperature. All the experimental details are shown in the following chapters.

2.2.1 Aqueous solution thermolysis

This method relies on water evaporation at high temperature and reactant self-redox during water evaporation. After the aqueous solution of reactants was prepared in a beaker, the beaker was placed in a fan-forced oven at a certain temperature. Water was gradually evaporated away during extended time, and at last, the dry products were left

on the bottom of the beaker.[1]

2.2.2 Magnetic stirring method

A magnetic stirrer is a device that is based on a rotating magnetic field to make a stir bar spin in a chemical or biological reaction system. The size of stir bar is small (a couple of centimetres) and the outside materials of stir bar are glass or Teflon which are easily cleaned and sterilized. Because of their outside materials, stir bars can work in glass and Teflon containers for stirring viscous liquids or thick suspensions. The advantage of magnetic stirrers is that they can be used inside hermetically closed vessels or systems by placing stir bar in reaction system before sealing the system. Magnetic stirrers can also combine with a hot plate or some other means for heating the liquid.[2]

2.3 Characterization and measurement methods

2.3.1 X-ray diffraction (XRD)

X-ray diffraction (XRD) is a method for determination of the identity and crystallinity of a synthesized compound. The principle is that: “The X-rays are generated by a cathode ray tube, filtered to produce monochromatic radiation, collimated to concentrate the beam, and directed toward the prepared sample. The interaction of the incident rays with the sample produces constructive interference (and a diffracted ray) when conditions satisfy Bragg’s Law:

$$2d \sin\theta = n\lambda \quad (2.1)$$

where d is the lattice spacing in a crystalline sample, λ is the wavelength of electromagnetic radiation, n is any integer, and θ is the diffraction angle of incidence experienced by the X-ray beam reflection from the faces of the crystal (Figure 2.1)."[3]

When a crystal sample is scanned with X-rays, diffraction peaks will be produced once the crystal inter-planer spacing and the wavelength of X-rays satisfy the relationship shown in Equation 2.1. For determining what this sample is, the resultant pattern was compared with standard reference patterns, which were obtained from previous experiments or calculations. Each standard reference pattern has a number, called JCPDS number. If all peaks in measured pattern match with a standard reference pattern, this sample has the same crystal structure with a standard reference in a unique JCPDS number. Not only the crystal structure, the crystal size of materials can also be estimated and calculated according to the Scherrer formula:

$$D = \frac{K\lambda}{\beta \cos\theta} \quad (2.2)$$

where K is the shape factor of the average crystallite (with a typical shape factor around 0.9), λ is the X-ray wavelength, β is the half-peak width, and θ is the Bragg angle.

The XRD device used in this thesis work is a GBC MMA diffractometer with a Cu Kα radiation (λ = 1.5406 Å) at 40 kV and 25 mA at a scanning rate of 2° min^{-1} for 2θ in the range of 20-80°. The scanning rate can be adjusted from 0.1° min^{-1} to 10° min^{-1}. The slower of the scanning rate is, the less of noise is, which means the pattern is smoother

than that obtained using fast scanning rate. This equipment cannot record at very low angles (e.g. 0.1-10°).

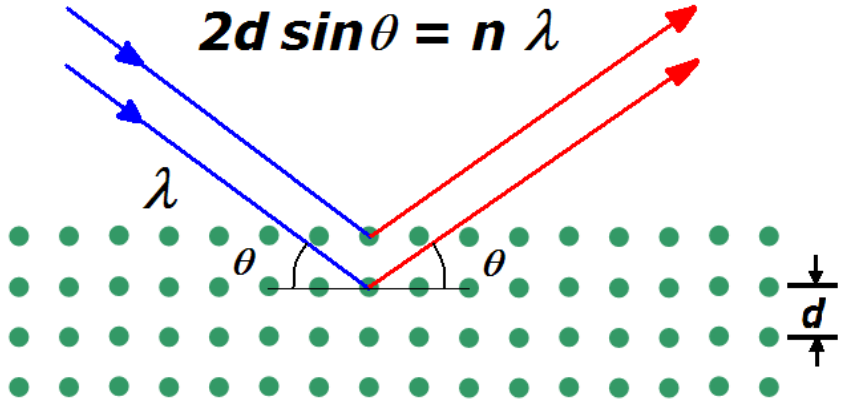

Figure 2.1 Bragg's Law defining the conditions for the occurrence of diffraction peaks.[3]

2.3.2 Scanning electron microscopy (SEM)

Scanning electron microscope (SEM) can produce detailed images of the surface of samples by scanning them with a focused beam of electrons (Figure 2.2).[4] These accelerated electrons are produced from electron gun on the top of a microscope. When electrons reached the surface atoms of prepared sample, they interact and produce some signals that can be detected and collected by a detector. These interactions can be classified into two groups. In the first group, electrons are scattered due to elastic collisions with atoms in the specimen and lose very little energy in the process. These electrons are called backscattered electrons. In the second group, electrons collide with atoms in the specimen inelastically and cause atoms collided to be ionized. Electrons

emitted as a result of this ionization are called secondary electrons.[5] These signals contain the information of the surface of samples that can be interpreted to morphology and composition of samples in images. Technically, a single machine cannot have all detectors for all signals. The SEM only uses secondary electrons detected and collected by the secondary electron detector to form an image of sample. For taking the high-resolution images for revealing details of a sample surface, the electron beam must be narrow. Besides, the images also have a large depth of field, which can appear a 3D visualisation of a sample surface for understanding. The range of magnifications can be adjusted from about 10 times to more than 500,000 times.[4]

The field emission SEM (FE-SEM) images of all samples in this thesis were collected using a JEOL JMS 7500-FA microscope with an accelerating voltage of 5 kV and a secondary electron detector. The energy dispersive X-ray spectroscopy (EDS) was performed on the X-ray spectrometer attached to the JEOL JMS 7500-FA. The X-ray is produced by the interactions of electron beam with sample, and used to map the distribution and estimate the contents of elements in the sample.

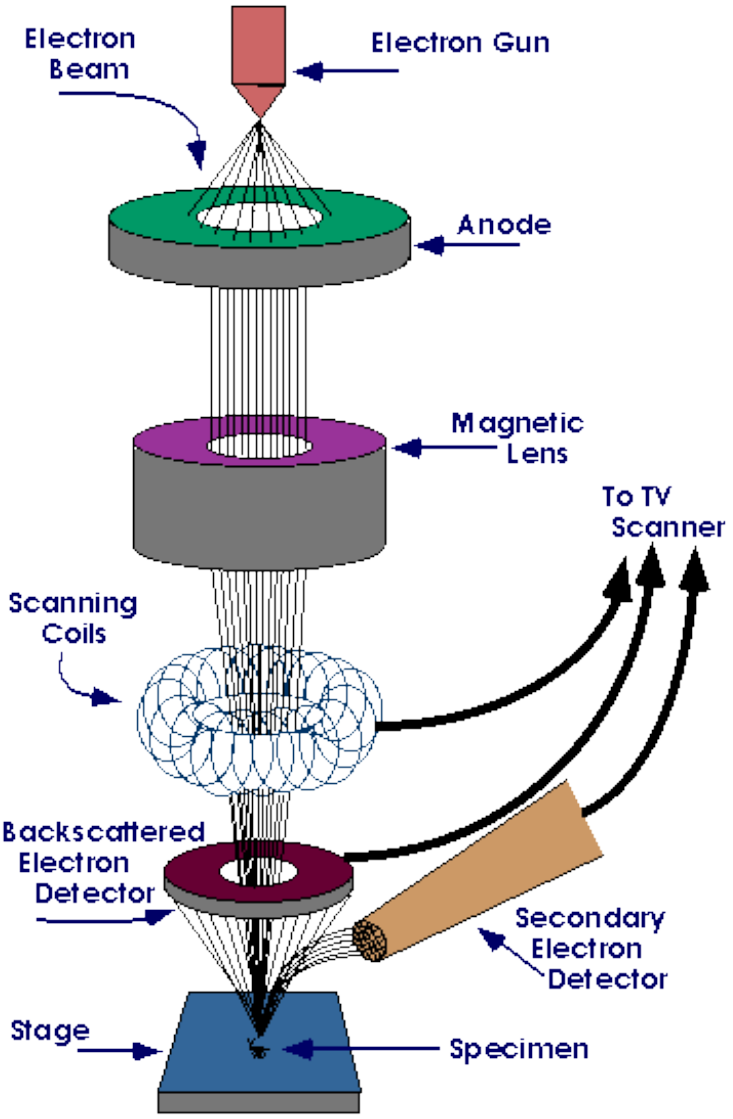

Figure 2.2 Diagram of scanning electron microscope.[4]

2.3.3 Transmission electron microscopy (TEM)

Transmission electron microscopy (TEM) can display morphology images of samples by using electrons beams transmitted through an ultra-thin sample (Figure 2.3). This technique is specially used to reveal internal structure in nanoscale solids. There are four

parameters influence the information of sample: “the resolving power of the microscope (usually smaller than 0.3 nm); the energy spread of the electron beam (often several eV); the thickness of the specimen (almost always significantly less than 1 μm), and the composition and stability of the specimen.”[6] TEM images have significantly higher resolution than SEM images because of the small de Broglie wavelength of electrons, which enables researchers to examine fine detail—even as small as a single column of atoms.[6] The image-forming principle is different when using low or high magnifications TEM. At low magnification, the image is formed directly by occlusion and absorption of electrons in the sample. The thickness and composition of samples and absorption of electrons in the samples influence the image contrast. Thicker sample or regions with more specimens will appear dark, while regions with no sample appear bright. At high magnifications, high-resolution transmission electron microscopy (HRTEM), also known as phase contrast, can investigate structures of materials, such as crystal orientation, electronic structure, and chemical identity. Image formation is given by complex wave interactions of the incoming electron beams. Apart from them, selected area electron diffraction (SAED) is an effective technique for observing crystal orientation. For thin crystalline samples, this produces an image that consists of a pattern of dots in the case of a single crystal, or a series of rings in the case of a polycrystalline material. For the single crystal case, the diffraction pattern is dependent upon the orientation of the specimen and the structure of the sample illuminated by the

electron beam. This image provides the investigator with information about the space group symmetries in the crystal and the crystal's orientation to the beam path. This is typically done without utilizing any information but the position at which the diffraction spots appear and the observed image symmetries.

A scanning transmission electron microscope (STEM) is a type of TEM. The raster of electron beam across the sample makes it suitable for a few analysis techniques such as elemental mapping by energy dispersive X-ray (EDX) spectroscopy, electron energy loss spectroscopy (EELS) and annular dark-field imaging (ADF). These signals can be obtained simultaneously, allowing direct correlation of image and quantitative data.

The TEM images in this thesis were collected on a JEOL-2010 and a JEOL ARM-200F microscope operated at 200 kV. Elemental mapping was performed on the X-ray spectrometer attached to the JEOL ARM-200F instrument by using Ni grids.

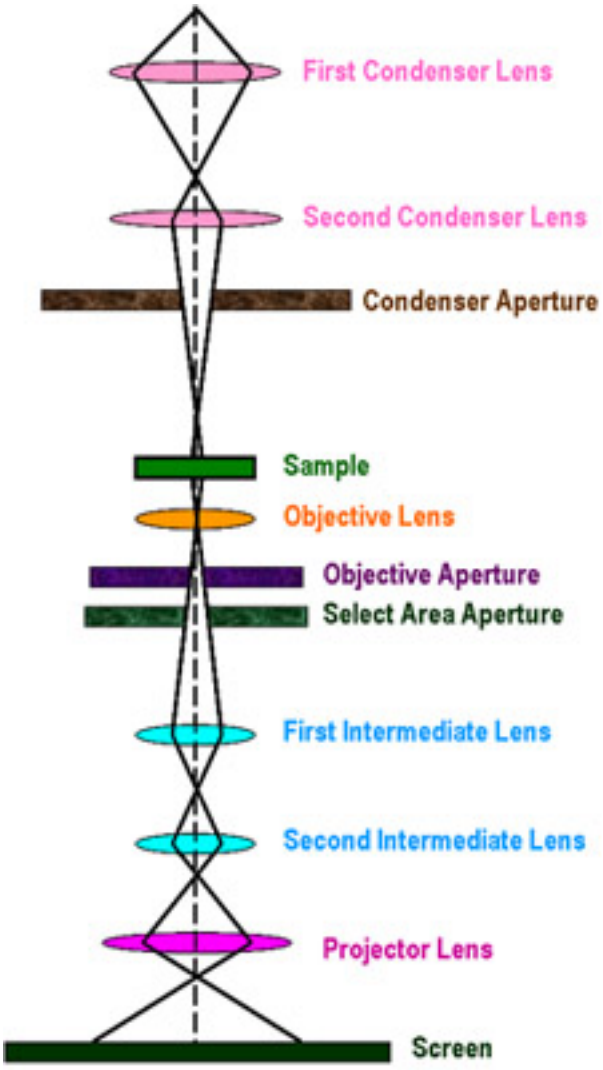

Figure 2.3 Schematic diagram of transmission electronic microscopy.[6]

2.3.4 X-ray photoelectron spectroscopy (XPS)

X-ray photoelectron spectroscopy (XPS) is a sensitive quantitative spectroscopic technique that measures the elemental composition of the sample surface. It can be used to characterize the valence state and ratio of the elements that exist on the surface of a sample when the sample is fresh prepared, or after some treatments, such as fracturing,

cutting, scraping, or exposing in the air. The spectra of samples are obtained by presenting a material under X-rays beam and simultaneously counting the kinetic energy and number of electrons that escape from the top 0 to 10 nm of the material being analysed. Identifying each peak produced from elements of the sample is compared the position of peaks with known data of handbooks. For avoiding a shift from a positive or negative surface charge, the spectra of peaks are usually calibrated by standard carbon and oxygen peaks.

In this thesis, the XPS spectra were collected by XPS instrument assembled by the Institute for Superconducting and Electronic Materials. This technique is used to investigate the valence states of elements in order to understand the reaction mechanism.

2.3.5 Inductively coupled plasma − atomic emission spectroscopy (ICP-AES)

Inductively coupled plasma atomic − emission spectroscopy (ICP-AES), or inductively coupled plasma optical emission spectrometry (ICP-OES), is used for detecting the trace of metal elements. The working principle is that atoms and ions in the samples, excited by the inductively coupled plasma, emit electromagnetic radiation at wavelengths for identifying a particular metal element.

In this thesis, all samples for ICP-AES were dissolved in 1.5% HNO_3, and the amounts of metal elements were traced by the ICP-AES instrument at UQ. This technique is used to investigate the element ratio of prepared compounds (e.g. $Cu_{2-x}Se$).

2.3.6 Thermogravimetric analysis (TGA)

Thermogravimetric analysis or thermal gravimetric analysis (TGA) is a method of thermal analysis for monitoring changes in physical and chemical properties of materials in terms of increasing temperature (with constant heating rate), or in terms of time (with constant temperature and/or constant mass loss).[7] This method is suitable to determine selected characteristics of materials that exhibit either mass loss or gain due to decomposition, oxidation, or loss of volatiles (such as moisture).

In this thesis, the weight loss of samples was measured with a Mettler-Toledo TGA/DSC instrument at UOW from 50-900 ˚C, with a heating rate of 5 ˚C min^{-1} in argon.

2.3.7 Differential scanning calorimetry (DSC)

Differential scanning calorimetry (DSC) is a thermoanalytical technique measuring a sample and a reference sample in an increasing temperature circumstance and obtaining the difference in the amount of heat. The heat capacity of reference sample should be known over the scanning range of temperatures. Then, the heat capacity of the sample can be determined by measurement result.

In this thesis, the heat capacity of samples was measured by a Mettler TGA/DSC instrument at Shanghai Mettler Company from 30-800 ˚C, with a heating rate of 20 K min^{-1}, and with the sample kept at 30 ˚C and 800 ˚C for 30 min, separately.

2.3.8 Brunauer-Emmett-Teller (BET)

Brunauer-Emmett-Teller (BET) theory can be used to explain the physical adsorption of gas molecules on a solid surface, which serves as a significant analysis technique for the measurement of the specific surface area, pore size, and pore volume of a material. The BET theory refers to multi-layer adsorption, and usually adopts non-corrosive gases (e.g., nitrogen, argon, carbon dioxide, etc.) as adsorbates to determine the surface area data. In this thesis, the surface area of samples was measured by a TriStar Ⅱ 3020 V1.04 at 77.3 K under nitrogen at UQ.

2.3.9 Raman spectroscopy

"Raman spectroscopy is a spectroscopic technique used to observe vibrational, rotational, and other low-frequency modes in molecules in a chemical system in both qualitative and quantitative applications."[8] Placing powder or film samples under a laser light, molecular vibrations or other excitations in the system interact with laser light and produce a shift up or down of laser phonons. This shift contains the information about bands between molecular of samples. The unique position and intensity of peaks in spectrum make Raman spectroscopy able to identify the chemical elements in the qualitative analysis. Besides, compared to infrared bands, Raman bands are inherently sharper, which present for more straightforward quantitative analysis.

In this thesis, the Raman spectroscopy was conducted with a 10 mW He/Ne laser at

632.8 nm (Jobin Yvon HR800) and was used to characterize the chemical composition and crystal structure of the samples.

2.3.10 Ultraviolet-visible (UV-vis) spectroscopy

Ultraviolet-visible (UV-vis) spectroscopy is an absorption spectroscopy or reflectance spectroscopy in the ultraviolet-visible (or near-UV and near-infrared) spectral region. For a liquid sample, the UV-vis absorption comes from molecules absorbing light in different wavelengths range. An absorption spectrum demonstrates a number of absorption bands corresponding to structural groups within the molecule. In this thesis, the measurement of UV-vis spectroscopy is not only carried out in solution but also in solid samples. For a solid sample, light is reflected by the surface of the sample because it cannot go through the solid sample. So the measurement of the band gap of solid samples was carried out by an attachment of UV-vis instrument (integrating spheres). The sample was placed in front of the incident light window for reflecting light on the detector that has a hollow sphere with a barium sulfate-coated interior. The obtained result of relative reflectance is related to the reflectance of the reference standard white board (barium sulfate-coated), which is considered to be 100%. “When light is directed at the sample at an angle of 0°, specularly reflected light exits the integrating sphere and is not detected. As a result, only diffuse reflected light is measured.”[9] In this thesis, the reflectance spectra were collected by a Shimadzu UV-3600 at IPRI.

2.4 Thermoelectric measurements

2.4.1 Preparation of samples

The as-synthesized $Cu_{2-x}Se$ powders or commercial Cu_2Se powders were loaded into a graphite die with a diameter of 20 mm and sintered into a pellet at 430 ˚C under 65 MPa for 10 min by the spark plasma sintering (SPS) technique. The resultant pellet was cut into pieces and polished into parallelepipeds with dimensions of ~2 mm × 3 mm × 10 mm for electrical conductivity and Seebeck coefficient measurements. The parallelepipeds were coated with a layer of boron nitride to protect the instrument against evaporation of the elements. For the thermal diffusivity measurements, the samples were cut and polished into a disk shape with a diameter of 10 mm and a thickness of 1 mm.

2.4.2 Measurement of thermoelectric performance

The electrical conductivity and the Seebeck coefficient were measured simultaneously under helium atmosphere from room temperature to 480 ˚C using an Ozawa RZ2001i (Japan). A Linseis LFA1000 (Germany) instrument was used to determine the thermal diffusivity of samples. The thermal conductivity (κ) was calculated using Equation (2.3):

$$\kappa = D \times C_p \times \rho \tag{2.3}$$

where D is the thermal diffusivity, C_p is the heat capacity, and ρ is the mass density of the specimen. The ρ values used here were calculated using the geometrical dimensions

of the specimens and their masses. The heat capacity was determined using the DSC method.

2.5 Assembly and measurements of QDSSCs

2.5.1 Preparation of photoelectrodes

CdS and CdSe sensitized TiO_2 working electrodes were prepared successively by casting the pastes on the fluorine-doped tin oxide (FTO) substrates using the doctor blade technique.[10] The TiO_2 film is composed of a 13.7 μm transparent layer (18NR-T paste, Dyesol) and a 4.5 μm light-scattering layer (WER2-O paste, Dyesol). [In Chapter 6, the TiO_2 film only includes a 13.7 μm transparent layer (18NR-T paste, Dyesol).] The working electrodes were gradually heated at 100 °C for 15 min and 500 °C for 30 min, respectively.

2.5.2 Preparation of counter electrodes

The sample CEs were prepared on FTO substrates by the doctor blade technique using the respective sample pastes. The pastes were prepared from sample powders according to previous work with some modifications.[11] The newly formed films were annealed at 350 °C for 30 min in Ar atmosphere to remove the binder and enhance the contact between the film and the substrate. For comparison, Au electrodes were prepared by sputtering to yield a thickness of ~ 50 nm (obtained from the calibration curve of the

sputtering).

2.5.3 Assembly and measurements of QDSSCs

The solar cells were fabricated by assembling the CEs and QD-sensitized TiO_2 film electrode with a binder clip separated by a 60 μm thick spacer. A mask with a window area of 0.16 cm^2 was clipped onto the TiO_2 side to define the active area of the cell when testing. The polysulfide electrolyte was composed of 2 M Na_2S, 2 M S, and 0.2 M KCl in Milli-Q water. For QDSSCs assembled under each set of conditions, at least 8 cells were prepared and tested in parallel, and the one with the medium value was chosen for the final data. For electrochemical impedance spectroscopy (EIS) and Tafel polarization measurements, the symmetric dummy cells were assembled from two identical CEs, using the same polysulfide electrolyte. The active area of the dummy cells was 0.64 cm^2. The photocurrent-voltage (*J*-*V*) tests of DSSCs were performed under one sun conditions using an air mass (AM) 1.5 solar simulator (Oriel), which was carefully calibrated with certified silicon solar cells. The light intensity of the solar simulator was adjusted to 100 mW cm^{-2} by using an optical power meter (Newport, 1918-c) with a detector (818P-040-25). *J*-*V* curves were obtained by applying an external bias to the cell, and measurements were recorded by a Keithley model 2420 digital source meter. The incident photon-to-current conversion efficiency (IPCE) plotted as a function of the excitation wavelength was obtained by using a Newport 1918-c power meter under irradiation of a 300 W Oriel xenon light source with an Oriel Cornerstone 260 1/4 m

monochromator in direct-current mode. The EIS were measured with dummy cells by using a Solartron 1260 Frequency Response Analyzer in combination with a Solartron 1480 Potentiostat in the dark. The applied bias voltage and ac amplitude were set at 0 V and 10 mV, and the frequency ranged from 106 to 0.1 Hz. Then, the Tafel-polarization measurements were recorded with a scan rate of 20 mV s^{-1} on an electrochemical workstation (CHI660d).

The fabrication of QD-sensitized TiO_2 film electrodes, assembly of QDSSCs, and measurements of the performance of cells were carried out at UQ with the help of colleagues.

References

[1] Xu, J.; Zhang, W. X.; Yang, Z. H.; Ding, S. X.; Zeng, C. Y.; Chen, L. L.; Wang, Q.; Yang, S. H. *Adv. Funct. Mater.* **2009**, *19*, 1759.

[2] Wikipedia, Magnetic stirrer; *Retrieved from https://en.wikipedia.org/wiki/Magnetic_stirrer*.

[3] Particle Analytical, X-Ray Diffraction-XRD; *Retrieved from http://particle.dk/methods-analytical-laboratory/xrd-analysis/*.

[4] Wikipedia, Scanning Electron Microscope; *Retrieved from https://en.wikipedia.org/wiki/Scanning_electron_microscope.*

[5] Cantafio, C., *Scanning Electron Microscope Usage and Analysis of Metal Fatigue*

in Mead Silver Paperclips, A Physics 499 Research Project Under Dr. Joseph M. Hoffman and Dr. David Morton, **1998**, Chapter 1.

[6] Brydson, R., *Aberration-Corrected Analytical Electron Microscopy*, John Wiley & Sons and RMS-Royal Microscopical Society, **2011**, 2.7.

[7] Coats, A. W.; Redfern, J. P. *Analyst* **1963**, *88*, 906.

[8] Gardiner, D. J., Graves, P. R., *Practical Raman Spectroscopy*, Springer. **1989**, Chapter 1.

[9] Shimadzu, Diffuse Reflectance Measurement; *Retrieved from https://shimadzu.com.au/diffuse-reflectance-measurement*.

[10] Bai, Y.; Yu, H.; Li, Z.; Amal, R.; Lu, G. Q.; Wang, L. Z. *Adv. Mater.* **2012**, *24*, 5850.

[11] Bai, Y.; Xing, Z.; Yu, H.; Li, Z.; Amal, R.; Wang, L. Z. *ACS Appl. Mater. Interfaces* **2013**, *5*, 12058.

CHAPTER 3 Aqueous Route for Preparation of Surfactant-Free Copper Selenide Nanowires

Uniform surfactant-free copper selenide ($Cu_{2-x}Se$) NWs were prepared via an aqueous route. The effects of reaction parameters such as Cu/Se precursor ratio, Se/NaOH ratio, and reaction time on the formation of NWs were comprehensively investigated. The results show that $Cu_{2-x}Se$ NWs were formed through the assembling of CuSe nanoplates, accompanied by their self-redox reactions. The resultant $Cu_{2-x}Se$ NWs were explored as a potential thermoelectric candidate in comparison with commercial copper selenide powder. Both synthetic and commercial samples have a similar performance and their figures of merit (ZT) are 0.29 and 0.38 at 750 K, respectively.

3.1 Introduction

Nano-scale copper selenides exhibit some unusual properties due to the large surface area, a high ratio of surface atoms, and quantum confinement effects. An example is a cuprous selenide (Cu_2Se) nanoparticles, which are easily oxidized into non-stoichiometric $Cu_{1.8}Se$, and become into a surprisingly good *p*-type semiconductor with over 3000 times of enhancements in electrical conductivity.[1] In order to tune the properties of nano-scale copper selenides, a number of techniques and strategies, such as hydro- or solvo-thermal approach,[1-3] sonochemistry,[4] electrochemical-deposition,[5] microwave-assistant route,[6] ball milling technique,[7] and chemical welding method,[8] have

been developed to prepare nanocrystals,[9] nanotubes/wires,[2,10-12] nanocages,[13] dendrimers,[3,14] and nanosheets[15] with well-defined size, morphology, crystal structure, and composition. However, most synthesizes are complicated and the resultant nanostructures are stabilized with organic ligands, which could influence their properties (e.g. conductivity) and have to be removed in some applications. There are few reports on synthesis of surfactant-free copper selenide nanostructures, which can be used without post surface treatment.[16]

In comparison with 0D and bulk counterparts, 1D semiconductor nanostructures have many unique characteristics including asymmetric structures, intrinsic polarization anisotropies, long (macroscopic) length, band and/or ballistic transport etc.[17-19] The electrons in nanowires are quantum confined laterally and thus occupy energy levels that are different from the traditional continuum of energy levels or bands found in bulk analogues. 1D semiconductor nanostructures show great potential in the fabrication of various optical and electronic nanodevices.[20] For example, stoichiometric cuprous selenide nanowires have been utilized to fabricate catalytic electrode for oxygen reduction reaction,[21] and non-stoichiometric ones have been used to construct the photoluminescence type sensor of humidity.[22] In this work, uniform surfactant-free $Cu_{2-x}Se$ NW bundles on gram-scale via an aqueous route were successfully synthesized. The resultant $Cu_{2-x}Se$ NW bundles have diameters of 100-300 nm and lengths of tens of micrometers. The evolution of $Cu_{2-x}Se$ NWs demonstrates they were formed through the

assembling of CuSe nanoplates accompanied by a redox reaction. This gram-scale synthesis offers enough pristine NWs for exploring their properties and potential applications. The NWs were sintered into pellets for investigation of their thermoelectric properties, which show higher electrical conductivity, smaller Seebeck coefficient, and lower thermal conductivity than commercial Cu_2Se powder which was sintered and measured under the same conditions. The obtained *ZT* is comparable with that of the commercial sample and reach to 0.29 at 480 ˚C.

3.2 Experimental section

3.2.1 Synthesis of $Cu_{2-x}Se$ NWs

In a typical synthesis, 0.1580 g Se powder, 4.800 g NaOH (Se/NaOH = 1/60), and 20 mL Milli-Q water were loaded into a 100 mL round-bottomed flask. The mixture was heated to 90 ˚C under magnetic stirring. After the selenium was completely dissolved (deep red), 1.5 mL $Cu(NO_3)_2$ aqueous solution (0.5 M) [$Se/Cu(NO_3)_2$ = 2.5/1] was quickly added into the selenium solution. The black suspension was transferred into a 100 mL beaker and then put into an oven at 100 ˚C until the water was completely evaporated (18 h). The black precipitate was washed with hot distilled water and centrifuged. The washing/centrifugation was repeated several times, and the purified sample was dried at 60 ˚C to constant weight. The yield is around 90 %.

3.2.2 Crystal structure and morphology evolution of $Cu_{2-x}Se$ NWs

In order to investigate the evolution of the morphology and crystal structure, a group of experiments was designed to prepare $Cu_{2-x}Se$ NWs and collect the intermediate samples at different reaction times. The preparation procedure was the same as in the above process. Typically 1.5792 g Se powder, 48.0000 g NaOH (Se/NaOH = 1/60), and 200 mL Milli-Q water were loaded into a 500 mL sealed round-bottomed flask. After the selenium was completely dissolved at 90 ˚C, the solution was equally divided into 10 beakers (20 mL in each beaker). After adding the same amount of 0.5 M $Cu(NO_3)_2$ aqueous solution (1.5 mL) [$Se/Cu(NO_3)_2$ = 2.5/1], all beakers were kept in an oven at 100 ˚C, with the individual samples taken out at different times (i.e. 1 min, 40 min, 60 min, 90 min, 3.5 h, 5 h, 7 h, 9 h, 13 h, and 18 h). The resultant products were purified using the same process as described above.

3.2.3 Synthesis of $Cu_{2-x}Se$ from as-synthesized CuSe in alkaline solution

CuSe powder was synthesized by a solvent-mediated method.[23] 0.63 g of copper metal powder (0.01 mol) and 0.79 g of selenium powder (0.01 mol) were initially stirred magnetically for 10 minutes, followed by the addition of 20 mL of 2-mercaptoethanol to it. The suspension was subjected to a vigorous magnetic stirring for 24 h at room temperature. The resultant products were purified and dried. 0.2850 g CuSe powder was dispersed into 20 mL NaOH solution (0.12 M) (CuSe/NaOH = 1/60). The suspension

was kept in an oven at 100 ˚C for 18 h. The resultant products were purified using the same process as described above.

3.3 Results and discussion

3.3.1 Results of synthesized $Cu_{2-x}Se$ NWs

Figure 3.1 shows the XRD pattern, and SEM and TEM images of the resultant NWs. Compared to the standard diffraction peaks of copper selenide, all the peaks of NWs are matched well with those of fcc $Cu_{2-x}Se$ (JCPDS 06-0680) with a lattice constant of 0.5728 nm [Figure 3.1(a)]. The strong and sharp diffraction peaks suggest that the as-synthesized NWs are well crystallized. The absence of other peaks indicates high purity and the single-phase nature of these NWs. The SEM image in Figure 3.1(b) clearly shows a large quantity of uniform bundles with lengths up to tens of micrometers and diameters of 100-300 nm. A typical bundle is displayed in Figure 3.1(b) as an inset. The TEM image in Figure 3.1(c) also confirms that these nanobundles have a uniform diameter and that they are made up of many thin NWs. The HRTEM image clearly shows the lattice fringes with a spacing of 0.33 nm [Figure 3.1(d)], which matches well with that of (111) planes of $Cu_{2-x}Se$. The EDS analysis shows that the ratio of copper to selenium in these NW bundles is 1.84, which is higher than the initial precursor ratio (Cu/Se = 1/2.5) and further confirms that they are copper-deficient.

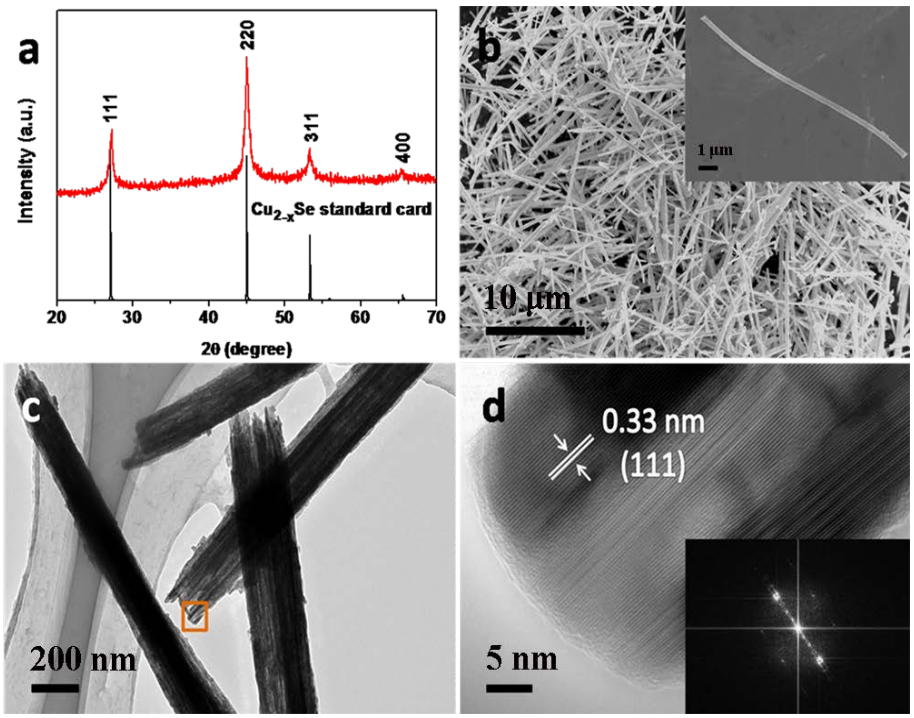

Figure 3.1 (a) XRD pattern of surfactant-free $Cu_{2-x}Se$ NW bundles. The vertical lines mark the line positions of the $Cu_{2-x}Se$ standard (JCPDS 06-0680). (b) SEM images of the resultant $Cu_{2-x}Se$ NW bundles. Inset is a typical image of an individual bundle. (c) TEM image of the $Cu_{2-x}Se$ NW bundles, showing that each bundle is composed of many thin NWs. (d) HRTEM image of the selected area in c. Insets are FFT of HRTEM image of the selected area in c.

3.3.2 Formation evolution $Cu_{2-x}Se$ NWs

In order to understand the formation mechanism of the $Cu_{2-x}Se$ NWs, the experiment was repeated and collected the intermediate products at different reaction times. Figure 3.2 shows the XRD patterns of the samples collected at 1 min, 40 min, 3.5 h, 5 h, and 18

h. When the $Cu(NO_3)_2$ solution reacted with Se-precursor solution for 1 min, the XRD pattern of the product [Figure 3.2(a)] matched that of hexagonal CuSe (JCPDS 34-0171). After 40 minutes reaction, the XRD pattern of the products is still indexed to hexagonal CuSe [Figure 3.2(b)]. When the mixture reacted for 3.5 h, the intermediate product is a mixture of hexagonal CuSe and cubic $Cu_{2-x}Se$ [Figure 3.2(c)]. The diffraction peaks marked with * arise from $Cu_{2-x}Se$ (JCPDS 06-0680). The intermediate product collected at 5 h is also a mixture of CuSe and $Cu_{2-x}Se$ [Figure 3.2(d)], but the content of CuSe is notably decreased due to the formation of $Cu_{2-x}Se$. The final product collected at 18 h shows single phase $Cu_{2-x}Se$ [Figure 3.2(e)], which demonstrates the complete transformation of CuSe into $Cu_{2-x}Se$. The transformation of CuSe into $Cu_{2-x}Se$ is also supported by the variation of the Cu/Se molar ratio in these samples, as determined by ICP-AES and shown in Table 3.1. The results clearly show the increase in the Cu/Se molar ratio during the transformation process. When the $Cu(NO_3)_2$ solution was added into the alkaline selenium solution, the black precipitate formed immediately and its Cu/Se molar ratio was 1.01, which means the main product is CuSe. When the reaction time increased from 1 min, through 40 min, 90 min, 3.5 h, 5 h, and 7 h, to 18 h, the Cu/Se molar ratio in these samples correspondingly increased from 1.01, through 1.06, 1.35, 1.51, 1.51, and 1.52, to 1.65.

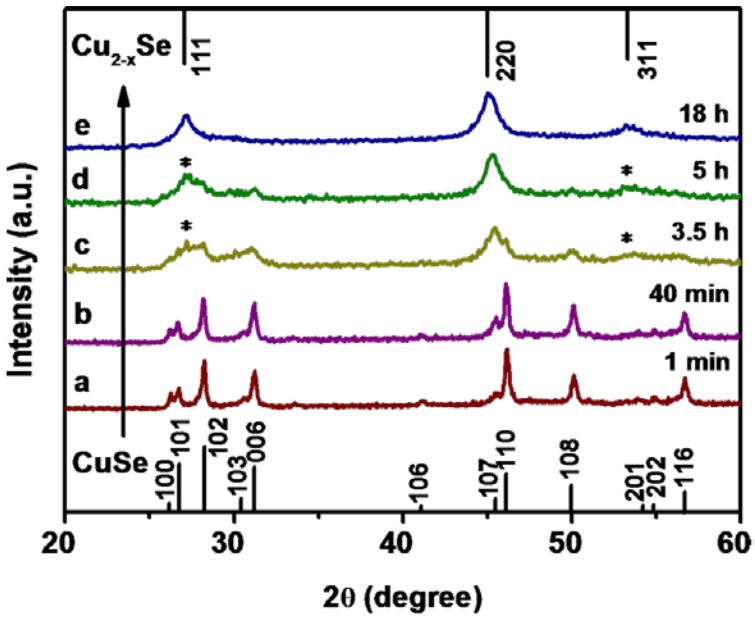

Figure 3.2 XRD patterns of samples collected at (a) 1 min, (b) 40 min, (c) 3.5 h, (d) 5 h, and (e) 18 h, showing the transformation of the crystal structure from hexagonal CuSe into cubic $Cu_{2-x}Se$. The diffraction peaks marked with * arise from $Cu_{2-x}Se$ (JCPDS 06-0680).

Table 3.1 Ratio of Cu to Se in the products collected at different reaction time, as determined by ICP-AES.

	1 min	40 min	90 min	3.5 h	5 h	7 h	18 h
Copper (mg/L)	28	23	26	23	26	25	39
Selenium (mg/L)	35	27	24	19	21	20	29
Ratio of Cu to Se	1.01	1.06	1.35	1.51	1.51	1.52	1.65

The above results support the formation of non-stoichiometric $Cu_{2-x}Se$ NWs, and the partial reduction of Cu^{2+} into Cu^{+} during sample preparation. XPS was used to determine the ratio of Cu^{2+}/Cu^{+} in these samples, and the whole XPS survey and spectra of Cu $2p_{3/2}$ are presented in Figure 3.3 (a-c). A slight shift in the binding energy of Cu $2p_{3/2}$ from 932.07 eV to 931.52 eV was observed when the reaction time increased from 1 min to 18 h [Figure 3.3(b)]. The small shift indicates the difficulty in distinguishing the contributions from Cu^{2+} and Cu^{+}. The binding energy of Cu $2p_{3/2}$ can be fitted into three peaks at 931.98 eV (CuSe), 931.48 eV (Cu_2Se), and 933.87 eV (CuO) [Figure 3.3(c)].

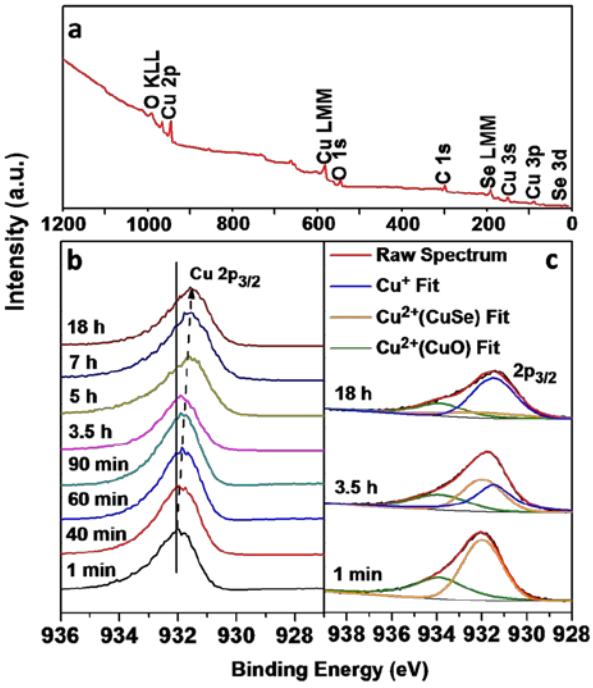

Figure 3.3 (a) Whole survey of as prepared $Cu_{2-x}Se$ NWs; (b) Binding energies of Cu $2p_{3/2}$ in the products collected from 1 min to 18 h; (c) XPS spectra of the Cu $2p_{3/2}$ region for selected samples with peak fits for Cu^{2+} and Cu^{+}.

At the very beginning of the reaction, there are only Cu^{2+} peaks. The Cu^{2+}/Cu^{+} ratio from CuSe and Cu_2Se in the samples collected at 40 min and 7 h decreased from 3.88 to 0.33 [Figure 3.4(b-g)], which means that the reduction of Cu^{2+} into Cu^{+} occurred upon the addition of copper nitrate solution to the Se-precursor solution. The absence of a contribution from CuSe in the sample collected at 18 h supports the complete transformation of CuSe into $Cu_{2-x}Se$. The small peak at 933.87 eV (CuO) in all samples is attributed to surface oxidation.[1,24-25]

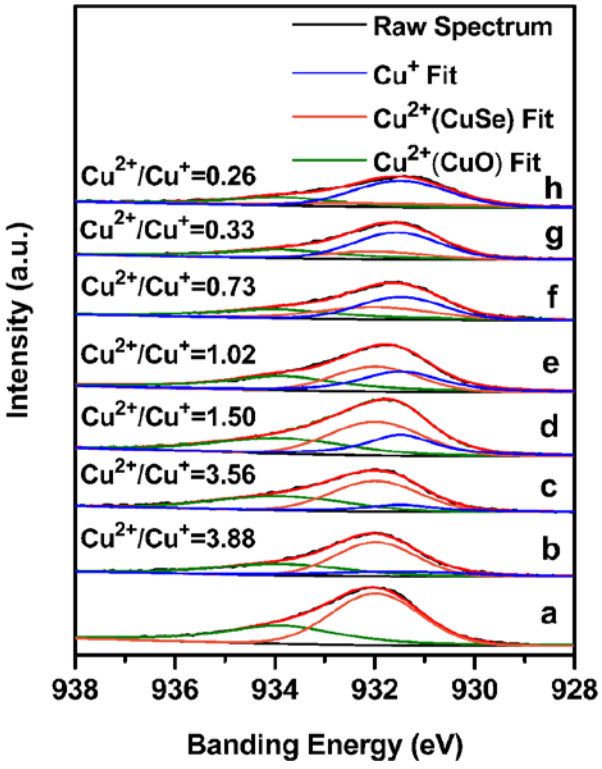

Figure 3.4 XPS spectra of the Cu $2p_{3/2}$ region for samples with peak fits for Cu^{2+} and Cu^{+} and molar ratios of Cu^{2+}/Cu^{+}: (a) 1 min; (b) 40 min; (c) 60 min; (d) 90 min; (e) 3.5 h; (f) 5 h; (g) 7 h; and (h) 18 h, showing the transformation of CuSe into $Cu_{2-x}Se$.

The evolution of the morphology during the transformation was monitored by SEM. Figure 3.5 shows SEM images of eight samples collected at different reaction times, 1 min, 40 min, 60 min, 90 min, 3.5 h, 5 h, 7 h, and 18 h, respectively. At the first stage (i.e., from 1 min to 60 min), the initially formed CuSe nanoparticles grow into hexagonal nanoplates with a size of 100-400 nm, as shown in Figure 3.5(a-c). At the second stage (i.e., from 60 min to 5 h), the hexagonal nanoplates become stacked together and self-assemble into a one-dimensional structure with a rough surface [Figure 3.5(d-f)]. The products are a mixture of CuSe and $Cu_{2-x}Se$, as proved by their XRD patterns in Figure 3.2. At the last stage (i.e., from 5 h to 18 h), the rough NW bundles become smoother [Figure 3.5(g-h)], which is accompanied by the complete transformation of CuSe into $Cu_{2-x}Se$ (Figure 3.2). The final NW bundles are about 100-300 nm in diameter and tens of micrometers in length.

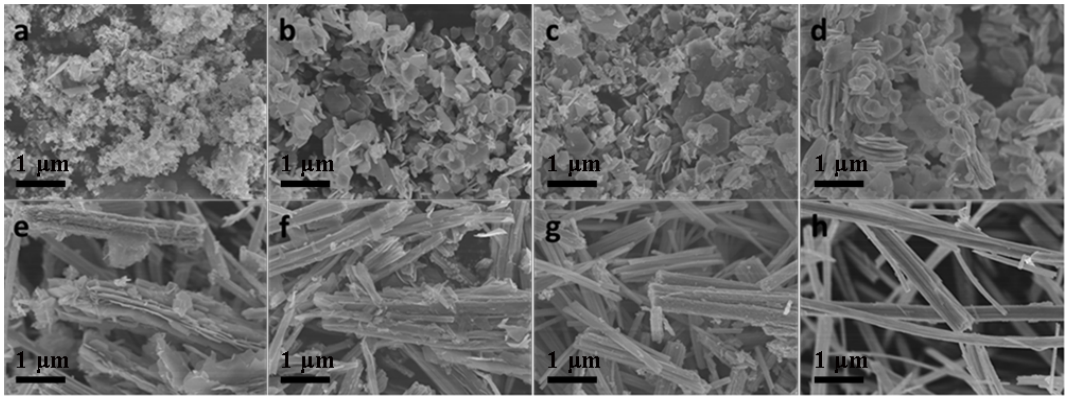

Figure 3.5 SEM images of the samples collected at (a) 1 min, (b) 40 min, (c) 60 min, (d) 90 min, (e) 3.5 h, (f) 5 h, (g) 7 h, and (h) 18 h, showing the evolution of the morphology of the $Cu_{2-x}Se$ NW bundles.

3.3.3 Effects of reaction parameters

It should be noted that the morphology and composition of the NWs are strongly influenced by the reaction parameters. Figure 3.6 shows the XRD patterns of products prepared using different molar ratios of sodium hydroxide to selenium powder (i.e., NaOH/Se). When a high molar ratio of NaOH/Se (i.e., 60/1) is used [Figure 3.6(a)], the final product is pure $Cu_{2-x}Se$, and its XRD pattern is consistent with the standard profile of $Cu_{2-x}Se$ indexed with JCPDS 06-0680. When the molar ratio is decreased from 60/1 to 30/1, the product obtained is a mixture of $Cu_{2-x}Se$, Cu_2O, and CuO. The diffraction peaks of Cu_2O and CuO are marked with # and º, respectively in Figure 3.6(b).

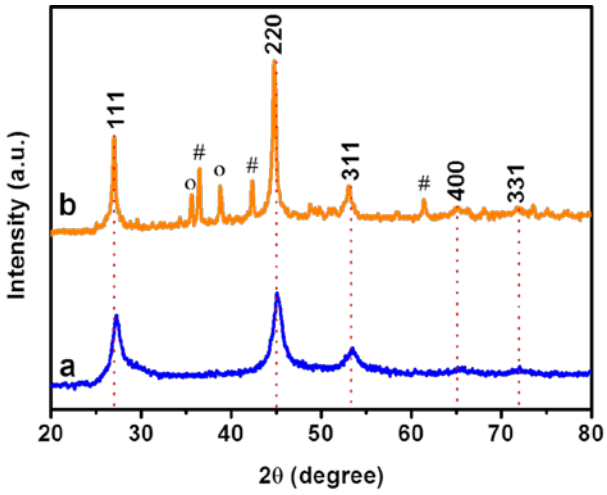

Figure 3.6 XRD patterns of the products prepared with the different molar ratio of NaOH and Se: (a) 60/1; (b) 30/1. The diffraction peaks of Cu_2O and CuO are marked with # and º, respectively.

Their SEM images in Figure 3.7 show that the sample prepared with a high NaOH/Se ratio has uniform NW bundles [Figure 3.7(a)], while the sample obtained with a low NaOH/Se ratio contains some big plates and particles in addition to the NW bundles [Figure 3.7(b)]. This result demonstrates the importance of the NaOH/Se ratio for the formation of uniform NWs.

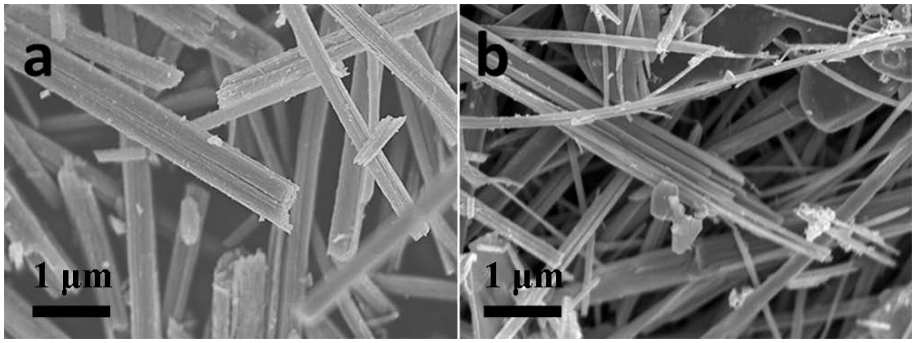

Figure 3.7 SEM images of the products prepared from different molar ratios of NaOH to Se: (a) 60/1; (b) 30/1.

In addition, the molar ratio of the Se powder to the $Cu(NO_3)_2$ also strongly affects the product morphology and composition. Figure 3.8 shows the XRD patterns of products prepared by adding different amounts of copper nitrate to the same amount of alkaline selenium aqueous solution, i.e., the Se/Cu ratio is varied from 0.5/1, though 1/1, 2.5/1, and 5/1, to 10/1. In the case of the lowest Se/Cu precursor ratio (i.e., 0.5/1), the small amount of Se is not enough for a complete reaction with $Cu(NO_3)_2$, and the excess $Cu(NO_3)_2$ is hydrolysed and dehydrated to form Cu_2O, whose diffraction peaks are labelled with $^{\Delta}$ in Figure 3.8(a). In the opposite case (i.e., Se/Cu ratio of 10/1), the large

amount of Se leads to the formation of CuSe [marked with ♦ in Figure 3.8(e)] mixed with $Cu_{2-x}Se$. When the precursor molar ratio is in the range of 1/1 to 5/1, the final products obtained are pure $Cu_{2-x}Se$, as confirmed by their XRD patterns are shown in Figure 3.8(b-d). Their SEM images in Figure 3.9 demonstrate that uniform NWs can be only obtained from a molar ratio of 2.5/1. Therefore, the optimal molar ratio of Se powder to $Cu(NO_3)_2$ is 2.5/1.

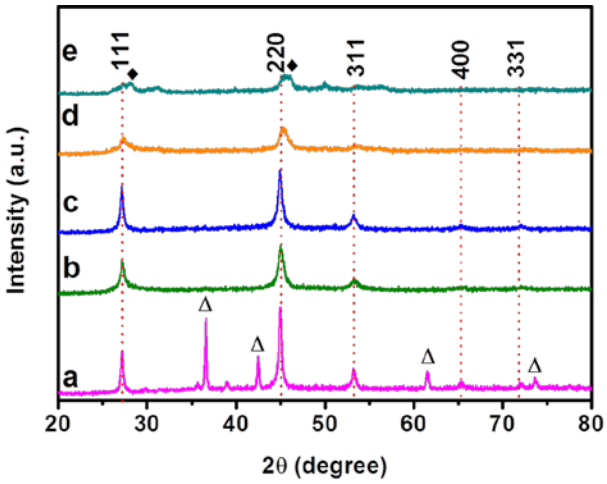

Figure 3.8 XRD patterns of the samples prepared using different molar ratios of Se to $Cu(NO_3)_2$: (a) 0.5/1; (b) 1/1; (c) 2.5/1; (d) 5/1; (e) 10/1. Δ marks Cu_2O peaks, ♦ CuSe peaks.

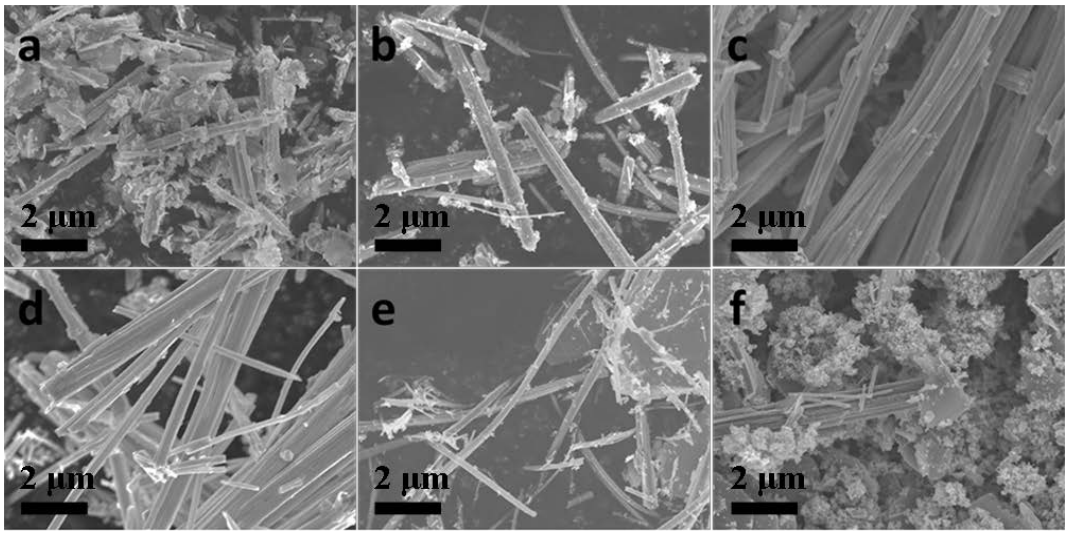

Figure 3.9 SEM images of the products prepared using different molar ratio of Se to $Cu(NO_3)_2$: (a) 0.5/1; (b) 1/1; (c, d) 2.5/1; (e) 5/1; (f) 10/1.

3.3.4 Formation mechanism $Cu_{2-x}Se$ NWs

On the basis of previous results, the following mechanism was proposed. After the $Cu(NO_3)_2$ solution is added into the Se precursor solution, the competition among reactions (3.2)–(3.4) is strongly dependent on the solubility constants of CuSe (K_{sp} = 7.94 × 10^{-49}), $CuSeO_3$ (K_{sp} = 2.1 × 10^{-8}), and Cu_2Se (K_{sp} = 1.58 × 10^{-61}).[12] For the same Se^{2-} concentration, the minimum Cu^{2+} concentration required for precipitation of CuSe is smaller than that required for Cu_2Se and $CuSeO_3$. Thus, CuSe was first precipitated after the addition of $Cu(NO_3)_2$ solution to Se solution. The formation ΔG can be expressed by Equation (3.5), in which R is the universal gas constant, T is the temperature, K_{sp} is the solubility of CuSe. J_{sp} is expressed by Equation (3.6), where C_{Cu}^{2+} and C_{Se}^{2-} represent the concentration of Cu^{2+} and Se^{2-}, respectively.

$$3Se + 6NaOH \rightarrow 2Na_2Se + Na_2SeO_3 + 3H_2O \quad (3.1)$$

$$Cu(NO_3)_2 + Na_2Se \rightarrow CuSe + 2NaNO_3 \quad (3.2)$$

$$Cu(NO_3)_2 + Na_2SeO_3 \rightarrow CuSeO_3 + 2NaNO_3 \quad (3.3)$$

$$2Cu(NO_3)_2 + 2Na_2Se \rightarrow Cu_2Se + Se + 4NaNO_3 \quad (3.4)$$

$$\Delta G = RT \times \ln J_{sp}/ K_{sp} \quad (3.5)$$

$$J_{sp}=C^2_{Cu^{2+}} \times C^2_{Se^{2-}} \quad (3.6)$$

$$(2-x)CuSe \rightarrow Cu_{2-x}Se + (1-x)Se \quad (3.7)$$

The high concentrations of Cu^{2+} and Se^{2-}, and small K_{sp} (7.94×10^{-49}) of CuSe indicate a large ΔG for the formation of CuSe nanoparticles. In addition, from a viewpoint of nucleation and growth of nanocrystals, high precursor concentration means the fast nucleation and growth process, which leads to a broad particle size distribution. Therefore, a mixture of nanoparticles and nanoplates is obtained upon the addition of copper nitrate solution into selenium precursor solution. The nanoparticles can be transformed into nanoplates through the Oswald ripening process due to the intrinsicly layered structure.

The transformation of nanoplates into NWs is induced by water evaporation, which increases the concentration of nanoplates and promotes nuclei self-assembly in the longitudinal direction (i.e., [110] direction). In the presence of excessive Se^{2-} ions which have strong reducing process. This process can be viewed as a chemical etching process of CuSe nanoplates by Se^{2-} anions from the solution in a redox reaction. At the same

time, the produced $Cu_{2-x}Se$ nuclei grew into nanorods along [110] direction. With the prolongation of reaction time, these split CuSe nanoplates were further etched, and converted to form fine $Cu_{2-x}Se$ NWs. The transformation of CuSe into $Cu_{2-x}Se$ by the self-redox reaction can be easily achieved in strong NaOH solution [formula (3.7)], which has been proved by treating CuSe powder in the same NaOH solution without other chemicals (Figure 3.10).

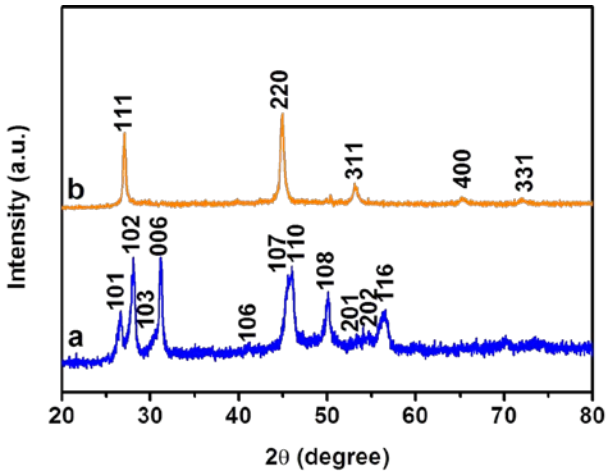

Figure 3.10 XRD patterns of (a) as-prepared CuSe powders, (b) $Cu_{2-x}Se$ powders obtained through self-redox reaction in strong NaOH solution.

3.3.5 Thermoelectric performance

As mentioned previously, $Cu_{2-x}Se$ nanostructures show high electrical conductivity arising from pronounced copper-deficiency. Bulk $Cu_{2-x}Se$ and Cu_2Se have potential in thermoelectric application due to the liquid-like behaviour of Cu^+ ions at high temperature. Therefore, the thermoelectric properties of $Cu_{2-x}Se$ NWs with commercial

Cu_2Se powders were compared. The reason Cu_2Se was selected is that there is no commercial $Cu_{2-x}Se$ powder and it is very difficult to prepare stoichiometric Cu_2Se NWs using the same approach. Nevertheless, the comparison between them would demonstrate the nanostructure effects on their thermoelectric properties.

As-synthetic $Cu_{2-x}Se$ powders were weighted and sintered as a pellet by using SPS technique. The resultant pellet was cut into pieces for thermoelectric measurement (Figure 3.11). The commercial powders were sintered under the same conditions and cut into pieces with a similar size and then measured under the same conditions.

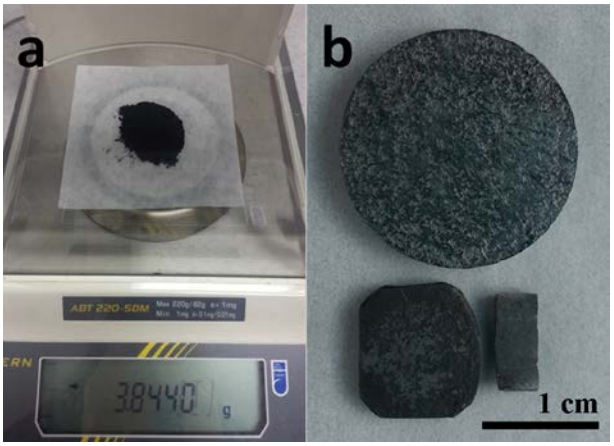

Figure 3.11 (a) As-synthetic $Cu_{2-x}Se$ powders on digital scale. (b) Sintered pellet (up), small piece after thermal diffusion measurement (down left), and small piece after electrical conductivity and Seebeck coefficiency measurement (down right).

The electrical conductivity [Figure 3.12(a)] of the $Cu_{2-x}Se$ sample is around 6800 S/cm at room temperature and decreases quickly to about 2200 S/cm at 480 ˚C, which is higher than that of commercial Cu_2Se powder at room temperature (2600 S/cm) and at 480 ˚C

(1200 S/cm), respectively. The higher electrical conductivity of $Cu_{2-x}Se$ is due to its higher copper-deficiency compared to commercial Cu_2Se, which is consistent with the previous report.[26] Due to its excellent electrical conductivity, the Seebeck coefficient [Figure 3.12(b)] of $Cu_{2-x}Se$ is lower than that of the commercial Cu_2Se (i.e. 35 μV/K at room temperature and 80 μV/K at 480 ˚C). Having the same trend as the Seebeck coefficient, this sample has a power factor [Figure 3.12(c)] of 0.3 $\mu Wcm^{-1}K^{-2}$ at room temperature and 5 $\mu Wcm^{-1}K^{-2}$ at 480 ˚C, lower than that of commercial sample.

To determine the thermal conductivity of samples, their *Cp* were measured and shown in Figure 3.12(d). A sharp endothermal peak at around 140 ˚C was observed in both synthetic and commercial samples, which is consistent with the previous reports.[7] The overall thermal conductivity can be calculated by using Equation (2.3). The resultant total thermal conductivity [Figure 3.12(e)] of $Cu_{2-x}Se$ sample from room temperature to 200 ˚C is higher than that of the commercial Cu_2Se sample, however, it is slightly lower in the range of 200-480 ˚C. The lower total thermal conductivity of synthetic $Cu_{2-x}Se$ could be due to the presence of nanoprecipitates in the pellet, which can effectively improve the phonon scattering and decrease the thermal conductivity.

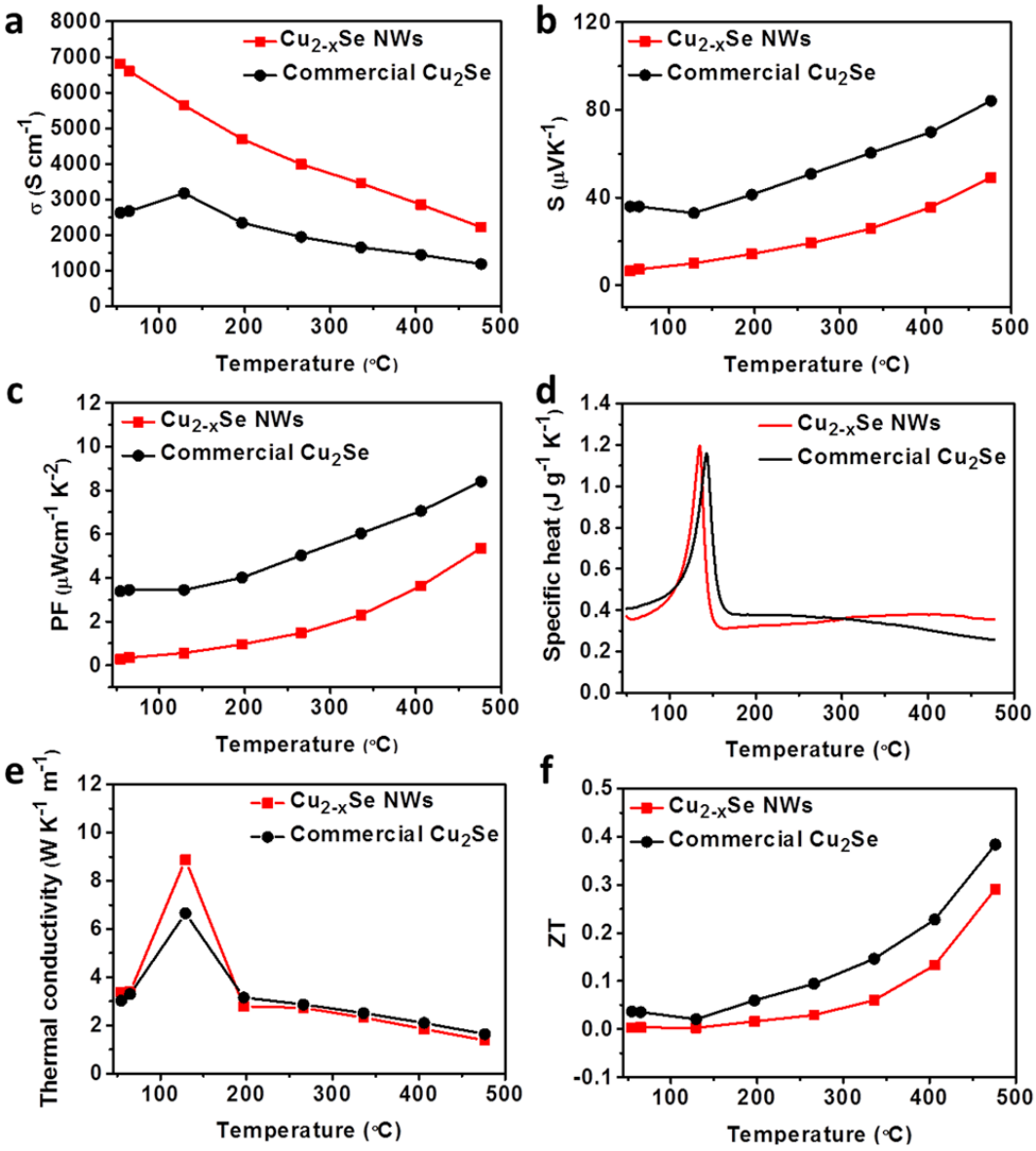

Figure 3.12 Temperature dependent thermoelectric properties of $Cu_{2-x}Se$ NWs bundles and commercial Cu_2Se powder: (a) electrical conductivity; (b) Seebeck coefficient; (c) power factor; (d) specific heat (C_p); (e) thermal conductivity; and (f) figure-of-merit calculated using Equation (1.4).

The SEM images of pellets made from $Cu_{2-x}Se$ NWs and commercial Cu_2Se powder in Figure 3.13 clearly show that the $Cu_{2-x}Se$ NWs were melted into nanoprecipitates at high temperature (430 ˚C) and high pressure (65 MPa) after SPS sintering, while the commercial Cu_2Se powder was pressed into a bulk layer structure. In addition, the pronounced copper-deficiency in the synthetic sample leads to more vacancies, which are also responsible for its lower thermal conductivity. As shown in Table 3.2, the Cu/Se ratio of the synthetic sample is increased from 1.65 in initial $Cu_{2-x}Se$ nanowires to 1.72 in sintered pellet, and to 1.92 after thermoelectric measurements. Similarly, the Cu/Se ratio of the commercial sample increased from 1.97 in initial powder to 2.09 in its sintered pellet, and to 2.03 after measurements. This sharp peak observed in *Cp* could be due to the phase transition.

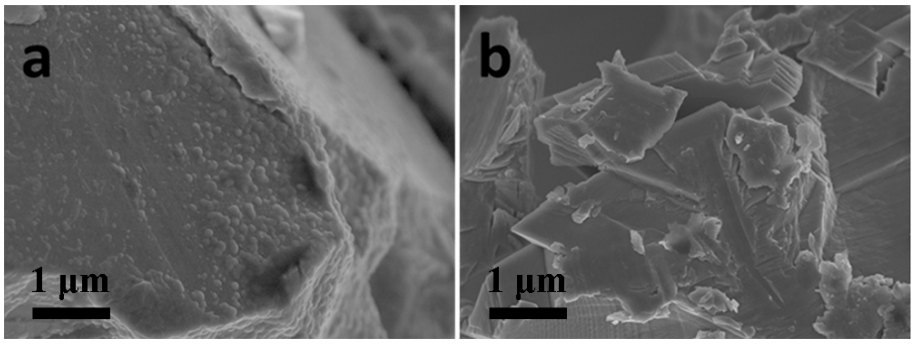

Figure 3.13 SEM images of cross-sections of (a) $Cu_{2-x}Se$ and (b) Cu_2Se pellets after sintering at 430 ˚C under 65 MPa by the spark plasma sintering technique.

Table 3.2 Ratio of Cu to Se in synthetic $Cu_{2-x}Se$ samples (A) and commercial Cu_2Se samples (B) determined by ICP-AES: numbers 1, 2, and 3 represent original powder, pellet after SPS sintering, and pellet after thermoelectric measurement.

	A1	A2	A3	B1	B2	B3
Copper (mg/L)	39	58	48	87	110	150
Selenium (mg/L)	29	42	31	54	68	92
Ratio of Cu to Se	1.65	1.72	1.92	1.97	2.09	2.03

The figure of merit for synthetic and commercial samples can be calculated by Equation (1.1).[27-29] The calculated *ZT* values of $Cu_{2-x}Se$ and Cu_2Se samples were plotted in Figure 3.12(f), a slight decrease in *ZT* at 140 ˚C was observed due to the presence of a sharp endothermal peak at this temperature [Figure 3.12(d)]. The *ZT* values of synthetic and commercial samples increase with the increase of temperature, and reach 0.29 and 0.38 at 480 ˚C, respectively. These results are similar to that of $Cu_{2-x}Se$ ($0 \leq x \leq 0.25$) prepared from a high-temperature solid state reaction, in which the highest *ZT* is from Cu_2Se with a value of 0.38 at 480 ˚C.[8,26]

3.4 Conclusions

In summary, surfactant-free $Cu_{2-x}Se$ NW bundles with lengths of tens of micrometers and diameters of 100–300 nm have been successfully synthesized on a large scale by an aqueous approach. The NW bundles are composed of many thin $Cu_{2-x}Se$ NWs. The evolution of the morphology shows that the formation of $Cu_{2-x}Se$ nanobundles arises from the assembly of CuSe nanoplates induced by water evaporation, accompanied by the self-redox reduction of CuSe. The formation of $Cu_{2-x}Se$ nanobundles is strongly influenced by the molar ratio of sodium hydroxide to selenium powder and the molar ratio of selenium powder to copper nitrate. The resultant $Cu_{2-x}Se$ nanobundles were sintered into a pellet and tested for thermoelectric application in comparison with the commercial Cu_2Se powder. The results show that the synthetic sample has a temperature-dependent *ZT* comparable to that of commercial sample, and reach to 0.29 at 480 ˚C. Our research provides a straight way to prepare surfactant-free copper selenide NWs for energy conversion.

References

[1] Riha, S. C.; Johnson, D. C.; Prieto, A. L. *J. Am. Chem. Soc.* **2011**, *133*, 1383.

[2] Zhang, Y.; Hu, C. G.; Zheng, C. H.; Xi, Y.; Wan, B. Y. *J. Phys. Chem. C* **2010**, *114*, 14849.

[3] Li, D. P.; Zheng, Z.; Lei, Y.; Ge, S. X.; Zhang, Y. D.; Zhang, Y. G.; Wong, K. W.;

Yang, F. L.; Lau, W. M. *CrystEngComm* **2010**, *12*, 1856.

[4] Zhao, Y. X.; Pan, H. C.; Lou, Y. B.; Qiu, X. F.; Zhu, J. J.; Burda, C. *J. Am. Chem. Soc.* **2009**, *131*, 4253.

[5] Yu, R.; Ren, T.; Sun, K. J.; Feng, Z. C.; Li, G. N.; Li, C. *J. Phys. Chem. C* **2009**, *113*, 10833.

[6] Cao, X. B.; Zhao, C.; Lan, X. M.; Gao, G. J.; Qian, W. H.; Guo, Y. *J. Phys. Chem. C* **2007**, *111*, 6658.

[7] Yu, B.; Liu, W. S.; Chen, S.; Wang, H.; Wang, H. Z.; Chen, G.; Ren, Z. F. *Nano Energy* **2012**, *1*, 472.

[8] Liu, H. L.; Shi, X.; Xu, F. F.; Zhang, L. L.; Zhang, W. Q.; Chen, L. D.; Li, Q.; Uher, C.; Day, T.; Snyder, G. J. *Nat. Mater.* **2012**, *11*, 422.

[9] Deka, S.; Genovese, A.; Zhang, Y.; Miszta, K.; Bertoni, G.; Krahne, R.; Giannini, C.; Manna, L. *J. Am. Chem. Soc.* **2010**, *132*, 8912.

[10] Xu, J.; Zhang, W. X.; Yang, Z. H.; Yang, S. H. *Inorg. Chem.* **2008**, *47*, 699.

[11] Jiang, Y.; Wu, Y.; Xie, B.; Zhang, S. Y.; Qian, Y. T. *Nanotechnology* **2004**, *15*, 283.

[12] Xu, J.; Zhang, W. X.; Yang, Z. H.; Ding, S. X.; Zeng, C. Y.; Chen, L. L.; Wang, Q.; Yang, S. H. *Adv. Funct. Mater.* **2009**, *19*, 1759.

[13] Cao, H. L.; Qian, X. F.; Zai, J. T.; Yin, J.; Zhu, Z. K. *Chem. Commun.* **2006**, *43*, 4548.

[14] Zhu, J. B.; Li, Q. Y.; Bai, L. F.; Sun, Y. F.; Zhou, M.; Xie, Y. *Chem. Eur. J.* **2012**, *18*, 13213.

[15] Xie, Y.; Zheng, X. W.; Jiang, X. C.; Lu, J.; Zhu, L. Y. *Inorg. Chem.* **2002**, *41*, 387.

[16] Zhang, W. X.; Zhang, X. M.; Zhang, L.; Wu, J. X.; Hui, Z. H.; Cheng, Y. W.; Liu, J. W.; Xie, Y.; Qian, Y. T. *Inorg. Chem.* **2000**, *39*, 1838.

[17] Li, Z.; Cheng, L. N.; Sun, Q.; Zhu, Z. H.; Riley, M. J.; Aljada, M.; Cheng, Z. X.; Wang, X. L.; Hanson, G. R.; Qiao, S. Z.; Smith, S. C.; Lu, G. Q. *Angew. Chem., Int. Edit.* **2010**, *49*, 2777.

[18] Li, Z.; Kurtulus, O.; Fu, N.; Wang, Z.; Kornowski, A.; Pietsch, U.; Mews, A. *Adv. Funct. Mater.* **2009**, *19*, 3650.

[19] Myalitsin, A.; Strelow, C.; Wang, Z.; Li, Z.; Kipp, T.; Mews, A. *ACS Nano* **2011**, *5*, 7920.

[20] Li, Z.; Du, A. J.; Sun, Q.; Aljada, M.; Zhu, Z. H.; Lu, G. Q. *Nanoscale* **2012**, *4*, 1263.

[21] Liu, Y.; Deng, Y. H.; Sun, Z. K.; Wei, J.; Zheng, G. F.; Asiri, A. M.; Khan, S. B.; Rahman, M. M.; Zhao, D. Y. *Small* **2013**, *9*, 2702.

[22] Jagminas, A.; Juskenas, R.; Gailiute, I.; Statkute, G.; Tomasiunas, R. *J. Cryst. Growth* **2006**, *294*, 343.

[23] Kumar, P.; Gusain, M.; Nagarajan, R. *Inorg. Chem.* **2012**, *51*, 7945.

[24] Sykora, M.; Koposov, A. Y.; McGuire, J. A.; Schulze, R. K.; Tretiak, O.; Pietryga,

J. M.; Klimov, V. I. *ACS Nano* **2010**, *4*, 2021.

[25] Mcintyre, N. S.; Cook, M. G. *Anal. Chem.* **1975**, *47*, 2208.

[26] Xiao, X. X.; Xie, W. J.; Tang, X. F.; Zhang, Q. J. *Chin. Phys. B* **2011**, *20*, 087201.

[27] Poudel, B.; Hao, Q.; Ma, Y.; Lan, Y. C.; Minnich, A.; Yu, B.; Yan, X. A.; Wang, D. Z.; Muto, A.; Vashaee, D.; Chen, X. Y.; Liu, J. M.; Dresselhaus, M. S.; Chen, G.; Ren, Z. F. *Science* **2008**, *320*, 634.

[28] Ma, Y.; Hao, Q.; Poudel, B.; Lan, Y. C.; Yu, B.; Wang, D. Z.; Chen, G.; Ren, Z. F. *Nano Lett.* **2008**, *8*, 2580.

[29] Joshi, G.; Lee, H.; Lan, Y. C.; Wang, X. W.; Zhu, G. H.; Wang, D. Z.; Gould, R. W.; Cuff, D. C.; Tang, M. Y.; Dresselhaus, M. S.; Chen, G.; Ren, Z. F. *Nano Lett.* **2008**, *8*, 4670.

CHAPTER 4 Ambient Facile Synthesis of Gram-Scale Copper Selenide Nanostructures from Commercial Copper and Selenium Powder

Based on the previous chapter, searching for facile and high yield fabrication method of copper selenide is an issue for thermoelectric application. Grams of $Cu_{2-x}Se$ nanostructures were prepared from commercial copper and selenium powders in the presence of thiol ligands by a one-pot reaction at room temperature. The morphology of the nanostructures is strongly dependent on the ratio of thiol ligand to selenium powder. The resultant $Cu_{2-x}Se$ ($0 \leq x \leq 0.25$) nanostructures were treated with hydrazine solution to remove the surface ligands and then explored as a potential thermoelectric candidate in comparison with commercial copper selenide powders. The results demonstrate that the synthetic samples from our novel approach exhibit similar thermoelectric properties to commercial Cu_2Se.

4.1 Introduction

Copper selenides have been explored as thermoelectric materials and have shown enhanced performance.[1-2] For example, non-doped β-phase Cu_2Se and $Cu_{2-x}Se$ fabricated by high-temperature solid state reaction have a figure of merit, *ZT*, of around 1.5 at 1000 K,[3] which is the highest value among the bulk materials. This value was notably enhanced to 1.7−1.8 at 700 ˚C by the introduction of nanoscale precipitates through fast

quenching of their liquids in the latest report.[4] The higher *ZT* of *β*-phase Cu_2Se and $Cu_{2-x}Se$ is attributed to the extraordinary liquid-like behavior of the copper ions around a crystalline sublattice of Se.[3] Although various strategies, such as hydrothermal or solvothermal approaches,[5-7] sonochemistry,[8-9] electrochemical-deposition,[10-12] the microwave-assisted route,[13] and the cation exchange method,[14] have been developed to prepare nanoscale copper selenides, most methods are not able to produce large-scale samples for thermoelectric research. An alternative approach is the high-energy ball-milling method,[2] which is energy-consuming and time-consuming. Thus, a facile synthesis of copper selenide on a large scale is desirable.

In this work, large amounts of $Cu_{2-x}Se$ nanostructures were synthesized through the ambient reaction of commercial copper powders with selenium powders in the presence of 2-mercaptoethanol and traces of NaOH. The as-prepared samples were treated with hydrazine solution to remove the adsorbed surface ligands. The resultant pristine $Cu_{2-x}Se$ nanoparticles were sintered into pellets for investigation of their thermoelectric properties in comparison with commercial Cu_2Se powder, which was sintered and measured under the same conditions. The obtained *ZT* is comparable to that of the commercial samples and reaches 0.28 at 480 ˚C.

4.2 Experimental section

4.2.1 Synthesis of $Cu_{2-x}Se$ nanostructures

Cu powder (0.06 mol), 12.6 mL 2-mercaptoethanol (0.18 mol), 1 mL NaOH (7 M), and 100 mL anhydrous ethanol were loaded into a 250 mL glass flask. The mixture was stirred for 5 min, and Se powder (0.03 mol) was added into the mixture. The color of the mixture gradually turned to black, suggesting the reaction of reddish copper with gray selenium powder. After the mixture was reacted for 24 h under gentle stirring, black precipitates were separated by centrifuge. These precipitates were dispersed in 20 mL hydrazine solution and stirred overnight. The precipitates were separated, washed with distilled water and ethanol several times, and then dried in vacuum at room temperature.

4.2.2 Effects of chalcogen/2-mercaptoethanol ratio on $Cu_{2-x}Se$ nanostructures

In order to investigate the influence of 2-mercaptoethanol on nanostructures, a group of experiments been performed by using different amount of 2-mercaptoethanol. The ratio of Se to 2-mercaptoethanol was varied from 1/3 through 1/5, 1/7, 1/10, 1/20, and 1/30 to 1/50. The resultant samples were purified using the same process as described above.

4.2.3 Morphology evolution of $Cu_{2-x}Se$ nanostructures

The evolution of nanostructures was investigated by analyzing samples collected after different reaction times. The group experiments used a ratio of Se/2-mercaptoethanol of 1/50, and intermediate samples were collected at 5 min, 1 h, 2 h, 8 h, and 24 h. All the

samples were purified using the above procedure.

4.3 Results and discussion

4.3.1 Results of synthesized $Cu_{2-x}Se$ nanostructures

Copper selenide was fabricated from commercial copper powders and selenium powders in the presence of 2-mercaptoethanol at room temperature, and the resultant nanostructures were treated with hydrazine solution to remove surface organic material, which can influence the thermoelectric properties of pellets sintered from nanopowders due to the evaporation of organics during sintering and measurement at high temperature. Figure 4.1 shows FESEM and TEM images of the non-treated sample. A mixture of nanoparticles and nanosheets was observed [Figure 4.1(a-c)], in which the nanosheets are assembled from small nanoparticles and have a thickness of around 7 nm. The SAED pattern in the inset of Figure 4.1(c) also indicates this characteristic, which is consistent with the random orientation of the crystal lattice, as shown by the HRTEM image of the selected area [Figure 4.1(d)]. The sheet structure was destroyed by treatment with hydrazine solution, but nanoparticles remained assembled together (Figure 4.2). The HRTEM images of both non-treated and treated samples clearly display lattice fringes with a spacing of 0.33 nm, matching well with the (111) planes of cubic $Cu_{2-x}Se$ [Figure 4.1(d), 4.2(c)]. These results suggest that removal of surface organic ligands by hydrazine did not influence the crystal structure.

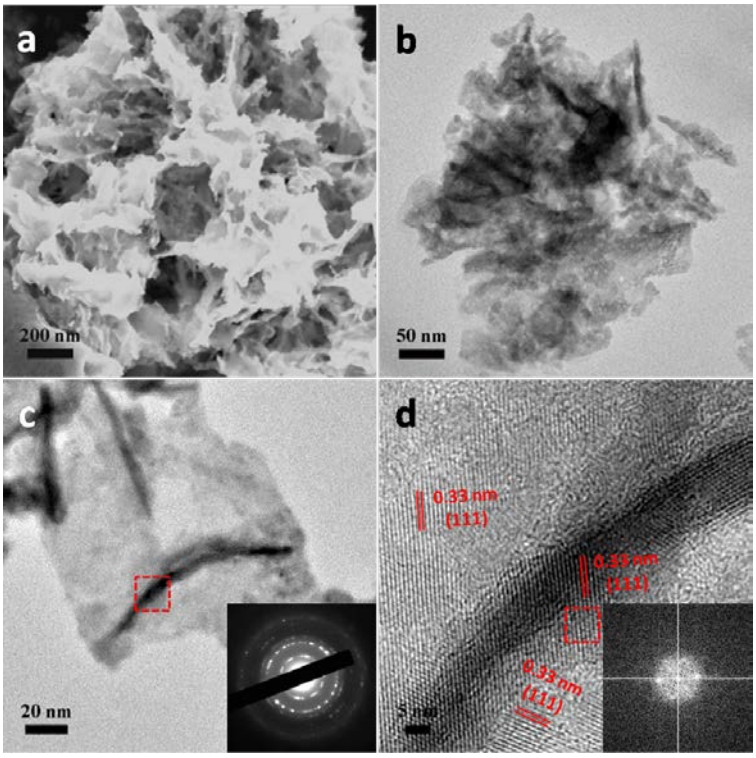

Figure 4.1 (a-c) FESEM and TEM images of as-prepared $Cu_{2-x}Se$ nanostructures. The inset in (c) is the SAED pattern of a typical single layer of $Cu_{2-x}Se$. (d) HRTEM image of the selected area in (c), with the inset of FFT pattern from the area selected with the dashed square in (d).

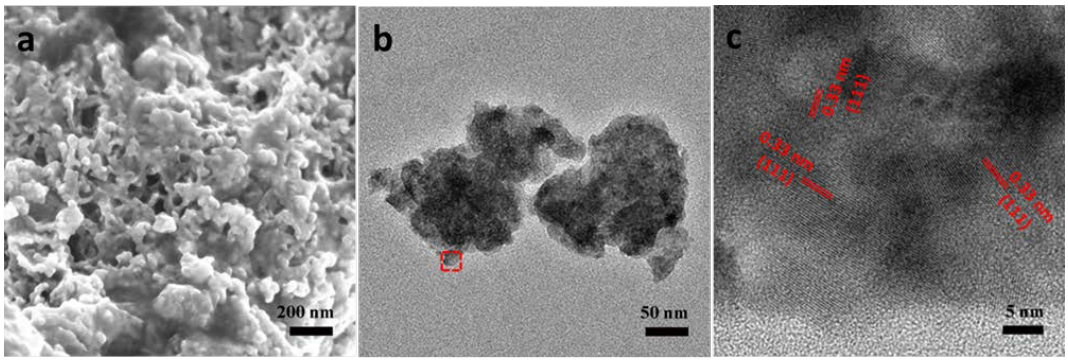

Figure 4.2 (a) FESEM image and (b) TEM image of the $Cu_{2-x}Se$ powder treated with N_2H_4. (c) HRTEM image of a small region of the selected area in (b).

To confirm their crystal structures, XRD patterns of treated and non-treated samples were collected [Figure 4.3(a)]. All the peaks of both samples match well with standard peaks of fcc Cu_2Se (JCPDS 88-2043), demonstrating that no crystal structure or phase change occurred after treatment with hydrazine, although the morphology was drastically modified after treatment. The strong and sharp diffraction peaks suggest that both samples are well-crystallized, despite using room-temperature synthesis and modification. To demonstrate the successful removal of surface organic material, TGA was used to compare the weight loss of samples before and after hydrazine treatment [Figure 4.3(b)]. The weight loss was reduced from 13 % to only 3 % after hydrazine treatment, which means that most of the surface ligands were removed.

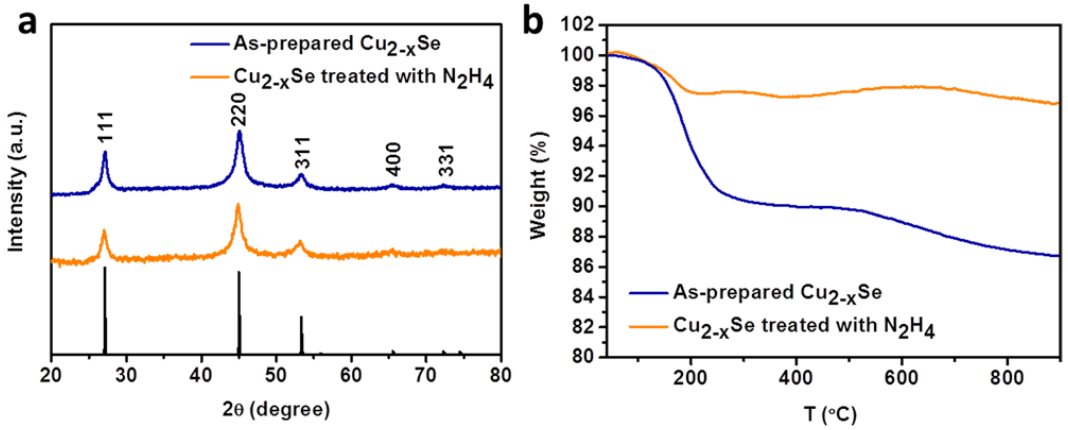

Figure 4.3 (a) XRD patterns and (b) TGA curves of as-prepared $Cu_{2-x}Se$ nanostructures before and after treatment with N_2H_4. The vertical lines in (a) mark the line positions of the Cu_2Se standard (JCPDS 88-2043)

The scanning TEM image and the corresponding EDX elemental mapping images of

nanostructures are shown in Figure 4.4, further revealing the homogenous distribution of Cu and Se elements in whole the structure. The average Cu/Se ratios in non-treated and treated samples were determined to be 1.91 and 1.95 by ICP-AES.

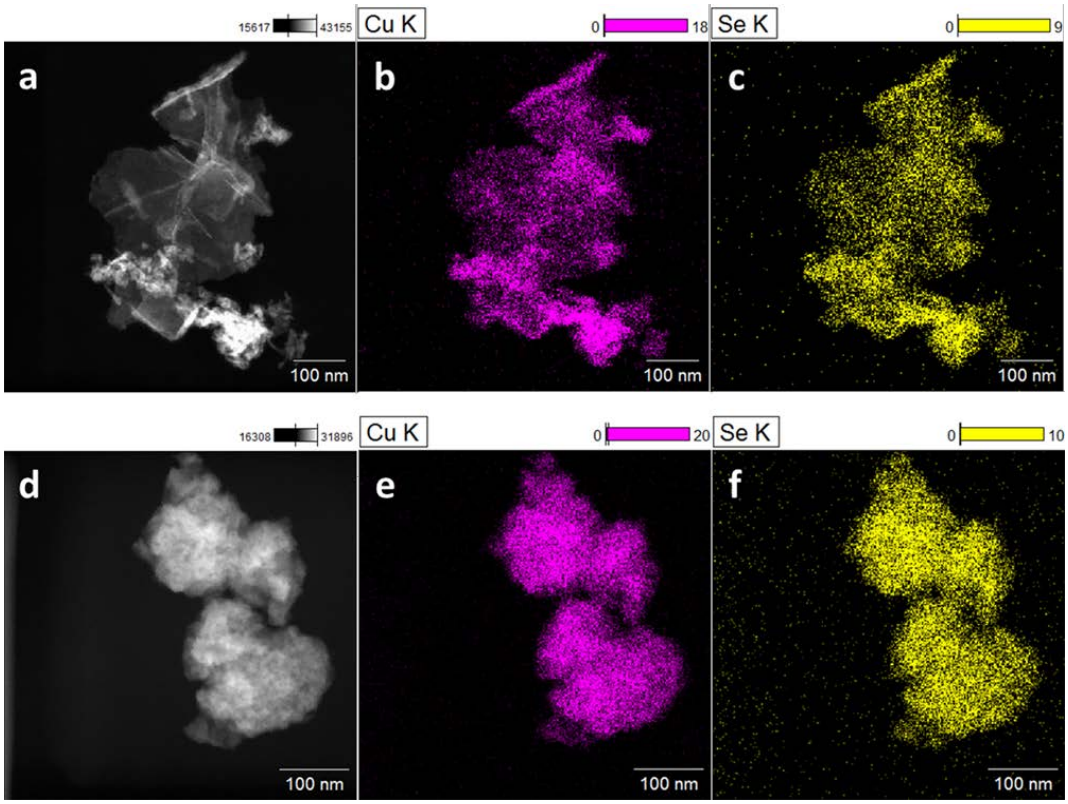

Figure 4.4 (a) Scanning TEM image of as-prepared $Cu_{2-x}Se$ nanostructures; (b-c) EDX elemental mapping of Cu and Se for the selected area in a. (d) Scanning TEM image of $Cu_{2-x}Se$ nanostructures after treatment with N_2H_4; (e-f) EDX elemental mapping of Cu and Se for the selected area in d.

Raman spectroscopy was further applied to demonstrate the removal of surface ligands. The spectra of both the non-treated and the treated $Cu_{2-x}Se$ samples clearly show the

characteristic vibration of the Cu-Se bond at 256 cm^{-1} (Figure 4.5).[15-17] The spectra also confirm the absence of the typical peak of the –SH group at 2500-2600 cm^{-1}.[18] It is well known that $Cu_{2-x}Se$ is easy to oxidize,[19-20] and XPS was used to determine the ratio of different valence states of Cu (i.e., Cu^{+}/Cu^{2+}) in both non-treated and treated $Cu_{2-x}Se$ samples (Figure 4.6). The XPS spectra of Cu 2p confirm the presence of both Cu^{+} and Cu^{2+} in both samples [Figure 4.6(a, c)]. The ratio of Cu^{+}/Cu^{2+} increases from 6.8 to 8.3 after the treatment with hydrazine due to the reduction capability of hydrazine.[21] The spectra of Se 3d in both samples suggest the existence of Se^{2-} at 53.8 eV [Figure 4.6(b, d)]. A small peak at 58.2 eV in the original sample is attributed to the adsorbed organic selenide on its surface [Figure 4.6(b)],[20,22] which was successfully removed after treatment [Figure 4.6(d)].

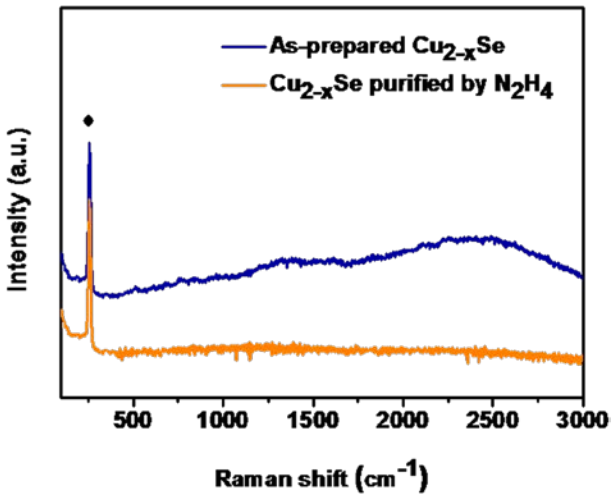

Figure 4.5 Raman spectra of the $Cu_{2-x}Se$ nanostructures before and after treatment with N_2H_4.

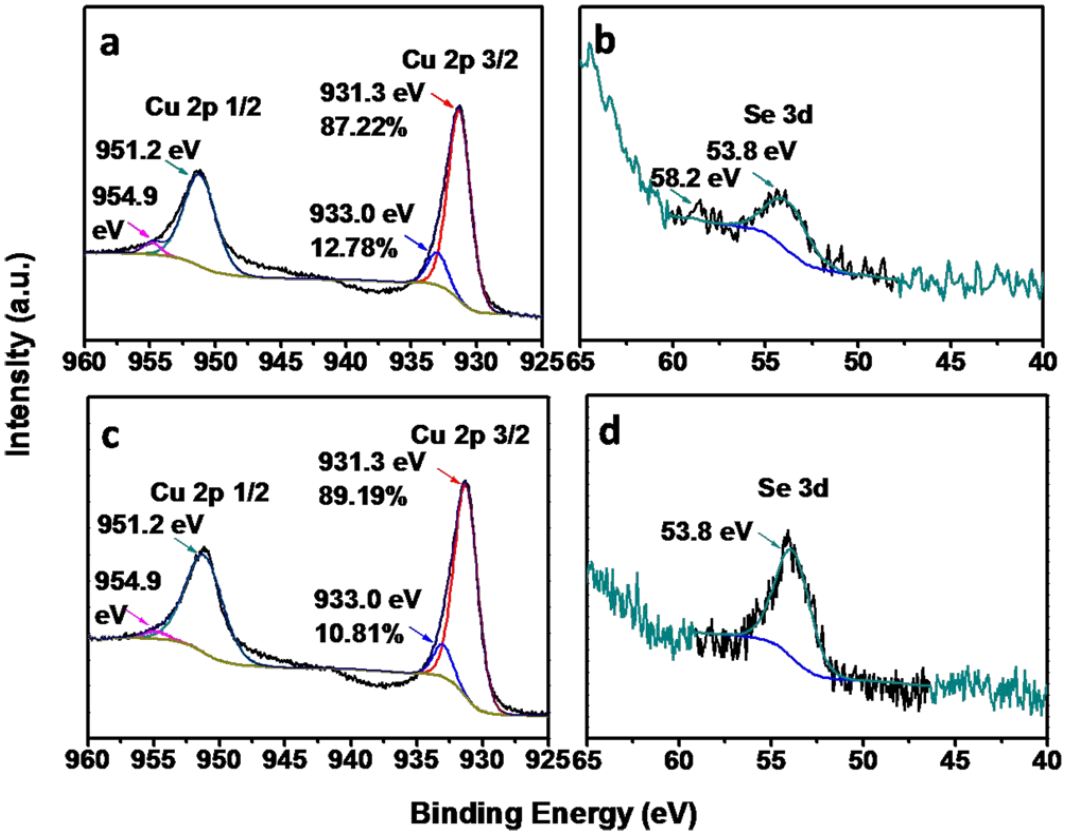

Figure 4.6 XPS spectra of (a) Cu 2p and (b) Se 3d of as-prepared $Cu_{2-x}Se$; (c) Cu 2p and (d) Se 3d of $Cu_{2-x}Se$ powder treated with N_2H_4.

4.3.2 Effects of chalcogen/2-mercaptoethanol ratio on $Cu_{2-x}Se$ nanostructures

A previous report on the preparation of highly crystalline CuSe from copper and selenium in pure 2-mercaptoethanol[23] demonstrates that the key role of 2-mercaptoethanol is to dissolve selenium to form highly reactive selenothiolate.[24-26] Theoretical calculations show that the reaction between copper and $HOCH_2CH_2SSe^-$ is spontaneous. The influence of 2-mercaptoethanol on the $Cu_{2-x}Se$ nanostructures was investigated (Figure 4.7). The ratio of Cu and 2-mercaptoethanol was varied from 1/3,

through 1/5, 1/7, 1/10, 1/20, and 1/30, to 1/50. The resultant nanostructures are a mixture of nanoparticles and nanosheets. The thickness of the nanosheets increases with increasing concentration of 2-mercaptoethanol (Figure 4.7). The average thickness of the nanosheets obtained from the ratio of 1/3 is 7 nm (Figure 4.1), and it increases through 11 nm, 15 nm, 18 nm, 23 nm, and 29 nm, to 47 nm with the ratio of Cu/2-mercaptoethanol increasing from 1/3, through 1/5, 1/7, 1/10, 1/20, and 1/30, to 1/50, respectively. These results demonstrate that more 2-mercaptoethanol promotes the growth of nanosheets along the (111) surface, which is the automatically smooth surface with the lowest energy in the fcc structure.[27]

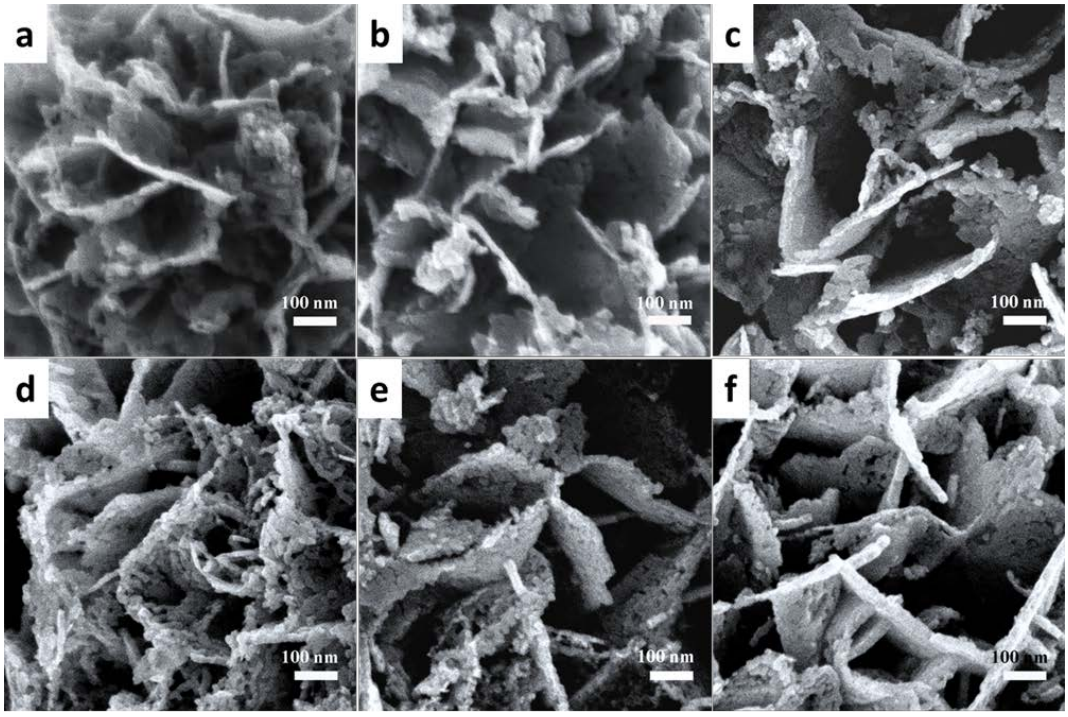

Figure 4.7 SEM images of $Cu_{2-x}Se$ nanostructures prepared from different molar ratios of Cu to 2-mercaptoethanol: (a) 1/5, (b) 1/7, (c) 1/10, (d) 1/20, (e) 1/30, (f) 1/50.

The XRD patterns of all the products (Figure 4.8) are matched well with fcc Cu_2Se (JCPDS 88-2043), which means that the use of more 2-mercaptoethanol did not influence the crystal structure of $Cu_{2-x}Se$.

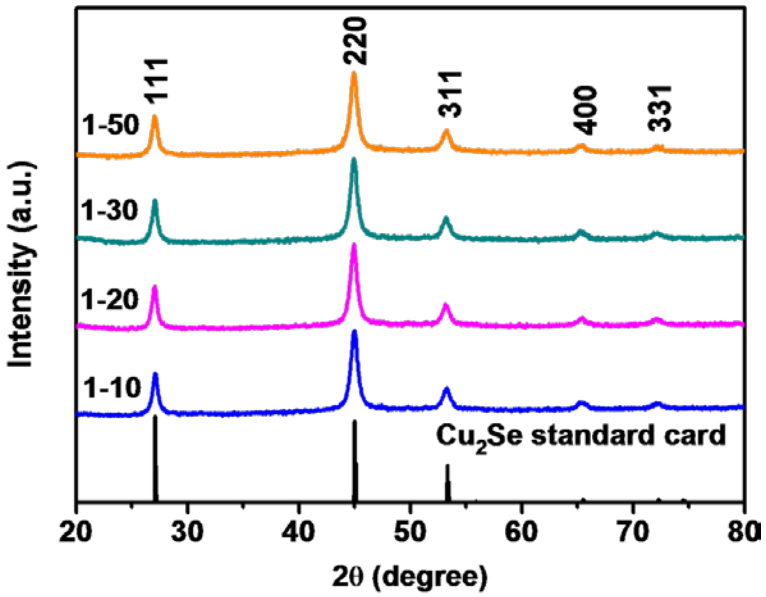

Figure 4.8 XRD patterns of the $Cu_{2-x}Se$ nanostructures prepared by using different molar ratios of Cu to 2-mercaptoethanol. The vertical lines indicate the peak positions of standard Cu_2Se (JCPDS 88-2043).

4.3.3 Morphology evolution of $Cu_{2-x}Se$ nanostructures

The evolution of the nanostructures was investigated in the case of the Cu/2-mercaptoethanol ratio of 1/50. The original commercial Cu powder is irregular and rough [Figure 4.9(a)]. 5 min after the addition of selenium powder into the reaction solution, small nanoparticles were formed and assembled into thin nanosheets [Figure

4.9(b)]. Increasing the reaction time led to the growth of small nanoparticles and the growth of nanosheets [Figure 4.9(c-f)].

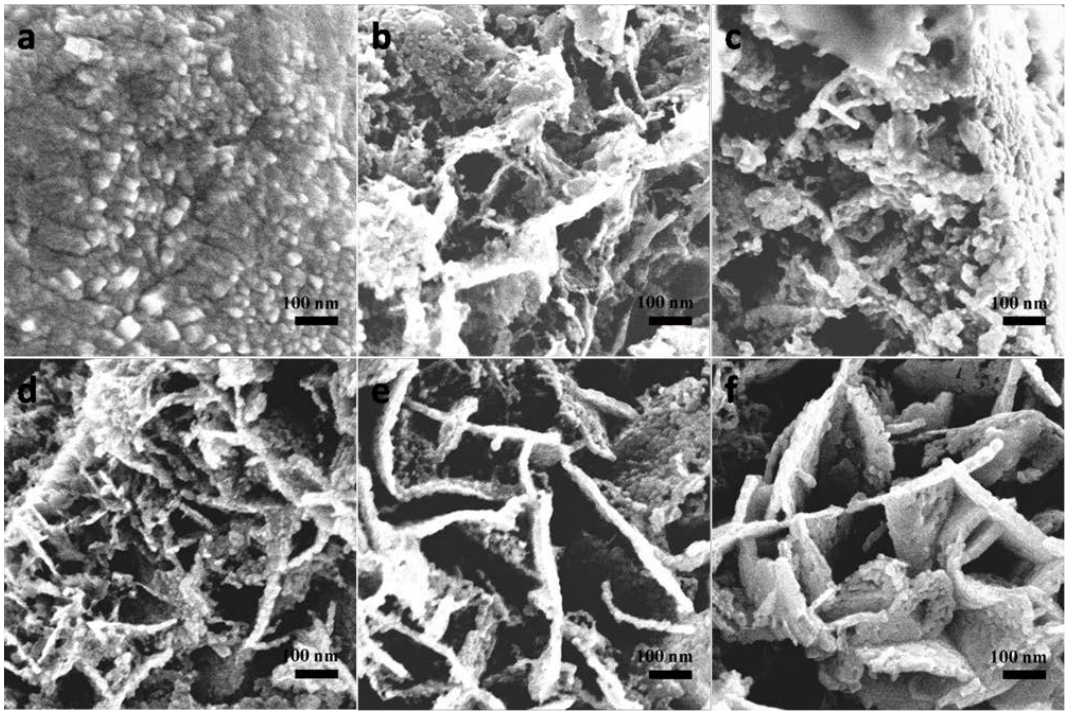

Figure 4.9 FESEM images of the Cu powders (a) and $Cu_{2-x}Se$ nanostructures with a ratio of Cu/2-mercaptoethanol of 1/50 after different reaction times: (b) 5 min; (c) 1 h; (d) 2 h; (e) 8 h; (f) 24 h.

The XRD patterns of all the samples also confirm the evolution of the nanostructures and the transformation of Cu into $Cu_{2-x}Se$ (Figure 4.10). The product obtained within a short reaction time (i.e., 5 min) is a mixture of Cu and $Cu_{2-x}Se$, as indicated by the high intensity of the Cu peaks and the very weak peaks from $Cu_{2-x}Se$ in its XRD pattern. Extended reaction time led to more $Cu_{2-x}Se$ being formed and an increase in the intensity

of the $Cu_{2-x}Se$ peaks in the corresponding XRD patterns. The pure $Cu_{2-x}Se$ obtained after 24 h reaction demonstrates the complete transformation of Cu into $Cu_{2-x}Se$.

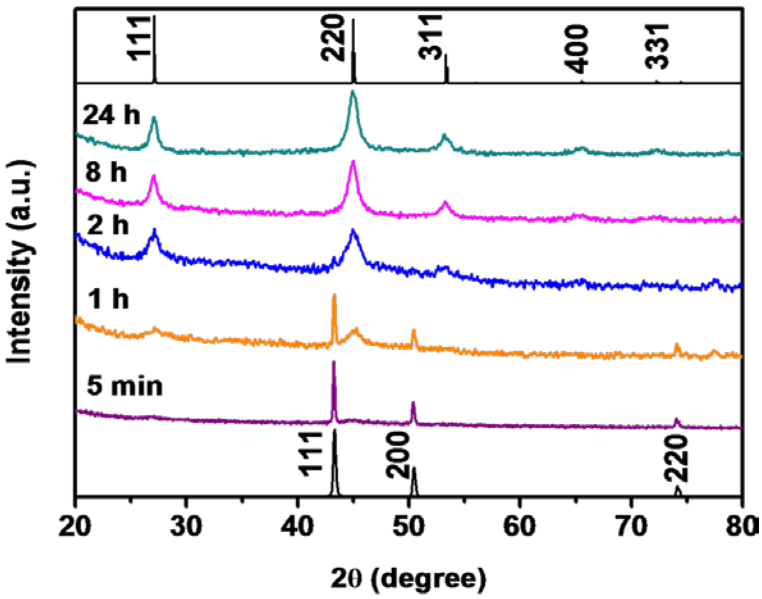

Figure 4.10 XRD patterns of the $Cu_{2-x}Se$ samples with a ratio of Cu/2-mercaptoethanol of 1/50 after different reaction times.

4.3.4 Thermoelectric performance

An advantage of my method is that it is capable of producing grams of $Cu_{2-x}Se$ nanostructures in a one-pot reaction for investigation of their properties and applications. As mentioned previously, copper selenides such as $Cu_{2-x}Se$ and Cu_2Se could be the candidate of thermoelectric materials. The thermoelectric properties of the as-synthesized $Cu_{2-x}Se$ nanostructures were investigated in comparison with commercial Cu_2Se powder. Both synthetic and commercial powders were sintered by SPS, and the resultant pellets were cut into pieces of a similar size and then measured under the same conditions.[28] As

shown in Figure 4.11(a), the electrical conductivity of the synthetic $Cu_{2-x}Se$ sample is higher than that of the commercial Cu_2Se powder from room temperature to 480 ˚C. Due to its excellent electrical conductivity, the Seebeck coefficient of $Cu_{2-x}Se$ is lower than that of the commercial sample (i.e., 35 μV/K at room temperature and 80 μV/K at 480˚C) [Figure 4.11(b)]. Following the same trend as with the Seebeck coefficient, this sample has a power factor (PF) of 0.3 $\mu W \cdot cm^{-1}K^{-2}$ at room temperature and 3.5 $\mu W \cdot cm^{-1}K^{-2}$ at 480 ˚C, lower than the corresponding values for the commercial sample [Figure 4.11(c)]. Heat capacities (C_p) were measured and are shown in Figure 4.11(d). A sharp endothermal peak at around 140 ˚C was observed in both the $Cu_{2-x}Se$ and the commercial samples.[2] The overall thermal conductivity of the $Cu_{2-x}Se$ and commercial samples calculated from Equation (2.3) demonstrates that our $Cu_{2-x}Se$ sample has lower thermal conductivity than that of the commercial Cu_2Se sample [Figure 4.11(e)]. The figures of merit *ZT* for our $Cu_{2-x}Se$ and the commercial sample were calculated from Equation (1.1).

The calculated *ZT* values of the $Cu_{2-x}Se$ and Cu_2Se samples are plotted in Figure 4.11(f), where a slight decrease in *ZT* at 140 ˚C can be observed due to the presence of a sharp endothermal peak at this temperature [Figure 4.11(d)]. The *ZT* values of $Cu_{2-x}Se$ and the commercial sample increase with increasing temperature, and reach 0.28 and 0.38 at 480 ˚C, respectively. These results are also similar to that for $Cu_{2-x}Se$ prepared from a high-temperature solid state reaction.[29]

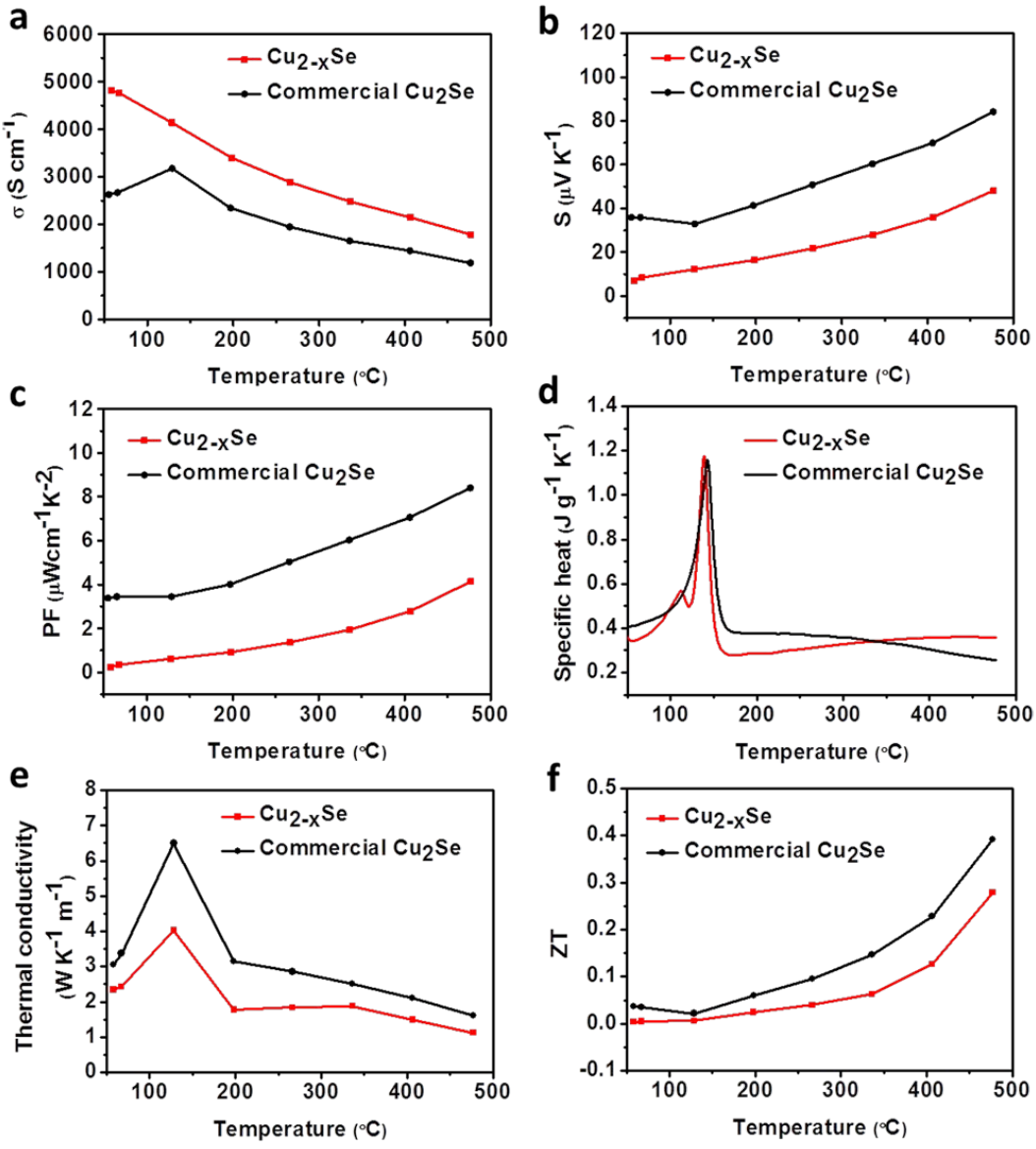

Figure 4.11 Temperature dependence of the thermoelectric properties of synthetic $Cu_{2-x}Se$ and commercial Cu_2Se samples: (a) electrical conductivity; (b) Seebeck coefficient; (c) power factor; (d) specific heat capacity (C_p); (e) thermal conductivity; (f) figure-of merit calculated using Equation (1.4).

4.3.5 Stability of $Cu_{2-x}Se$ in thermoelectric performance

The higher electrical conductivity and lower overall thermal conductivity of my $Cu_{2-x}Se$ sample could be attributed to its stable crystal structure, which was re-examined after SPS sintering and thermoelectric measurements. The XRD patterns show that there was no phase transition in the $Cu_{2-x}Se$ sample after sintering and measurement at high temperature, except that the peaks became narrower and sharper due to the improvement in crystallization at high temperature [Figure 4.12(a)]. The original as-received commercial Cu_2Se powder consists of cubic and orthorhombic phases, however, the fraction of orthorhombic Cu_2Se became pronounced after it was sintered into a pellet under the same conditions, and it was completely transformed into the orthorhombic structure after high-temperature measurements [Figure 4.12(b)]. The disordered Cu ions in the cubic structure at high temperature would be highly efficient phonon scattering centres as compared with the orthorhombic structure, which increases the carrier concentration.[2-3] The average Cu/Se ratios in pellets of our $Cu_{2-x}Se$ and the commercial samples after SPS and measurement were determined to be 1.93 and 2.02, respectively, by ICP-AES, which shows a higher Cu deficiency in the $Cu_{2-x}Se$ sample. Increased carrier concentration enhances the electrical conductivity according to Equations (4.1-4.2), however, the Seebeck coefficient of the $Cu_{2-x}Se$ compounds was found to decrease with increasing carrier concentration.[29]

$$\rho = 1/\mu ne \tag{4.1}$$

$$\alpha = \frac{k}{e}\left(r - ln\frac{n}{N_0} \right) \tag{4.2}$$

where ρ, μ, n, e, α, k, r, and N_0 are the electrical resistivity, carrier mobility, carrier concentration, charge of the electron, Seebeck coefficient, Boltzmann's constant, scattering factor, and Avogadro constant, respectively.[30-31] In addition to the liquid-like behaviour of copper ions at high temperature, the lower thermal conductivity of prepared $Cu_{2-x}Se$ sample could be also due to the presence of nanoscale grains, pores, and boundaries in the pellet, which can effectively improve the phonon scattering and decrease the thermal conductivity. SEM images of pellets made from $Cu_{2-x}Se$ nanoparticles and commercial Cu_2Se powder in Figure 4.12(c-d) clearly show that the $Cu_{2-x}Se$ pellet has a larger amount of nanoscale particles and pores than the Cu_2Se pellet, although they were sintered under the same conditions (i.e., 430 ˚C, 65 MPa, and 10 min) by SPS technology. In addition, the pronounced copper-deficiency in the $Cu_{2-x}Se$ sample leads to more vacancies, which are also responsible for its lower thermal conductivity.

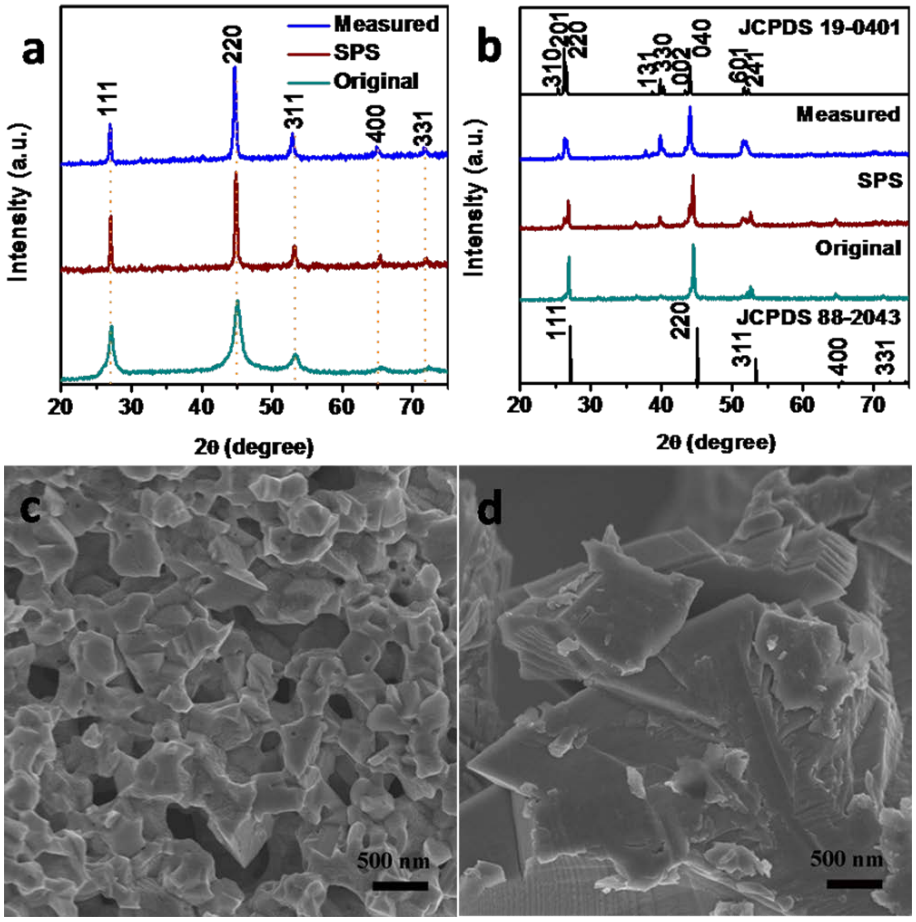

Figure 4.12 XRD patterns of (a) as-prepared $Cu_{2-x}Se$ nanopowder (Original), $Cu_{2-x}Se$ pellet after sintering at 430 ˚C under 65 MPa (SPS), and $Cu_{2-x}Se$ pellet after thermoelectric measurements (Measured); (b) commercial Cu_2Se powder, Cu_2Se pellet sintered under the same conditions as in (a), and Cu_2Se pellet after thermoelectric measurements. FESEM images of cross-sections of (c) $Cu_{2-x}Se$ and (d) Cu_2Se pellets after sintering at 430 ˚C under 65 MPa by the spark plasma sintering technique and thermoelectric measurements.

4.4 Conclusions

In this chapter, grams of $Cu_{2-x}Se$ nanostructures have been synthesized by a one-pot reaction of commercial copper powder with Se powder in the presence of 2-mercaptoethanol. The resultant nanostructures were treated with hydrazine solution to remove adsorbed surface ligands. The hydrazine treatment destroyed the sheet-like structure and resulted in pristine $Cu_{2-x}Se$ nanoparticles, which were sintered into a pellet. Their thermoelectric properties were measured in comparison with commercial Cu_2Se powder under the same conditions. Their thermoelectric properties show that the $Cu_{2-x}Se$ sample has a similar temperature-dependent *ZT* (0.28 at 480 ˚C) to that of the commercial sample. The $Cu_{2-x}Se$ sample retained the same crystal structure and morphology after SPS sintering and thermoelectric measurements at high temperature. This research provides a simple way to prepare large-scale copper selenide nanostructures for diverse applications.

References

[1] Han, C.; Li, Z.; Dou, S. X. *Chin. Sci. Bull.* **2014**, *59*, 2073.

[2] Yu, B.; Liu, W. S.; Chen, S.; Wang, H.; Wang, H. Z.; Chen, G.; Ren, Z. F. *Nano Energy* **2012**, *1*, 472.

[3] Liu, H. L.; Shi, X.; Xu, F. F.; Zhang, L. L.; Zhang, W. Q.; Chen, L. D.; Li, Q.; Uher, C.; Day, T.; Snyder, G. J. *Nat. Mater.* **2012**, *11*, 422.

[4] Zhao, L. L.; Wang, X. L.; Wang, J. Y.; Cheng, Z. X.; Dou, S. X.; Wang, J. L.; Liu, L. Q. *Scientific Reports* **2015**, *54*, 7671.

[5] Zhang, Y.; Hu, C. G.; Zheng, C. H.; Xi, Y.; Wan, B. Y. *J. Phys. Chem. C* **2010**, *114*, 14849.

[6] Li, D. P.; Zheng, Z.; Lei, Y.; Ge, S. X.; Zhang, Y. D.; Zhang, Y. G.; Wong, K. W.; Yang, F. L.; Lau, W. M. *CrystEngComm* **2010**, *12*, 1856.

[7] Deka, S.; Genovese, A.; Zhang, Y.; Miszta, K.; Bertoni, G.; Krahne, R.; Giannini, C.; Manna, L. *J. Am. Chem. Soc.* **2010**, *132*, 8912.

[8] Xie, Y.; Zheng, X. W.; Jiang, X. C.; Lu, J.; Zhu, L. Y. *Inorg. Chem.* **2002**, *41*, 387.

[9] Xu, S.; Wang, H.; Zhu, J. J.; Chen, H. Y. *J. Cryst. Growth* **2002**, *234*, 263.

[10] Thouin, L.; Rouquette-sanchez, S.; Vedel, J. *Electrochim. Acta* **1993**, *38*, 2387.

[11] Massaccesi, S.; Sanchez, S.; Vedel, J. *J. Electrochem. Soc.* **1993**, *140*, 2540.

[12] Yu, R.; Ren, T.; Sun, K. J.; Feng, Z. C.; Li, G. N.; Li, C. *J. Phys. Chem. C* **2009**, *113*, 10833.

[13] Cao, X. B.; Zhao, C.; Lan, X. M.; Gao, G. J.; Qian, W. H.; Guo, Y. *J. Phys. Chem. C* **2007**, *111*, 6658.

[14] Li, H. B.; Zanella, M.; Genovese, A.; Povia, M.; Falqui, A.; Giannini, C.; Manna, L. *Nano Lett.* **2011**, *11*, 4964.

[15] Cho, A.; Ahn, S.; Yun, J. H.; Gwak, J.; Ahn, S. K.; Shin, K.; Yoo, J.; Song, H.; Yoon, K. *Thin Solid Films* **2013**, *546*, 299.

[16] Witte, W.; Kniese, R.; Powalla, M. *Thin Solid Films* **2008**, *517*, 867.

[17] Izquierdo-Roca, V.; Saucedo, E.; Ruiz, C. M.; Fontane, X.; Calvo-Barrio, L.; Alvarez-Garcia, J.; Grand, P. P.; Jaime-Ferrer, J. S.; Perez-Rodriguez, A.; Morante, J. R.; Bermudez, V. *Phys. Status Solidi A* **2009**, *206*, 1001.

[18] Szafranski, C. A.; Tanner, W.; Laibinis, P. E.; Garrell, R. L. *Langmuir* **1998**, *14*, 3570.

[19] Miszta, K.; Brescia, R.; Prato, M.; Bertoni, G.; Marras, S.; Xie, Y.; Ghosh, S.; Kim, M. R.; Manna, L. *J. Am. Chem. Soc.* **2014**, *136*, 9061.

[20] Riha, S. C.; Johnson, D. C.; Prieto, A. L. *J. Am. Chem. Soc.* **2011**, *133*, 1383.

[21] Chang, Y.; Lye, M. L.; Zeng, H. C. *Langmuir* **2005**, *21*, 3746.

[22] Fonder, G.; Volcke, C.; Csoka, B.; Delhalle, J.; Mekhalif, Z. *Electrochim. Acta* **2010**, *55*, 1557.

[23] Kumar, P.; Gusain, M.; Nagarajan, R. *Inorg. Chem.* **2012**, *51*, 7945.

[24] Amaratunga, W.; Milne, J. *Can. J. Chem.* **1994**, *72*, 2506.

[25] Afsar, H.; Tor, I.; Apak, R. *Analyst* **1989**, *114*, 1315.

[26] Afsar, H.; Apak, R.; Tor, I. *Analyst* **1989**, *114*, 1319.

[27] Tan, M.; Chen, X. Q. *J. Electrochem. Soc.* **2012**, *159*, K15.

[28] Chen, X. Q.; Li, Z.; Yang, J. P.; Sun, Q.; Dou, S. X. *J. Colloid Interface Sci.* **2014**, *442*, 140.

[29] Xiao, X. X.; Xie, W. J.; Tang, X. F.; Zhang, Q. J. *Chin. Phys. B* **2011**, *20*, 087201.

[30] Ge, Z. H.; Zhang, B. P.; Yu, Z. X.; Li, J. F. *J. Mater. Res.* **2011**, *26*, 2711.

[31] Liu, W. S.; Zhang, B. P.; Li, J. F.; Zhang, H. L.; Zhao, L. D. *J. Appl. Phys.* **2007**, *102*.

CHAPTER 5 Room-Temperature Synthesis of $Cu_{2-x}E$ (E = S, Se) Nanotubes with Hierarchical Architecture as High-Performance Counter Electrodes of Quantum-Dot-Sensitized Solar Cells

Using the ambient facile synthesis method mentioned in chapter 3, $Cu_{2-x}E$ (E = S, Se) microtubes/NTs with a hierarchical architecture were prepared by using copper NWs, stable sulfur and selenium powder as precursors at room temperature. The theoretical calculation confirmed the reaction mechanism. The influence of reaction parameters (e.g., precursor ratio, ligands, ligand ratio, and reaction time) on the formation of NTs was comprehensively investigated. The resultant $Cu_{2-x}E$ (E = S, Se) NTs were used as CEs of QDSSCs to achieve a conversion efficiency (η) of 5.02 % and 6.25 %, respectively, much higher than that of QDSSCs made with Au CE (η = 2.94 %).

5.1 Introduction

Copper chalcogenide nanostructures have been exploited as CEs of QDSSCs with enhanced electrochemical performance owing to their super catalytic activity for the reduction of polysulfide.[1-6] Currently, the conventional noble counter electrodes (Pt or Au) are unsuitable for QDSSC applications when polysulfide electrolytes are used, mainly because sulfur-containing (S^{2-} or thiol) compounds are absorbed preferentially and strongly on the Pt or Au surface, leading to surface passivation and decrease in the

conductivity of electrodes.[7-9] In contrast, copper chalcogenide based CEs show lower resistance and higher electrocatalytic activity towards the redox reaction of polysulfide, thus improving the conversion efficiency of QDSSCs.[3,8] For example, CuS and Cu_2S-based CEs boosted the conversion efficiency of CdS/CdSe QD sensitized solar cells to 4.1%, higher than that of QDSSCs made with Au CE.[4] The better performance and lower cost of copper chalcogenides make them promising alternative CE to the noble metal Pt and Au analogues. Current investigations in this field, however, are mainly focused on 0D copper sulfides and selenide ($Cu_{2-x}E$, E = S, Se, $0 \leq x \leq 1$) nanostructures, and there are few reports on their 1D counterparts.[5-6]

Among different type of copper chalcogenide nanostructures,[10-20] 1D microtubes and NTs have increasingly attracted considerable attention because of their superior performance, benefiting from both the hollow and 1D nature of their structures.[21] 1D hollow nanostructures not only show a higher speed of electron transport, but also exhibit larger surface area in comparison with solid analogues. They can be formed by the self-sacrifice of templates through the Kirkendall effect.[22] Most syntheses rely on high temperature or complicated processes, however.[23-24] There are few reports on the synthesis of $Cu_{2-x}E$ (E = S, Se) tubular nanostructures at room temperature.[25-28] For example, Cu_7S_4 and $Cu_{2-x}Se$ NT arrays on copper substrates can be formed by partially etching copper substrates into $Cu(OH)_2$ nanorods, followed by reaction with Na_2S and Na_2Se solution. From an application perspective, it would be highly desirable to develop

a versatile method to effectively synthesize size- tunable and surface-tunable copper chalcogenide colloidal NTs with a hierarchical architecture for diverse applications.

The importance of hierarchical nanostructures in boosting conversion efficiency of solar cells has been addressed in previous studies.[29-32] For example, hierarchical ZnO and TiO_2 NWs have been fabricated and utilized to realize higher conversion efficiency than NWs arrays in dye-sensitized solar cells (DSSCs). The higher conversion efficiency is due to 1D hierarchical nanostructure which significantly improved the electron diffusion length in photoelectrode films by providing a direct conduction pathway for the rapid collection of photogenerated electrons DSSCs.[30-32]

In this work, a versatile robust approach for the synthesis of $Cu_{2-x}E$ (E = S, Se) microtubes/NTs with a rough or flower-like surface from Cu NWs and chalcogen powder at room temperature was developed. The theoretical calculation confirmed the reaction mechanism. Cu NWs are conventionally used as building blocks of transparent electrodes.[33] Here they serve as self-sacrifice templates for $Cu_{2-x}E$ NTs. Interestingly, 2D nanosheets can be prepared from Cu NWs by simply increasing the amount of ligands (or using different ligands) during preparation. The resultant $Cu_{2-x}E$ (E = S, Se) NTs were employed as the CEs of QDSSCs to generate a conversion efficiency (η) of 5.02% and 6.25%, respectively, which are much higher than that of QDSSCs made with Au CE (η = 2.94%).

5.2 Experimental section

5.2.1 Computational Methods

The geometric structures of reactants, intermediates, and products were fully optimized using the generalized gradient approximation.[34-35] An all-electron double numerical atomic orbital basis set augmented by d-polarization functions (DNP) was used. This level of theory has been used to successfully determine the geometrical, energetic, and electronic structural properties of interactions of many small molecules and nanomaterials.[36-38] The optimized length of the Cu NW is 13.311 Å, and tetragonal supercell with a dimension of 30 × 30 × 13.311 ($Å^3$) was used for all the calculations. The Brillouin zone is sampled by 1 × 1 × 6 k-points using the Monkhorst-Pack scheme. The complete linear synchronous transit/quadratic synchronous transit (LST/QST) method[39] implemented in DMol3 code was used to find the transition states between the intermediate complexes and products. Implicit solvation was incorporated into all simulations by use of the conductor-like screening model – isosurface ball and stick (COSMO-ibs) polarisable continuum model, in which the dielectric continuum of permittivity (ε) of ethanol is 23.4.[40] All the calculations have been performed using the DMol3 module in Materials Studio.[41-42]

5.2.2 Solubility of Se or S powder in 2-mercaptoethanol

The role of 2-mercaptoethanol during the formation of NTs was addressed by examining the solubility of Se or S powder in the reaction mixture. 0.3 mmol Se powder

or S powder was added into different amounts of 2-mercaptoethanol in the same volume of NaOH (120 μL) and ethanol solution (10 mL) in six glass vials separately, i.e., the ratio of chalcogen precursor to 2-mercaptoethanol was varied from 3/1, through 2/1, 1/1, 1/3, and 1/5, to 1/10. The mixture was vigorously shaken for a few minutes, and then allowed to stand until all the undissolved powder precipitated at the bottom of the vials.

5.2.3 Synthesis of Cu NWs

Cu NWs were prepared by a slight modification from previous reports.[43-44] In a typical synthesis, 3.0 mL of $Cu(NO_3)_2$ (0.1 M) aqueous solution was added slowly to a glass bottle (volume capacity 125 mL) containing 90 mL of NaOH (7 M), followed by sequential injection of ethylenediamine (1.5 mL) and hydrazine solution (75 μL) under vigorous stirring. The bottle was sealed and immersed in a water bath (60 °C) for 1.5 h without stirring. The newly formed Cu NWs floated on the solution surface and were collected by centrifugation. The Cu NWs can be used directly without removing adsorbed NaOH for the preparation of $Cu_{2-x}S$ or $Cu_{2-x}Se$ NTs, or can be washed with water to remove the NaOH which was added during preparation.

5.2.4 Synthesis of $Cu_{2-x}Se$ and $Cu_{2-x}S$ NTs

Freshly prepared Cu NWs (0.3 mmol), 63 μL 2-mercaptoethanol (0.9 mmol), and 10 mL anhydrous ethanol were added into a 20 mL glass vial. After the mixture was stirred for 5 min, 0.02369 g Se or 0.0096 g S powder (0.3 mmol) was added to the mixture. The mixture gradually turned black, indicating the occurrence of the reaction. The black

suspension was gently stirred for 24 h and then was centrifuged to separate the $Cu_{2-x}Se$ or $Cu_{2-x}S$ precipitates. The black precipitates were washed with distilled water and ethanol several times and then dried under vacuum at room temperature.

5.2.5 Morphology evolution of $Cu_{2-x}Se$ NTs

The evolution of NTs was investigated by analyzing samples collected after different reaction times. Two groups of experiments were carried out. The first group experiments used a ratio of Se/2-mercaptoethanol of 1/3, and samples were collected at 5 min, 10 min, and 24 h. The second group experiments used a ratio of 1/50, and intermediate samples were collected at 1 min, 3 min, 5 min, 10 min, 20 min, and 8 h. All the samples were purified using the above procedure.

5.2.6 Reaction of Cu NWs with Se in different solutions

In order to investigate the role of 2-mercaptoethanol and NaOH, the as-prepared Cu NWs were thoroughly washed with distilled water, and the cleaned Cu NWs (0.4 mmol) were dispersed in 14 mL ethanol and then divided into four parts. Three parts were separately loaded into three small glass vials (3.5 mL each). The fourth part was centrifuged and washed twice in pure 2-mercaptoethanol, and then dispersed into 3.5 mL 2-mercaptoethanol in a glass vial. The four glass vials were labeled with 1, 2, 3, and 4, respectively. Vial 1was loaded with 21 μL 2-mercaptoethanol (0.3 mmol). Vial 2 was loaded with 21 μL 2-mercaptoethanol and 10 μL NaOH (7 M). Vial 3 and vial 4 had no 2-mercaptoethanol or NaOH. After that, 0.00790 g Se (0.1 mmol) was added to each vial,

and all mixtures were stirred for 24 h. All the samples were purified using the above procedure.

5.2.7 Effects of chalcogen/2-mercaptoethanol ratios on $Cu_{2-x}Se$ and $Cu_{2-x}S$ NTs

In order to investigate the influence of 2-mercaptoethanol on NTs, a group of experiments been performed by using a different amounts of 2-mercaptoethanol. The ratio of Se to 2-mercaptoethanol was varied from 1/3 through 1/10, 1/20, and 1/30 to 1/50. In the case of $Cu_{2-x}S$ NTs, the ratio of S to 2-mercaptoethanol was varied from 1/3 through 1/10 to 1/20. The resultant samples were purified using the same process as described above.

5.3 Results and discussion

5.3.1 Theoretical calculations

Previous investigations demonstrated that thiol molecules can covalently adsorb on the surface of copper substrates[45] and selenium can be dissolved in thiolate to form selenothiolate,[46-48] which suggests that copper could react with selenothiolate to form copper selenides. The reaction between copper and selenothiolate (or thiosulphide) was thus theoretically calculated using hydroxyethylthioselenide (or hydroxyethylthiosulphide) and Cu NWs as models through the DMol3 module in the Materials Studio software package. Cu NWs, $HOCH_2CH_2SSe^-$, $HOCH_2CH_2SS^-$, and their complexes were fully optimized using a generalized gradient approximation,[34] treated

with the Perdew- Burke-Ernzerhof exchange-correlation potential, and with long-range dispersion correction made using Grimme's scheme.[35] Figure 5.1 shows the reaction pathways of $HOCH_2CH_2SSe^-$ and $HOCH_2CH_2SS^-$ with Cu NWs, and the insets are fully optimized structures of Cu NWs, $HOCH_2CH_2SSe^-$, $HOCH_2CH_2SS^-$, and their complexes. The selenothiolate (or thiosulphide) ions can absorb on the surface of Cu NWs to form intermediate complexes, and their adsorption energies can be calculated from Equation (5.1).

$$E_{ads} = E_{nanowire-ligand} - \left(E_{nanowire} + E_{ligand} \right) \quad (5.1)$$

where $E_{nanowire\text{-}ligand}$ is the total energy of each complex, $E_{nanowire}$ is the energy of the isolated Cu NW, and E_{ligand} is the energy of selenothiolate (or thiosulphide). The calculated adsorption energies are -2.97 eV and -2.93 eV, respectively (Figure 5.1), which indicate the strong interactions between $HOCH_2CH_2SSe^-$ ($HOCH_2CH_2SS^-$) and Cu NWs. The intermediate complexes go through their transition states to form the products. In the reaction of $HOCH_2CH_2SSe^-$ with Cu NW, the energy difference between the intermediate complex and the transition state is negligible (0.05 eV), but the energy of the product is more negative than that of the intermediate complex (ΔE = -1.97 eV), which means that the reaction is a spontaneous process. In the reaction of $HOCH_2CH_2SS^-$ with Cu NW, the energy barrier between the intermediate complex and the transition state is 0.16 eV, which is higher than in the previous case. The slightly higher energy barrier suggests the slower reaction of $HOCH_2CH_2SS^-$ with Cu NW than that of $HOCH_2CH_2SSe^-$,

although the energy difference between the intermediate complex and the product in both cases is similar (i.e., -1.97 eV vs. -1.98 eV).

The calculation results indicate that the reactions between Cu, $HOCH_2CH_2SSe^-$, and $HOCH_2CH_2SS^-$ are spontaneous once the anionic precursors have formed. It is well known that the pK_a of the thiol (-SH) group in 2-mercaptoethanol is 9.61,[46] suggesting that 2-mercaptoethanol could be deprotonated to give hydroxyethylmercaptide by adding NaOH solution [Equation 5.2].[46-48] The hydroxyethylmercaptide formed is chalcophilic and could react with Se or S powder to form hydroxyethylthioselenide or hydroxyethylthiosulphide [Equations (5.3-5.4)]. Hydroxyethylthioselenide (or hydroxyethylthiosulphide) is highly reactive and could react with Cu to generate copper selenides or sulfides [Equations (5.5-5.6)].

$$HOCH_2CH_2SH + NaOH \longrightarrow HOCH_2CH_2SNa + H_2O \quad (5.2)$$

$$HOCH_2CH_2SNa + Se \longrightarrow HOCH_2CH_2SSeNa \quad (5.3)$$

$$HOCH_2CH_2SNa + S \longrightarrow HOCH_2CH_2SSNa \quad (5.4)$$

$$2Cu + HOCH_2CH_2SSeNa \longrightarrow Cu_2Se + HOCH_2CH_2SNa \quad (5.5)$$

$$2Cu + HOCH_2CH_2SSNa \longrightarrow Cu_2S + HOCH_2CH_2SNa \quad (5.6)$$

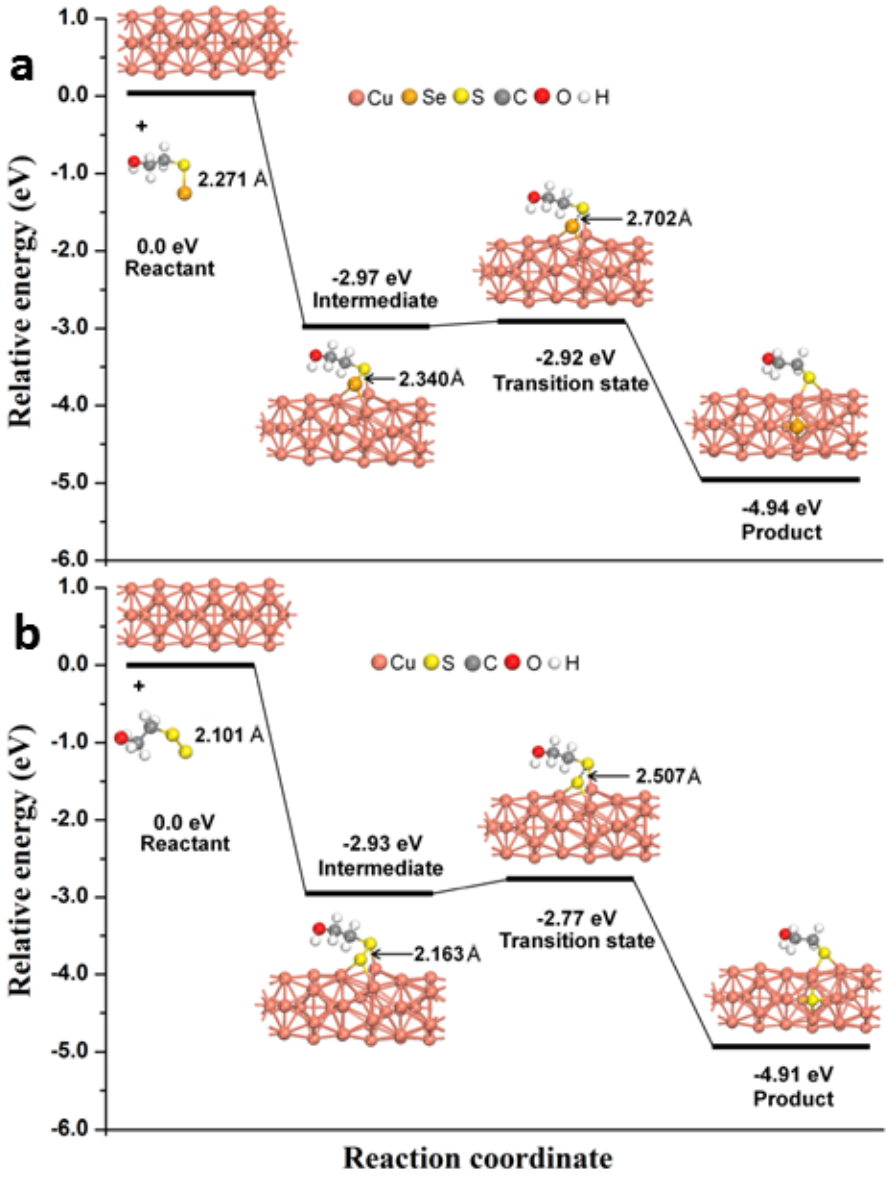

Figure 5.1 Energy profiles for reactions of $CH_2OHCH_2SSe^-$ (a) and $CH_2OHCH_2SS^-$ (b) with Cu NW.

5.3.2 Result of solubility of Se or S powder in 2-mercaptoethanol

In order to confirm our hypotheses, Se and S powder were added into the same volume of 2-mercaptoethanol and ethanol mixture in the absence and presence of NaOH,

respectively. It was found that Se or S powder was very difficult to dissolve in the mixture without NaOH. The addition of small amounts of NaOH, however, drastically promoted the dissolving of Se and S powder. Figure 5.2 presents optical photographs of mixed solutions containing the same amount of NaOH and different ratios of chalcogen powder and 2-mercaptoethanol (i.e., the molar ratios of chalcogen powder to 2-mercaptoethanol were varied from 3/1 through 2/1, 1/1, 1/3, and 1/5, to 1/10). The results clearly show that neither Se nor S powder was completely dissolved in the solutions with less 2-mercaptoethanol (i.e., chalcogen/2-mercaptoethanol ratios of 3/1 and 2/1). There are some Se and S powders remaining at the bottom of the glass vials. The addition of more 2-mercaptoethanol accelerated the dissolving of chalcogen powder to form a light solution. In the case of excessive 2-mercaptoethanol (i.e., 1/10 ratio), the obtained sulfur mixture solution is almost colorless. Therefore, the role of NaOH is to deprotonate 2-mercaptoethanol to form hydroxyethylmercaptide, which reacts with Se or S powder to produce selenothiolate (or thiosulphide). As shown in Figure 5.3, hydroxyethylmercaptide can also react with Cu NWs,[43-44] as the Cu NWs were completely dissolved in 2-mercaptoethanol to form a transparent solution after stirring for 24 h at room temperature.

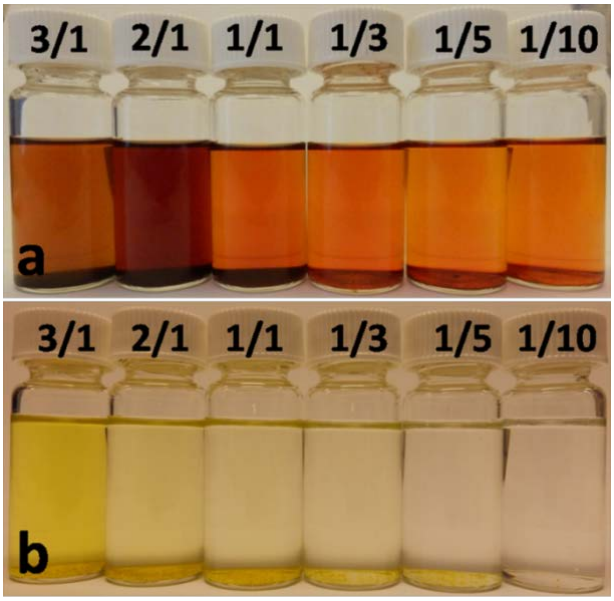

Figure 5.2 Optical images of Se powder (a) and S powder (b) dissolving in a different amount of 2-mercaptoethanol. The molar ratios of chalcogen to 2-mercaptoethanol are shown in the figure.

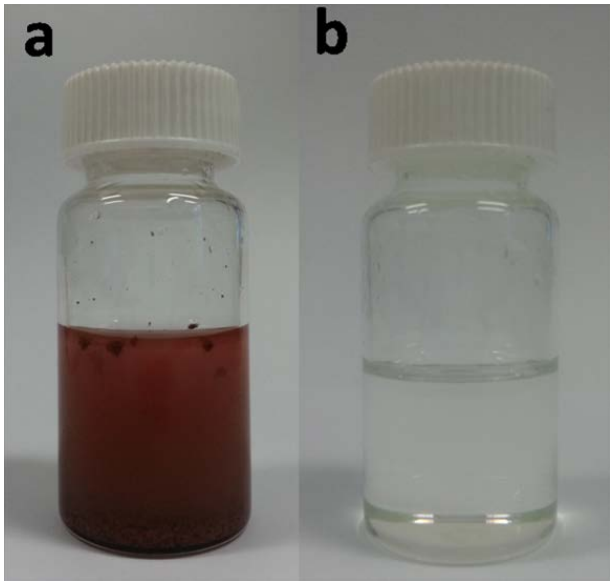

Figure 5.3 Optical images of Cu NWs stirred in pure 2-mercaptoethanol after (a) 5 min; (b) 24 h.

5.3.3 Results of synthesized $Cu_{2-x}Se$ and $Cu_{2-x}S$ NTs

$Cu_{2-x}Se$ NTs and $Cu_{2-x}S$ NTs were synthesized by the reaction of freshly-made Cu NWs with Se or S powder in ethanol in the presence of 2-mercaptoethanol. It should be noted that the reaction of Cu NWs with Se powder is faster than the reaction with S powder, as the Cu NWs changed from a deep red colour to black immediately when the Se powder was added. XRD patterns of $Cu_{2-x}Se$ NTs, $Cu_{2-x}S$ NTs, and Cu NWs are shown in Figure 5.4(a) and Figure 5.5(a). The strong and sharp diffraction peaks in the blue pattern match well with the (111), (220), (311), (400), and (331) planes of fcc Cu_2Se (JCPDS 88-2043), suggesting that the as-synthesized $Cu_{2-x}Se$ NTs are well crystallized and have a similar crystal structure to Cu_2Se [Figure 5.4(a)]. The four diffraction peaks in the red pattern are similar to the (102), (110), (103), and (112) planes of hexagonal Cu_2S (JCPDS31-0482), and they are slightly right shifted by about 0.73°. The FESEM image in Figure 5.5(b) clearly shows that the Cu NWs are straight, with diameters in the range of 160-360 nm (mostly ~300 nm) and lengths up to tens of micrometers. The uniform $Cu_{2-x}Se$ and $Cu_{2-x}S$ NTs have an inner diameter of 300 nm and an outer diameter of 600 nm on average [Figure 5.4(c, d)]. In addition to their different crystal structures, $Cu_{2-x}Se$ and $Cu_{2-x}S$ NTs also show a huge difference in surface structure, even though they were prepared under similar conditions, i.e. the surfaces of $Cu_{2-x}Se$ and $Cu_{2-x}S$ NTs are composed of nanosheets and nanoparticles, respectively.

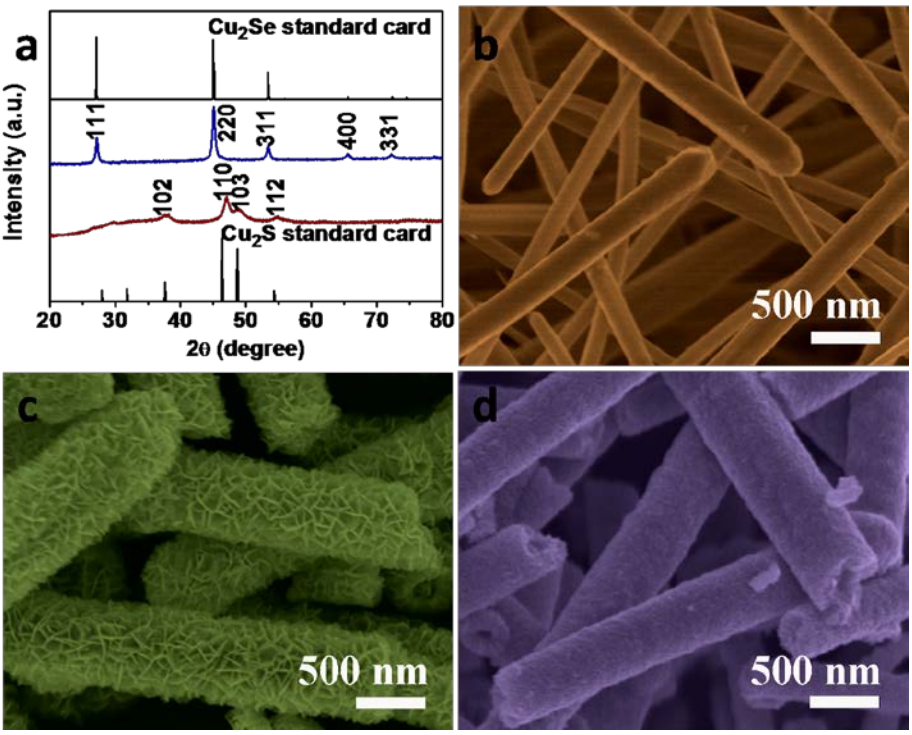

Figure 5.4 (a) XRD patterns of $Cu_{2-x}Se$ NTs and $Cu_{2-x}S$ NTs. The vertical lines mark the positions of Cu_2Se (JCPDS 88-2043) and Cu_2S (JCPDS 31-0482) standards. (b-d) FESEM images of the resultant Cu NWs, $Cu_{2-x}Se$ NTs, and $Cu_{2-x}S$ NTs, respectively.

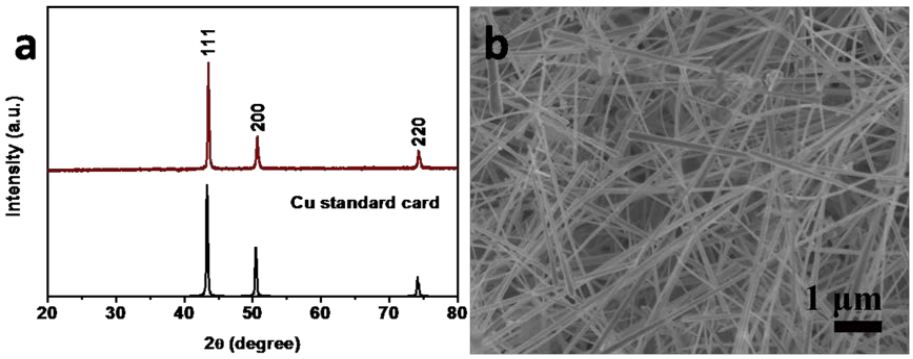

Figure 5.5 (a) XRD pattern of Cu NWs in comparison with the standard diffraction peak of Cu (JCPDS 65-9743). (b) Low-magnification SEM image of Cu NWs.

The TEM image in Figure 5.6 confirms the tubular structure of $Cu_{2-x}Se$ and $Cu_{2-x}S$ and their surface differences [Figure 5.6(a,c)]. The HRTEM images clearly display lattice fringes with a spacing of 0.33 nm and 0.31 nm [Figure 5.6(b,d)], which match well with those of the (111) planes of $Cu_{2-x}Se$ and (110) planes of $Cu_{2-x}S$, respectively. The FFT patterns also confirm their cubic and hexagonal structures. The average Cu/Se and Cu/S ratios were determined to be 1.77 and 2.37 by ICP-AES. The higher Cu/S ratio in $Cu_{2-x}S$ NTs suggests the incomplete conversion of Cu NWs within the reaction time.

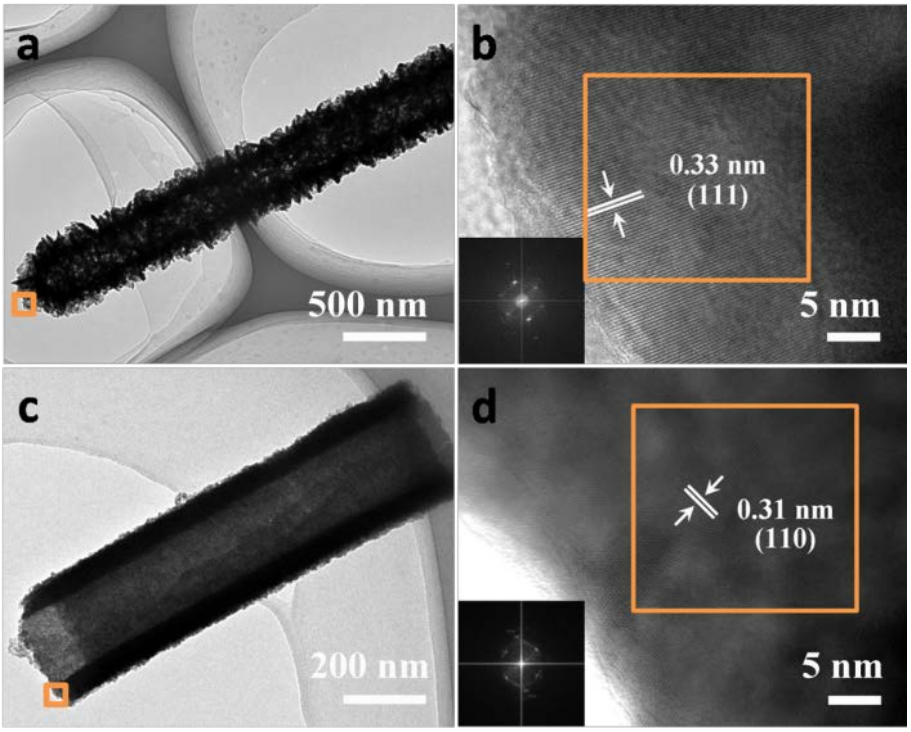

Figure 5.6 TEM and HRTEM images of the NTs: (a-b) $Cu_{2-x}Se$ NTs and (c-d) $Cu_{2-x}S$ NTs. Insets are fast Fourier transforms (FFT) of the HRTEM images of the selected areas in (b) and (d).

XPS was used to determine the ratios of different valence states of Cu in these $Cu_{2-x}Se$ and $Cu_{2-x}S$ samples (Figure 5.7). The XPS spectra of Cu 2p confirm the presence of both Cu^{2+} and Cu^{+} in both $Cu_{2-x}Se$ and $Cu_{2-x}S$ samples [Figure 5.7(a, c)].[49] The spectra of Se 3d and S 2p suggest the co-existence of Se^{2-} or S^{2-} together with a small amount of organic selenide and sulfide species, which could adsorb on the surface of NTs.[50-52]

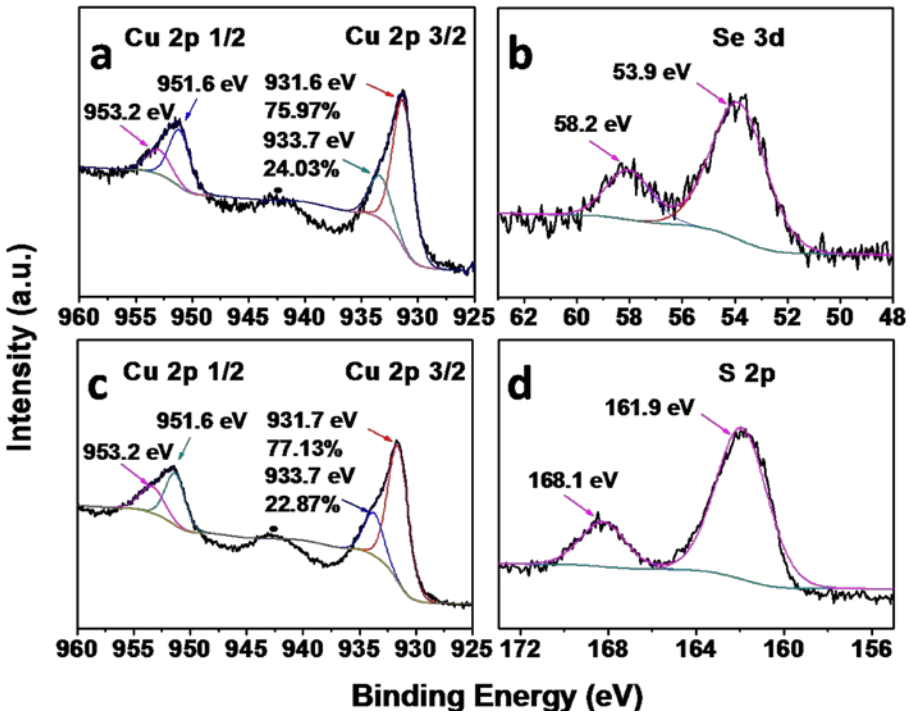

Figure 5.7 XPS spectra of (a) Cu 2p and (b) Se 3d of $Cu_{2-x}Se$ NTs; (c) Cu 2p and (d) S 2p of $Cu_{2-x}S$ NTs. The black dot in a and c marked the satellite peak of Cu^{2+}.

5.3.4 Morphology evolution of $Cu_{2-x}Se$ NTs

The above results demonstrate that Cu NWs reacted with selenothiolate (or thiosulphide) to form NTs with a hierarchical architecture. The evolution of the NTs was investigated by analyzing the intermediate products collected at different reaction times.

Figure 5.8 shows the XRD patterns and SEM images of samples collected after 5 min, 10 min, and 24 h during the formation of $Cu_{2-x}Se$ NTs. After the Se powder was added to the reaction solution, the surface Cu reacted with selenothiolateto form a thin layer of nanosheets on the Cu NWs to result in a Cu@$Cu_{2-x}Se$ core-shell structure, in which the internal Cu is still solid after a short reaction time (i.e., 5 min), as displayed in Figure 5.8(b). The XRD pattern of this sample also confirms a mixture of fcc Cu and a small amount of $Cu_{2-x}Se$. Increasing the reaction time to 10 minutes led to the formation of a hollow Cu@$Cu_{2-x}Se$ core-shell structure [Figure 5.8(c)], which exhibits a similar XRD pattern, except that the intensity of peaks arising from the Cu NWs is decreased and the peaks of $Cu_{2-x}Se$ become more pronounced. Further extension of the reaction time to 24 h resulted in pure $Cu_{2-x}Se$ NTs with large internal holes [Figure 5.8(d)], which demonstrates the complete transformation of Cu into $Cu_{2-x}Se$. These results demonstrate that $Cu_{2-x}Se$ NTs were formed through the self-sacrifice of Cu NWs.

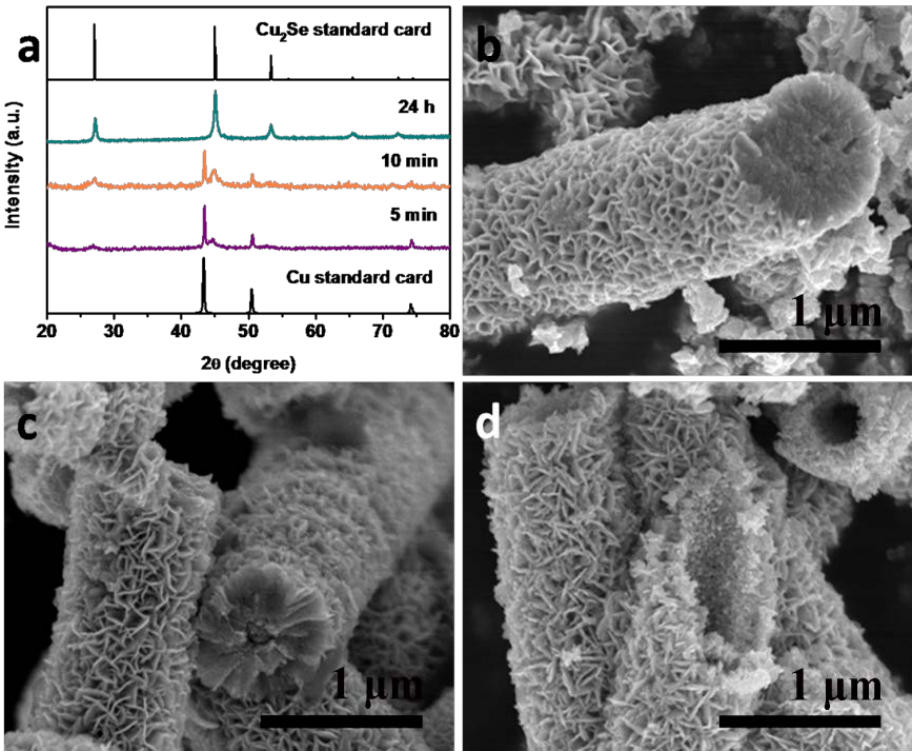

Figure 5.8 (a) XRD patterns of copper selenide samples collected after reaction times of 5 min, 10 min, and 24 h, showing the transformation of cubic Cu NWs into cubic $Cu_{2-x}Se$ NTs. The vertical lines mark the peak positions of Cu (JCPDS 65-9743) and Cu_2Se (JCPDS 88-2043) standards.FESEM images of the copper selenides collected after (b) 5 min, (c) 10 min, and (d) 24 h, showing the morphology evolution of $Cu_{2-x}Se$ NTs.

5.3.5 The functions of NaOH and 2-mercaptoethanol in reaction

In this reaction system, both NaOH and 2-mercaptoethanol play important roles in the formation of NTs. In order to demonstrate their importance, the clean Cu NWs were divided into four parts and respectively dispersed in (1) a mixture of ethanol and 2-mercaptoethanol; (2) a mixture of ethanol, 2-mercaptoethanol, and NaOH; (3) pure

ethanol; and (4) pure 2-mercaptoethanol. Then, the same amount of Se powder was added into the four mixtures and stirred for 24 h. The ratio of Cu NWs and Se powder (i.e., 1/1) in each case was the same as that used in the preparation of $Cu_{2-x}Se$ NTs. The results in Figure 5.9 clearly demonstrate that only the system containing both NaOH and 2-mercaptoethanol can form pure $Cu_{2-x}Se$ [Figure 5.9(b2)]. Other solutions without NaOH or 2-mercaptoethanol cannot produce pure products [Figure 5.9(b1, b4)]. It should be noted that when Cu NWs reacted with Se in pure 2-mercaptoethanol for a few days, the product was CuSe rather than $Cu_{2-x}Se$.[53]

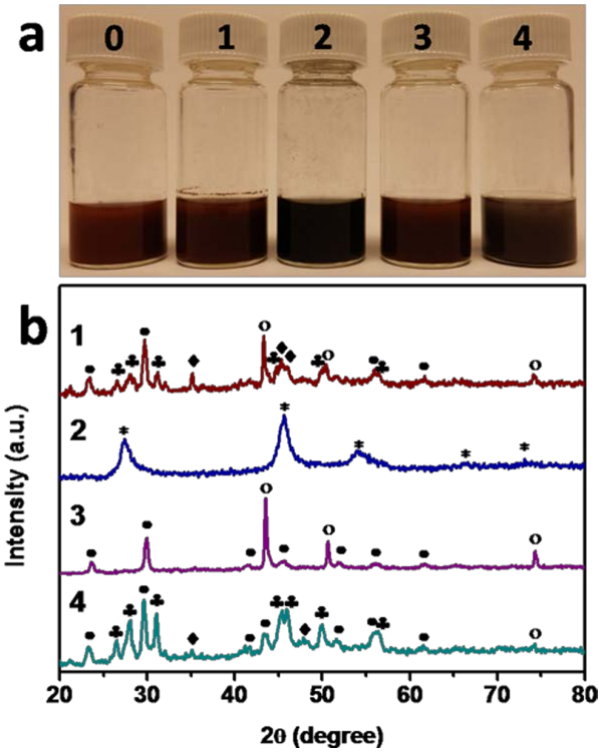

Figure 5.9 (a) Optical images of Cu NWs reacting with Se in different solutions: (a0) Cu NWs dispersed in pure ethanol; (a1) Cu NWs reacting with Se in 2-mercaptoethanol and ethanol after 24 h; (a2) Cu NWs reacting with Se in 2-mercaptoethanol, sodium

hydroxide, and ethanol after 24 h; (a3) Cu NWs reacting with Se in pure ethanol after 24 h; (a4) Cu NWs reacting with Se in pure 2-mercaptoethanol after 24 h. (b) XRD patterns of the samples collected from a1-a4. The diffraction peaks of Se, Cu, Cu_2Se, CuSe and Cu_3Se_2 are marked with·, º, *, ♣, and♦, respectively.

The role of NaOH was further addressed by the effects of the NaOH/2-mercaptoethanol ratio on the product. Figure 5.10 shows the XRD patterns of products prepared by adding different amounts of NaOH into a mixture with the same amounts of Cu, Se, 2-mercaptoethanol, and ethanol, i.e., the NaOH/2-mercaptoethanol ratio was varied from 1/600, through 1/60, 1/30, 1/15, 1/6, and 2/3, to 5/3. In the cases of low NaOH/2-mercaptoethanol ratios (i.e., 1/600 and 1/60), the XRD patterns of the products are indexed to be Cu (JCPDS 65-9743) and Se (JCPDS 06-0362), which means that a small amount of NaOH is not enough for the reaction of Cu NWs with Se powder. Increasing the amount of NaOH (i.e., the NaOH/2-mercaptoethanol ratio of 1/30 or 1/15) promoted the reaction and produced $Cu_{2-x}Se$ mixed with unreacted Se. Further increasing the amount of NaOH (i.e., the NaOH/2-mercaptoethanol ratio of 1/6, 2/3, or 5/3) led to pure products, as indicated by their XRD patterns, which match well with fcc Cu_2Se (JCPDS 88-2043). These results support the role of NaOH as the catalyst for the deprotonation of 2-mercaptoethanol for dissolving of Se or S powder in the reaction mixture.

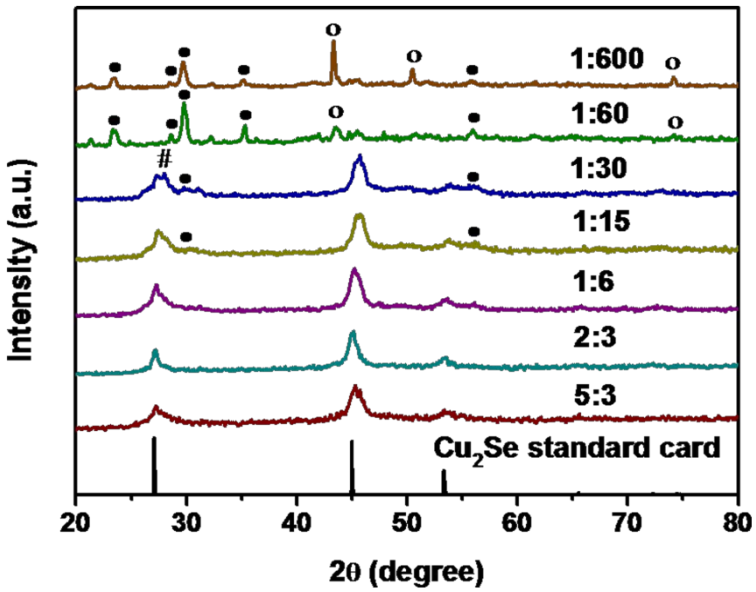

Figure 5.10 XRD patterns of the samples prepared by using different molar ratios of NaOH to 2-mercaptoethanol, i.e., 1/600, 1/60, 1/30, 1/15, 1/6, 2/3, and 5/3. The vertical lines indicate the peak positions of standard Cu_2Se (JCPDS 88-2043). The diffraction peaks of Se and Cu are marked with • and°, respectively.

5.3.6 Effects of chalcogen/2-mercaptoethanol ratios on $Cu_{2-x}Se$ and $Cu_{2-x}S$ NTs

As shown in Figure 5.2, more 2-mercaptoethanol helped Se powder to dissolve in the solution. The influence of 2-mercaptoethanol on $Cu_{2-x}Se$ NTs was investigated by varying the ratio of Se and 2-mercaptoethanol from 1/3 through 1/10, 1/20, and 1/30, to 1/50. The SEM images in Figure 5.11 clearly show that the ratio of NTs in the products decreases as the amount of 2-mercaptoethanol is increased, especially when the ratio of Se/2-mercaptoethanol is 1/50. This is attributed to the faster reaction in the case of more 2-mercaptoethanol and the disassembling of NTs under long-term magnetic stirring, as is

supported by the SEM images of the products prepared from a ratio of Se/2-mercaptoethanol of 1/50 and collected after different reaction times (Figure 5.12).

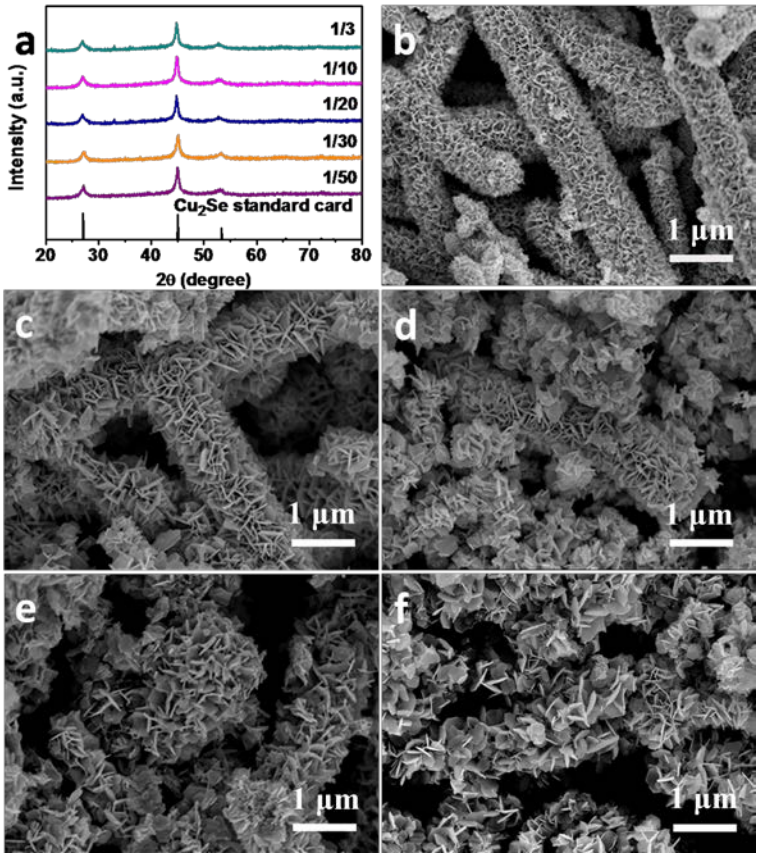

Figure 5.11 (a) XRD patterns of copper selenide samples with different molar ratios of Se to 2-mercaptoethanol; (b-f) FESEM images of the products prepared using different molar ratios of Se to 2-mercaptoethanol: 1/3, 1/10, 1/20, 1/30, and 1/50, respectively.

NTs are clearly observed after the reaction time of only 1 min, which is much shorter than that (10 min) needed in the case of a high Se/2-mercaptoethanol ratio (i.e., 1/3, Figure 5.8). The NTs became shorter and shorter with increasing reaction time under magnetic stirring and eventually disassembled into nanosheets. Similar effects are

observed during the preparation of $Cu_{2-x}S$ NTs with more 2-mercaptoethanol (i.e., ratios of S/2-mercaptoethanol are 1/10 and 1/20). As presented in Figure 5.13, the resultant $Cu_{2-x}S$ NTs have larger surface particles and rougher surfaces than those prepared from a ratio of S/2-mercaptoethanol of 1/3 (Figure 5.4).

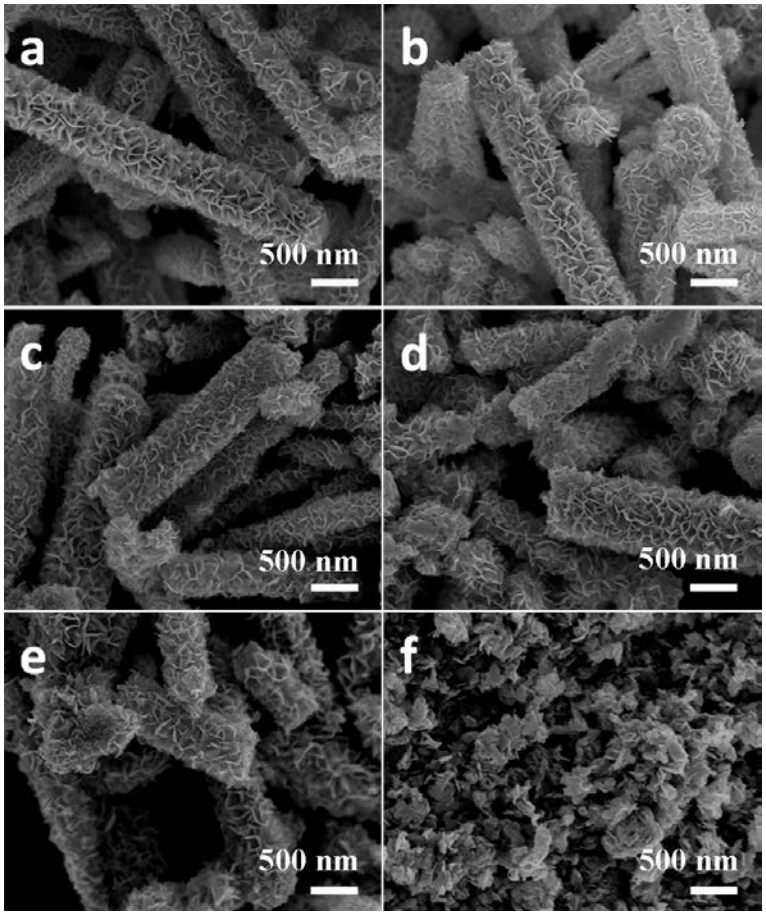

Figure 5.12 FESEM images of copper selenide samples with a ratio of Se/2-mercaptoethanol of 1/50 after different reaction times: (a) 1 min; (b) 3 min; (c) 5 min; (d) 10 min; (e) 20 min; and (f) 8 h.

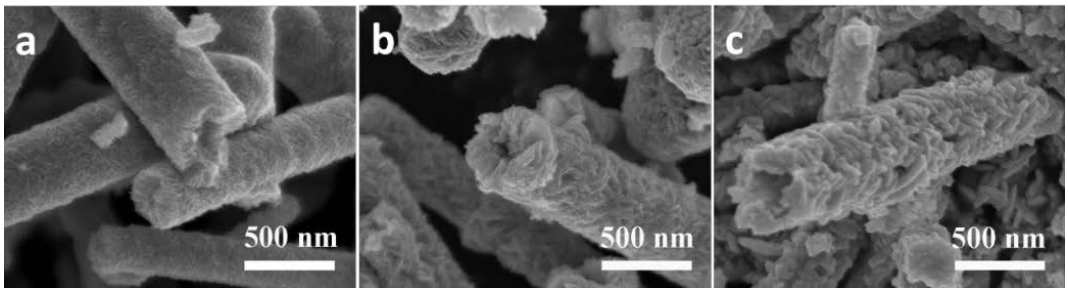

Figure 5.13 FESEM images of $Cu_{2-x}S$ NTs prepared using different molar ratios of S to 2-mercaptoethanol: (a) 1/3; (b) 1/10; (c) 1/20.

5.3.7 Effects of different thiol ligands

The room-temperature reaction of Cu NWs with Se (or S) powder can be also assisted with other thiol ligands, as long as their –SH groups can be deprotonated by a base. In addition to 2-mercaptoethanol, 1-dodecanethiol, 3-mercapto-1-propanol, 4-mercapto-1-butanol, thioglycolic acid, 3-mercaptopropionic acid, and cysteamine were also selected as ligands. The pK_a values of their functional groups are shown in Table 5.1, and the pK_a of their –SH groups is in the order of 1-dodecanethiol (14) > thioglycolic acid (10.7) ≈ 3-mercaptopropionic acid > 2- mercaptoethanol (9.61) ≈ 3-mercapto-1-propanol ≈ 4-mercapto-1-butanol > cysteamine (8.35). The obtained $Cu_{2-x}Se$ nanostructures are shown in Figure 5.14-5.15. Similar to the case of 2-mercaptoethanol, the products obtained from 1-dodecanethiol, 3-mercapto-1-propanol, 4-mercapto-1-butanol, and cysteamine are NTs [Figure 5.14(a-d)], which means that the terminal functional groups in these ligands had no influence on the deprotonation of –SH and the subsequent reaction, as the pK_a values of –OH [pK_a(-OH) of 16 in

2-mercaptoethanol) and $–NH_2$ (pK_a(-NH^{3+}) of 10.81 in cysteamine)] are higher than that of –SH group (Table 5.1).[54-55] The smaller pK_a of –SH suggests the stronger acidity of –SH than of the –OH and $–NH_2$ groups, and it would be preferentially deprotonated upon addition of NaOH solution. For the ligands containing –COOH and –SH, such as thioglycolic acid and 3-mercaptopropionic acid, the deprotonation of –SH and the reaction environment (e.g., solution pH) are strongly influenced by their –COOH groups [pK_a(-COOH) of 3.68 in thioglycolic acid]. Different nanostructures (e.g., nanosheets) were obtained as expected [Figure 5.14(e-f)]. These results show that the morphology of copper selenide nanostructures can be simply tuned by using different ligands, demonstrating the versatility of our novel approach.

Table 5.1 pK_a values of thiol ligands.

Thiol		pK_a(-SH)	pK_a(-OH)	pK_a(-COOH)	pK_a(-NH_3^+)
1-dodecanethil	HS-$(CH)_{11}$-CH_3	14	-	-	-
2-mercaptoethanol	HS-$(CH)_2$-OH	9.61	16	-	-
Cysteamine	HS-$(CH)_2$-NH_2	8.35	-	-	10.81
Thioglycolic acid	HS-CH_2-COOH	10.7	-	3.68	-

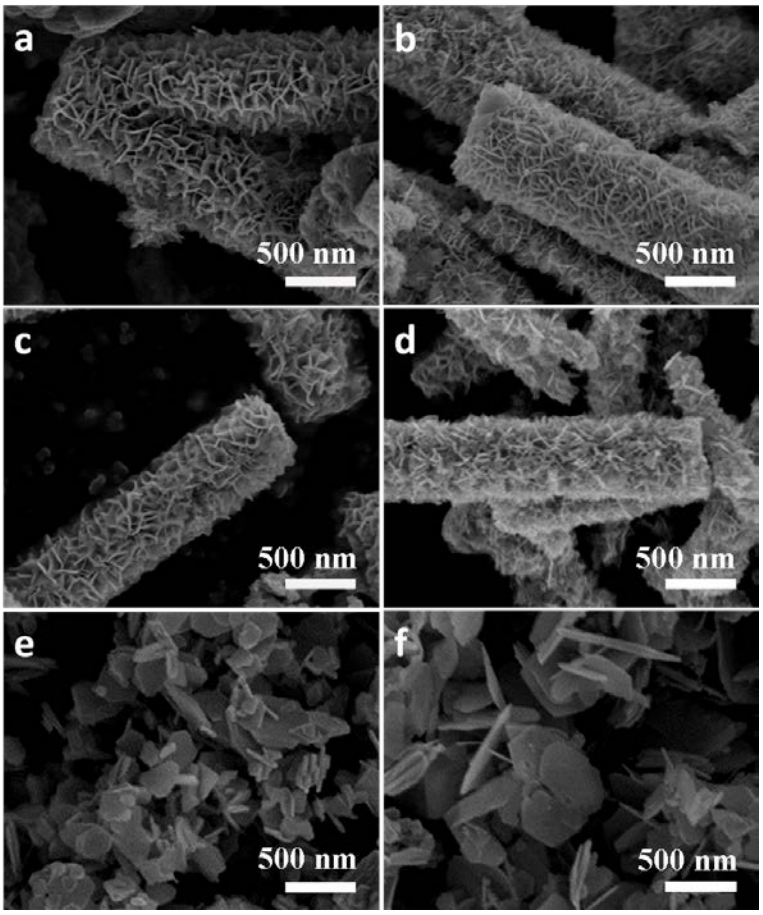

Figure 5.14 FESEM images of copper selenide samples prepared with different ligands: (a) 1-dodecanethiol; (b) 3-mercapto-1-propanol; (c) 4-mercapto-1-butanol; (d) cysteamine; (e) thioglycolic acid; and (f) 3-mercaptopropionic acid.

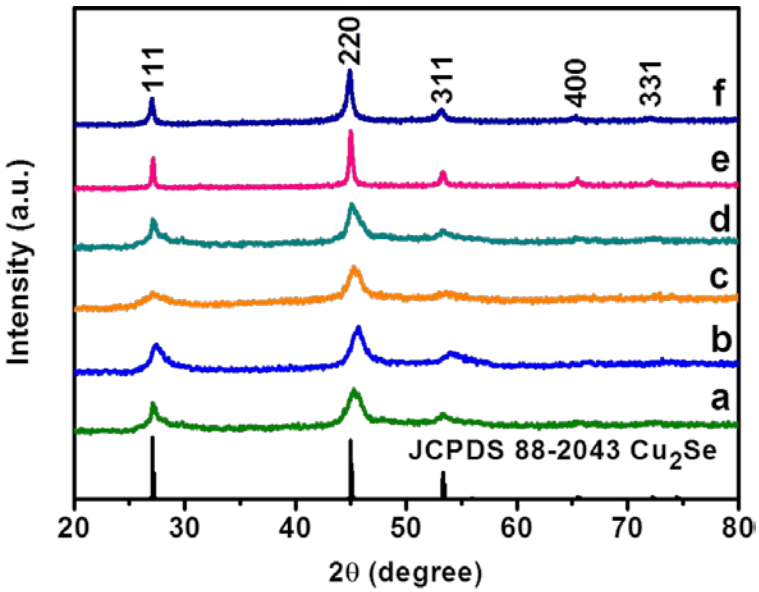

Figure 5.15 XRD patterns of copper selenide samples prepared with different ligands: (a) 1-dodecanethiol; (b) 3-mercapto-1-propanol; (c) 4-mercapto-1-butanol; (d) cysteamine; (e) thioglycolic acid; and (f) 3-mercaptopropionic acid.

5.3.8 Performances of QDSSCs with $Cu_{2-x}Se$ or $Cu_{2-x}S$ CEs

The hierarchical architecture of resultant $Cu_{2-x}Se$ and $Cu_{2-x}S$ NTs could provide large surface area and more reactive sites for electrochemical reactions. The surface areas of $Cu_{2-x}Se$ and $Cu_{2-x}S$ NTs are measured to be 13.34 and 7.98 m^2g^{-1}, respectively. They were fabricated into CEs of QDSSCs to evaluate their catalytic activity. A typical absorption spectrum [Figure 5.16(a)] of the TiO_2/CdS/CdSe electrodes reveals their absorbance from 400 to 800 nm. Figure 5.16(b) shows the *J-V* curves of the QDSSCs assembled using Au, $Cu_{2-x}Se$, and $Cu_{2-x}S$ as CEs. It should be noted that for the photovoltaic performance measurements, at least eight cells were constructed and evaluated in parallel. The average

photovoltaic performance parameters are summarized in Table 5.2. The open-circuit voltage (V_{oc}) and short-circuit current density (J_{sc}) were obtained from measured results. Fill factor (*FF*) is calculated by the ratio of maximum obtainable power to the product of the open-circuit voltage and short-circuit current. The energy conversion efficiency (η) is calculated by dividing a cell's power output (in watts) at its maximum power point (P_m) by the incidence (light), *G*, in W/m^2 and the surface area of the solar cell (A_c in m^2) Equation (5.7).

$$\eta = P_m/(G \times A_c) \quad (5.7)$$

Compared with conventional solar cells using Au CE, the cells made with $Cu_{2-x}Se$ or $Cu_{2-x}S$ CEs exhibit both higher V_{oc} (559 mV in $Cu_{2-x}Se$ and 536 mV in $Cu_{2-x}S$ vs. 449 mV) and higher *FF* (59.3 % in $Cu_{2-x}Se$ and 54.3 % in $Cu_{2-x}S$ vs. 46.4 %). The higher V_{oc} and *FF* of the devices with $Cu_{2-x}Se$ and $Cu_{2-x}S$ CEs are due to the higher catalytic activity of $Cu_{2-x}Se$ and $Cu_{2-x}S$ NTs than Au in this system. Although V_{oc} is theoretically determined by the potential different between the quasi-Fermi level of photoanode under illumination and the redox potential of the electrolyte, it can also be affected by the catalytic reactivity of CEs. As mentioned previously, sulfur-containing (S^{2-} or thiol) species are absorbed preferentially and strongly on the surface of Au, leading to surface passivation and a decrease in the catalytic reactivity. The low catalytic reactivity of Au CE leads to the reaction of polysulfide electrolyte with electrons generated from the photoanode, causing recombination and loss of V_{oc}.[6]

The obvious drop in the IPCE [Figure 5.16(c)] at around 630 nm corresponds to the absorption edge of the CdS/CdSe QDs. There is 12 % and 9 % enhancement, respectively, after replacement of Au CE with $Cu_{2-x}Se$ and $Cu_{2-x}S$ NT CEs, which is in agreement with the increase in the J_{sc}. However, J_{sc} is not the sole factor to affect the IPCE. In QDSSCs, multiple excitons (i.e., one photon absorbed generates more electrons) could benefit photocurrent significantly. The higher extinction coefficient of QDs also reduces the dark current and increases the overall efficiency.[6,56-57]

To probe the redox processes at the CE-polysulfide electrolyte interface and further clarify the electrochemical characteristics of various CEs in catalyzing the reduction of S_n^{2-}, EIS and Tafel-polarization measurements were carried out using dummy cells assembled with two identical electrodes (CE/electrolyte/CE). Figure 5.16(d) shows the Nyquist plots for dummy cells with different CEs, illustrating the impedance characteristics. The impedance characteristics of CEs for polysulfide electrolyte are determined by several operational circuit elements (Table 5.2): the series resistance (R_s), charge transfer resistance (R_{ct}), and Warburg diffusion impedance (Z_w), which are similar to those in the triiodide/iodide system used in DSSCs. The series resistance is composed of the bulk resistance of the CE materials, the resistance of the FTO substrate, and the contact resistance. The Warburg diffusion impedance (Z_w) describes the electrolyte diffusion resistance. The charge transfer resistance (R_{ct}) is a measure of the electrocatalytic activity towards the reduction of S_n^{2-}, which is the key step in the

catalytic process.[58-59] Therefore R_{ct} is the most important factor for evaluating the catalytic activity of a CE catalyst.[60-61] According to the equivalent circuit shown in the inset of Figure 5.16(d), the high-frequency intercept on the real axis represents the series resistance. The charge transfer resistance (R_{ct}) can be obtained by fitting the left arc in the middle-frequency region, which corresponds to the charge transfer process at the CE/electrolyte interface and changes inversely with the catalytic activity of the different CEs. The right-hand arc in the low-frequency range indicates the Warburg diffusion impedance (Z_w), which arises from mass transport limitations due to the diffusion of the S_n^{2-}/nS^{2-} couple within the electrolyte.[61-63] All these parameters were determined by fitting the impedance spectra using Z-view software and are summarized in Table 5.2. The $Cu_{2-x}Se$ NT CE possesses a smaller R_s of 11.1Ω compared to that of the $Cu_{2-x}S$ NT CE (17.5 Ω), indicating the superior electrical conductivity of $Cu_{2-x}Se$. More importantly, the $Cu_{2-x}Se$ NT CE shows the smallest R_{ct} (0.73 Ω), whilst Au exhibits the highest R_{ct} (37.97Ω), revealing the order of charge transfer resistance, which is the key factor dictating the electrocatalytic activity of the CEs, as discussed previously. This is consistent with the increased J_{sc} displayed in Table 5.2. In addition, the $Cu_{2-x}Se$ NT CE had a smaller Z_w as compared to the Au and $Cu_{2-x}S$ CEs, which indicates the efficient diffusion of polysulfide electrolyte. The remarkably increased *FF* of QDSSCs containing $Cu_{2-x}Se$ NT CEs may be attributed to the decreased Z_w as well as the R_s.[64] All these parameters together contribute to the excellent catalytic activity of the $Cu_{2-x}Se$ NT CE,

leading to the significantly enhanced performance of the QDSSCs. Tafel-polarization measurements were also conducted with the dummy cells used in the EIS experiments.

Figure 5.16(e) shows the logarithmic current density (log *J*) as a function of the voltage (*U*) for the oxidation/reduction of S_n^{2-} to nS^{2-}. The slopes of the anodic and cathodic branches are in the order of $Cu_{2-x}Se$ NT > $Cu_{2-x}S$ NT > Au. The larger slopes for the $Cu_{2-x}Se$ NT electrodes indicate the larger exchange current density (J_0),[61,65-66] which is in good agreement with the EIS parameters in terms of the following Equation (5.8).

$$J_0 = RT / nFR_{ct} \tag{5.8}$$

where *R* is the gas constant, *T* is the temperature, *F* is the Faraday constant, and *n* is the number of electrons involved in the electrochemical reduction of sulfur at the electrode. Obviously, the values for the calculated J_0 also follow the same order as above, which is consistent with the J_{sc} order in Table 5.2. Furthermore, the limiting current density (J_{lim}), determined by the diffusion of ionic carriers between the two electrodes, is directly proportional to the diffusion coefficient (*D*) of the S_n^{2-}/nS^{2-} redox couple.[65] As shown in Figure 5.16(e), the value of J_{lim} as well as *D* increases in the same order of $Cu_{2-x}Se$ NT > $Cu_{2-x}S$ NT > Au, which is in accordance with the EIS analysis on Z_w.[67] The diffusion coefficient *D* can be as obtained by Equation (5.9).

$$D = J_{lim} l / 2nFC \tag{5.9}$$

where *D* is the diffusion coefficient of the polysulfide electrolyte, *l* is the spacer thickness, *n* is the number of electrons involved in the reduction of sulfur at the electrode, *F* is the

Faraday constant, and *C* is the sulfide concentration. The electrochemical stability of the $Cu_{2-x}Se$ NT CEs was examined by Tafel polarization curve measurements. Figure 5.16(f) shows the Tafel polarization curves of the fresh and aged dummy cells over time. It is clear that $Cu_{2-x}Se$ NT CEs display an almost negligible change after 6 h in the Tafel curves. This suggests that the $Cu_{2-x}Se$ NT CEs are stable when in contact with polysulfide electrolyte. Considering the high performance and excellent stability of the $Cu_{2-x}Se$ NT CEs, $Cu_{2-x}Se$ NT is expected to have great potential to replace the widely used $Cu_{2-x}S$ in QDSSCs as a promising, more effective, and stable CE catalyst.

The excellent electrochemical performance of CEs made from $Cu_{2-x}Se$ and $Cu_{2-x}S$ NTs boost the conversion efficiency of QDSSCs to 6.25 % ($Cu_{2-x}Se$ CE) and 5.02 % ($Cu_{2-x}S$ CE), which are much higher than that obtained with conventional Au CEs (2.94 %), due to their unique structures and properties. More specifically, first, the hierarchical architecture of the nanotube structure provides the larger surface area (13.34 m^2/g for $Cu_{2-x}Se$ NTs and 7.98 m^2/g for $Cu_{2-x}Se$ NTs) for adsorption of polysulfide electrolyte (i.e., providing more catalytic sites) than the bulk metal electrode. Second, $Cu_{2-x}Se$ and $Cu_{2-x}S$ NTs are more stable than metal electrodes in polysulfide electrolyte, as they have high resistance to corrosion and passivation, and can retain good conductivity. Third, $Cu_{2-x}Se$ and $Cu_{2-x}S$ are essentially heavily self-doped semiconductors and exhibit excellent conductivity. Their diverse compositions and crystal structures allow their properties to be tuned over a wide range.

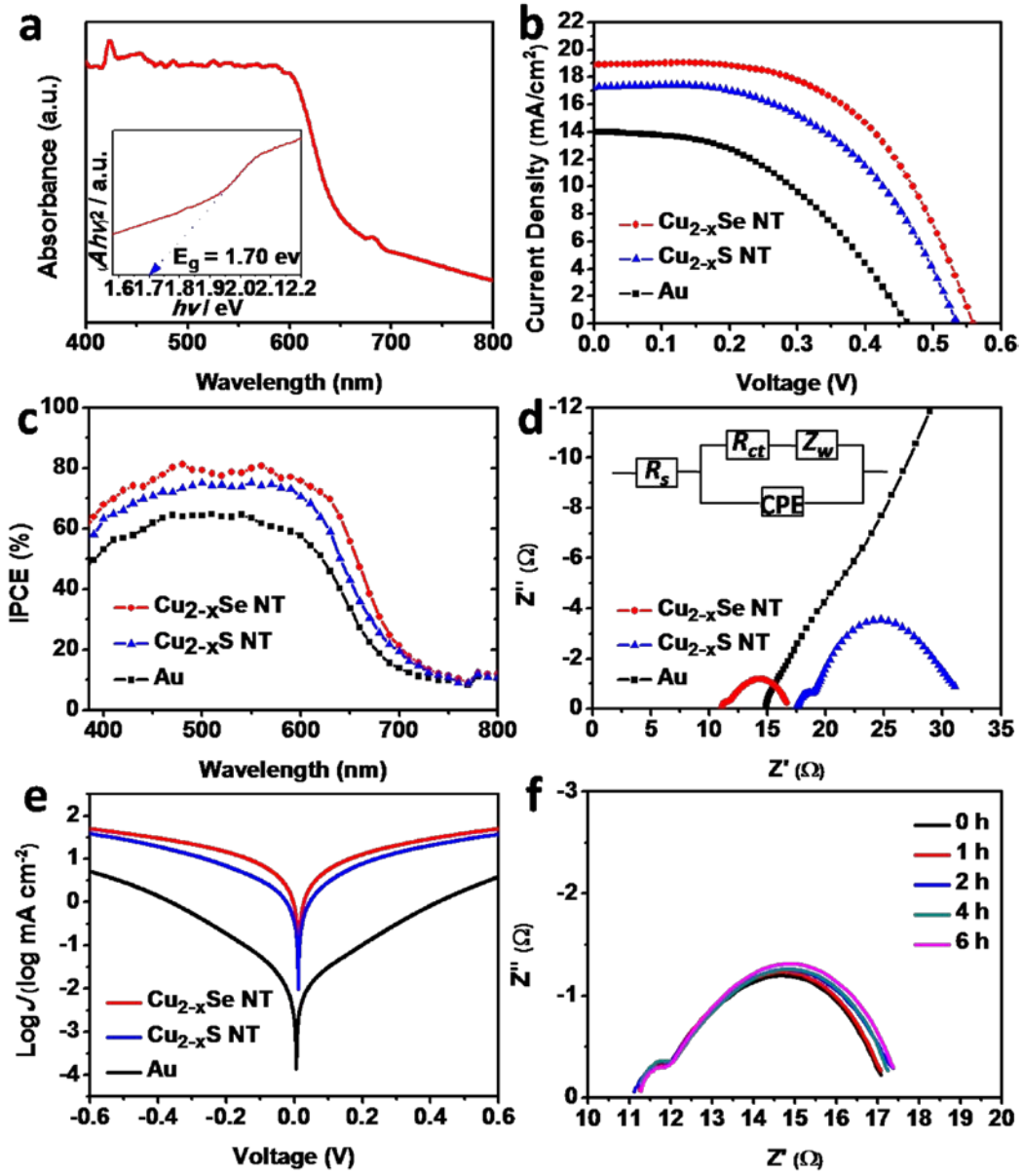

Figure 5.16 (a) Absorption spectrum of the as-prepared TiO_2/CdS/CdSe electrode. The inset contains plots of $(Ahv)^2$ vs. hv for the TiO_2/CdS/CdSe electrode. (b) Photocurrent-voltage (*J*-*V*) curves and (c) IPCE spectra of QDSSCs with different counter electrodes. (d) Nyquist plots of the symmetrical dummy cells fabricated with various CEs; the inset shows the equivalent circuit. (e) Tafel polarization curves of

different dummy cells that are the same as those used for EIS measurements. (f) Nyquist plots of the symmetrical dummy cells fabricated with $Cu_{2-x}Se$ CEs over time.

Table 5.2 Photovoltaic parameters of QDSSCs with different CEs.

CEs	V_{oc} (mV)	J_{sc} (mA cm^{-2})	FF (%)	η (%)	R_s (Ω)	R_{ct} (Ω)	Z_w (Ω)
$Cu_{2-x}Se$ NT	559	18.85	59.3	6.25	11.1	0.73	4.29
$Cu_{2-x}S$ NT	536	17.26	54.3	5.02	17.5	1.63	6.82
Au	449	14.12	46.2	2.94	14.8	37.97	77.61

5.4 Conclusions

In summary, $Cu_{2-x}E$ (E = S, Se) NTs with a hierarchical architecture were successfully synthesized at room temperature through the reaction of Cu NWs with sulfur or selenium powder in the presence of thiol ligands under the catalysis of NaOH. Cu NWs served as sacrificial templates during the formation of the nanotubes. NaOH played a role in

deprotonating –SH groups of thiol ligands and helped to dissolve of chalcogen precursors. A comprehensive investigation on the effects of reaction parameters demonstrates that this room-temperature reaction can occur as long as thiol group is deprotonated. The resultant $Cu_{2-x}E$ (E = S, Se) NTs have been used to fabricate high-performance CEs for QDSSCs, showing a higher conversion efficiency (up to 5.02 % and 6.25 %, respectively) than ever reported for Au CEs. This research provides a simple way to prepare copper chalcogenide nanostructures for diverse applications.

References

[1] Gonzalez-Pedro, V.; Xu, X. Q.; Mora-Sero, I.; Bisquert, J. *ACS Nano* **2010**, *4*, 5783.

[2] Ruhle, S.; Shalom, M.; Zaban, A. *ChemPhysChem* **2010**, *11*, 2290.

[3] Jiang, Y.; Zhang, X.; Ge, Q. Q.; Yu, B. B.; Zou, Y. G.; Jiang, W. J.; Song, W. G.; Wan, L. J.; Hu, J. S. *Nano Lett.* **2014**, *14*, 365.

[4] Yang, Z. S.; Chen, C. Y.; Liu, C. W.; Li, C. L.; Chang, H. T. *Adv. Energy Mater.* **2011**, *1*, 259.

[5] Bo, F.; Zhang, C. F.; Wang, C. L.; Xu, S. H.; Wang, Z. Y.; Cui, Y. P. *J. Mater. Chem. A* **2014**, *2*, 14585.

[6] Choi, H. M.; Ji, I. A.; Bang, J. H. *ACS Appl. Mater. Interfaces* **2014**, *6*, 2333.

[7] Lee, Y. L.; Lo, Y. S. *Adv. Funct. Mater.* **2009**, *19*, 604.

[8] Hodes, G.; Manassen, J.; Cahen, D. *J. Electrochem. Soc.* **1980**, *127*, 544.

[9] Yang, Z. S.; Chen, C. Y.; Liu, C. W.; Chang, H. T. *Chem. Commun.* **2010**, *46*, 5485.

[10] Xu, J.; Zhang, W. X.; Yang, Z. H.; Ding, S. X.; Zeng, C. Y.; Chen, L. L.; Wang, Q.; Yang, S. H. *Adv. Funct. Mater.* **2009**, *19*, 1759.

[11] Zhu, J. B.; Li, Q. Y.; Bai, L. F.; Sun, Y. F.; Zhou, M.; Xie, Y. *Chem. Eur. J.* **2012**, *18*, 13213.

[12] Deka, S.; Genovese, A.; Zhang, Y.; Miszta, K.; Bertoni, G.; Krahne, R.; Giannini, C.; Manna, L. *J. Am. Chem. Soc.* **2010**, *132*, 8912.

[13] Xie, Y.; Zheng, X. W.; Jiang, X. C.; Lu, J.; Zhu, L. Y. *Inorg. Chem.* **2002**, *41*, 387.

[14] Yu, R.; Ren, T.; Sun, K. J.; Feng, Z. C.; Li, G. N.; Li, C. *J. Phys. Chem. C* **2009**, *113*, 10833.

[15] Jagminas, A.; Juskenas, R.; Gailiute, I.; Statkute, G.; Tomasiunas, R. *J. Cryst. Growth* **2006**, *294*, 343.

[16] Hsu, Y. J.; Hung, C. M.; Lin, Y. F.; Liaw, B. J.; Lobana, T. S.; Lu, S. Y.; Liu, C. W. *Chem. Mater.* **2006**, *18*, 3323.

[17] Pai, R. R.; John, T. T.; Lakshmi, M.; Vijayakumar, K. P.; Kartha, C. S. *Thin Solid Films* **2005**, *473*, 208.

[18] Xue, M. Z.; Zhou, Y. N.; Zhang, B.; Yu, L.; Zhang, H.; Fu, Z. W. *J. Electrochem. Soc.* **2006**, *153*, A2262.

[19] Xiong, S. L.; Zeng, H. C. *Angew. Chem., Int. Edit.* **2012**, *51*, 949.

[20] Liu, X.; Wang, X. L.; Zhou, B.; Law, W. C.; Cartwright, A. N.; Swihart, M. T. *Adv. Funct. Mater.* **2013**, *23*, 1256.

[21] Zhang, G. Q.; Xia, B. Y.; Xiao, C.; Yu, L.; Wang, X.; Xie, Y.; Lou, X. W. *Angew. Chem., Int. Edit.* **2013**, *52*, 8643.

[22] Yin, Y. D.; Rioux, R. M.; Erdonmez, C. K.; Hughes, S.; Somorjai, G. A.; Alivisatos, A. P. *Science* **2004**, *304*, 711.

[23] Tan, M.; Chen, X. Q. *J. Electrochem. Soc.* **2012**, *159*, K15.

[24] Gates, B.; Mayers, B.; Wu, Y. Y.; Sun, Y. G.; Cattle, B.; Yang, P. D.; Xia, Y. N. *Adv. Funct. Mater.* **2002**, *12*, 679.

[25] Xu, J.; Zhang, W. X.; Yang, Z. H.; Yang, S. H. *Inorg. Chem.* **2008**, *47*, 699.

[26] Zhang, W. X.; Xu, J.; Yang, Z. H.; Ding, S. X. *Chem. Phys. Lett.* **2007**, *434*, 256.

[27] Li, Y. D.; Wang, Z. Y.; Ding, Y. *Inorg. Chem.* **1999**, *38*, 4737.

[28] Jiang, Y.; Wu, Y.; Xie, B.; Zhang, S. Y.; Qian, Y. T. *Nanotechnology* **2004**, *15*, 283.

[29] Li, Z.; Wei, J. Q.; Li, P. X.; Zhang, L. H.; Shi, E. Z.; Ji, C. Y.; Liu, J.; Zhuang, D. M.; Liu, Z. D.; Zhou, J.; Shang, Y. Y.; Li, Y. B.; Wang, K. L.; Zhu, H. W.; Wu, D. H.; Cao, A. Y. *Nano Res.* **2012**, *5*, 595.

[30] Herman, I.; Yeo, J.; Hong, S.; Lee, D.; Nam, K. H.; Choi, J. H.; Hong, W. H.; Lee, D.; Grigoropoulos, C. P.; Ko, S. H. *Nanotechnology* **2012**, *23*, 194005.

[31] Ko, S. H.; Lee, D.; Kang, H. W.; Nam, K. H.; Yeo, J. Y.; Hong, S. J.; Grigoropoulos, C. P.; Sung, H. J. *Nano Lett.* **2011**, *11*, 666.

[32] Lee, D.; Rho, Y.; Allen, F. I.; Minor, A. M.; Ko, S. H.; Grigoropoulos, C. P. *Nanoscale* **2013**, *5*, 11147.

[33] Mayousse, C.; Celle, C.; Carella, A.; Simonato, J. P. *Nano Res.* **2014**, *7*, 315.

[34] Perdew, J. P.; Burke, K.; Ernzerhof, M. *Phys. Rev. Lett.* **1996**, *77*, 3865.

[35] Grimme, S. *J. Comput. Chem.* **2006**, *27*, 1787.

[36] Sun, Q.; Li, Z.; Searles, D. J.; Chen, Y.; Lu, G. Q.; Du, A. J. *J. Am. Chem. Soc.* **2013**, *135*, 8246.

[37] Sun, Q.; Wang, M.; Li, Z.; Li, P.; Wang, W. H.; Tan, X. J.; Du, A. J. *Fuel* **2013**, *109*, 575.

[38] Sun, Q.; Wang, M.; Li, Z.; Ma, Y. Y.; Du, A. J. *Chem. Phys. Lett.* **2013**, *575*, 59.

[39] Halgren, T. A.; Lipscomb, W. N. *Chem. Phys. Lett.* **1977**, *49*, 225.

[40] Delley, B. *Mol. Simulat.* **2006**, *32*, 117.

[41] Delley, B. *J. Chem. Phys.* **1990**, *92*, 508.

[42] Delley, B. *J. Chem. Phys.* **2000**, *113*, 7756.

[43] Chang, Y.; Lye, M. L.; Zeng, H. C. *Langmuir* **2005**, *21*, 3746.

[44] Alia, S. M.; Pivovar, B. S.; Yan, Y. S. *J. Am. Chem. Soc.* **2013**, *135*, 13473.

[45] Tarabara, V. V.; Nabiev, I. R.; Feofanov, A. V. *Langmuir* **1998**, *14*, 1092.

[46] Afsar, H.; Tor, I.; Apak, R. *Analyst* **1989**, *114*, 1315.

[47] Afsar, H.; Apak, R.; Tor, I. *Analyst* **1989**, *114*, 1319.

[48] Amaratunga, W.; Milne, J. *Can. J. Chem.* **1994**, *72*, 2506.

[49] Xiong, J. Y.; Li, Z.; Chen, J.; Zhang, S. Q.; Wang, L. Z.; Dou, S. X. *ACS Appl. Mater. Interfaces* **2014**, *6*, 15716.

[50] Riha, S. C.; Johnson, D. C.; Prieto, A. L. *J. Am. Chem. Soc.* **2011**, *133*, 1383.

[51] Kuo, C. H.; Chu, Y. T.; Song, Y. F.; Huang, M. H. *Adv. Funct. Mater.* **2011**, *21*, 792.

[52] Fonder, G.; Volcke, C.; Csoka, B.; Delhalle, J.; Mekhalif, Z. *Electrochim. Acta* **2010**, *55*, 1557.

[53] Kumar, P.; Gusain, M.; Nagarajan, R. *Inorg. Chem.* **2012**, *51*, 7945.

[54] Pitman, I. H.; Morris, I. J. *Aust. J. Chem.* **1979**, *32*, 1567.

[55] Wallace, T. J. *J. Org. Chem.* **1966**, *31*, 1217.

[56] Lee, J. K.; Son, D. Y.; Ahn, T. K.; Shin, H. W.; Kim, I. Y.; Hwang, S. J.; Ko, M. J.; Sul, S.; Han, H.; Park, N. G. *Scientific Reports* **2013**, *3*, 1.

[57] Santra, P. K.; Kamat, P. V. *J. Am. Chem. Soc.* **2012**, *134*, 2508.

[58] Radich, J. G.; Dwyer, R.; Kamat, P. V. *J. Phys. Chem. Lett.* **2011**, *2*, 2453.

[59] Murakami, T. N.; Ito, S.; Wang, Q.; Nazeeruddin, M. K.; Bessho, T.; Cesar, I.; Liska, P.; Humphry-Baker, R.; Comte, P.; Pechy, P.; Gratzel, M. *J. Electrochem. Soc.* **2006**, *153*, A2255.

[60] Chen, J. K.; Li, K. X.; Luo, Y. H.; Guo, X. Z.; Li, D. M.; Deng, M. H.; Huang, S.

Q.; Meng, Q. B. *Carbon* **2009**, *47*, 2704.

[61] Wu, M. X.; Lin, X. A.; Hagfeldt, A.; Ma, T. L. *Angew. Chem., Int. Edit.* **2011**, *50*, 3520.

[62] Fabregat-Santiago, F.; Bisquert, J.; Palomares, E.; Otero, L.; Kuang, D. B.; Zakeeruddin, S. M.; Gratzel, M. *J. Phys. Chem. C* **2007**, *111*, 6550.

[63] Wang, Q.; Moser, J. E.; Gratzel, M. *J. Phys. Chem. B* **2005**, *109*, 14945.

[64] Wu, X.; Tian, F.; Wang, W. X.; Chen, J.; Wu, M.; Zhao, J. X. *J. Mater. Chem. C* **2013**, *1*, 4676.

[65] Hauch, A.; Georg, A. *Electrochim. Acta* **2001**, *46*, 3457.

[66] Zakeeruddin, S. M.; Gratzel, M. *Adv. Funct. Mater.* **2009**, *19*, 2187.

[67] Gong, F.; Wang, H.; Xu, X.; Zhou, G.; Wang, Z. S. *J. Am. Chem. Soc.* **2012**, *134*, 10953.

CHAPTER 6 Ambient Synthesis of One-Dimensional/Two-Dimensional CuAgSe Ternary Nanotubes as High-Performance Counter Electrodes of Quantum-Dot-Sensitized Solar Cells

Using the copper selenide ($Cu_{2-x}Se$) NTs as template (same prepared method as Chapter 5), 1D/2D ternary CuAgSe NTs were successfully prepared at room temperature within a short reaction time by the facile cation exchange approach. The cation exchange leads to the transformation of the crystal structure from cubic into orthorhombic and/or tetragonal with good retention of morphology. The exchange reactions are spontaneous due to their large negative changes of the Gibbs free energy (ΔG). The effects of parameters such as reaction time, precursor source, and precursor ratio on the exchange reaction were investigated. The resultant CuAgSe NTs were explored as CEs of QDSSCs and achieved much higher conversion efficiency (η = 5.61 %) than those of QDSSCs containing the noble-metal Au CE (3.32 %).

6.1 Introduction

1D/2D ternary semiconductor NTs have been the subject of extensive studies, not only because their electronic structures and properties can be engineered over a broad range of diverse applications such as photodetectors,[1-2] photovoltaics,[3] and electronics,[4] but also because their unique morphology consists of internal tubes and external nanosheets to

form a large surface area, which enables them to be good electron transporters and show better performance in comparison with solid analogues.[5] For example, ternary copper silver selenide (CuAgSe) has high mobility from both Cu^+ and Ag^+ ions, and displays better performance than binary Ag_2Se or Cu_2Se in electrochemical devices.[6-8] This material was initially reported in 1950 to have a tetragonal structure[9] and to have an orthorhombic structure in 1957[10]. It has been rarely studied in the past half century, however, due to the difficulty in its synthesis, especially for its nanostructures. Ternary CuAgSe is conventionally synthesized by heating a mixture of Ag, Cu, and Se powder to over 1000 K with several heating and cooling steps.[11-12] The thin CuAgSe films can be prepared by the electrodeposition method.[13] The crystal size of products generated by these methods is quite large and uncontrollable, and recent advances in nanofabrication have led to new insights into the preparation and application of ternary CuAgSe nanostructures. For example, surfactant-free CuAgSe nanoparticles were prepared on a large scale from copper nitrate, silver nitrate, and selenium powder under ambient conditions to show a temperature-dependent reversible transition of metallic-*n*-*p* conductivity, and great potential in converting heat into electricity through the Seebeck effect.[14] In addition to CuAgSe nanoparticles, CuAgSe dendrites were prepared by using dendritic Ag_2Se/Ag as a template.[15] The NT analogues were also synthesized by the reaction of Ag_2Se/Se NTs with fresh Cu nanoparticles in ammonia solution.[6] These two methods are time-consuming and difficult to avoid Ag or Se in the final products. Thus, a

facile and efficient method for the synthesis of CuAgSe nanomaterials with well-defined composition and architecture is desirable.

Compared with the aforementioned approaches, cation exchange has emerged as a particularly powerful and promising method to prepare well-defined nano-architectures, as it can retain the size and shape of the parent nanostructures.[16-20] It offers a new avenue to create chemically and compositionally diverse nanomaterials, and particularly suitable for the preparation of late-TMC nanostructures.[21-23] This strategy has been successfully applied to prepare heterostructured, doped, alloyed, hollow and core-shell nanocrystals, nanorods, and nanowires.[17,24-29] For example, the dual interface heterostructured copper sulfide layer capped with zinc sulfide grains in spherical nanocrystals were synthesized and the extent of the cation exchange can be precisely manipulated to tune the thickness of internal layer down to single atom level.[17] Hollow and cave nanoparticles $Cu_{2-x}S_ySe_{1-y}$ nanoparticles were prepared from core/shell $Cu_{2-x}Se/Cu_{2-x}S$ nanocrystals by the diffusion of Cu^+ from the $Cu_{2-x}Se$ core into the $Cu_{2-x}S$ shell.[29] Very recently, phase-selective cation exchange enables the successful transition of CdS NWs into $Cu_{2-x}S$ NWs with the tunable crystal structure.[28] Harder than partially or completely cation exchange between binary compounds, very few reports are available on the preparation of hierarchical 1D/2D ternary CuAgSe NTs by the ion exchange approach from binary compounds, however.

In this study, 1D/2D ternary CuAgSe NTs from $Cu_{2-x}Se$ NTs were synthesized through

the facile cation exchange method at room temperature in a short reaction time. The resultant CuAgSe NTs employed as the CEs of QDSSCs to generate the conversion efficiency (η) of 5.61 %. To the best knowledge, this is the first report on 1D/2D ternary CuAgSe NTs and their application in QDSSC.

6.2 Experimental section

6.2.1 Synthesis of CuAgSe NTs

$Cu_{2-x}Se$ NTs were prepared as described in chapter 5. In a typical synthesis, 0.15 mmol as-prepared $Cu_{2-x}Se$ NTs were dispersed in 0.5 mL anhydrous ethanol, followed by adding 2.5 mL silver nitrate or silver acetate (0.15 mmol) ethanol solution under gentle stirring for 20-40 min. The black precipitates were purified by distilled water and ethanol several times and then dried at room temperature.

6.2.2 Evolution of CuAgSe NTs

The evolution of NTs was investigated by characterizing samples collected at different reaction times. Two groups of experiments were carried out. The first group experiments were performed by using silver nitrate for the cation exchange reaction, and the samples were collected at 1 min, 2 min, 10 min, and 20 min. The second group experiments were conducted by using silver acetate for cation exchange, and the samples were collected at 1 min, 2 min, 10 min, 20 min, and 60 min.

6.3 Results and discussion

6.3.1 Results of synthesized CuAgSe NTs

1D/2D ternary CuAgSe NTs were fabricated by cation exchange from freshly-made $Cu_{2-x}Se$ NTs reacted with $AgNO_3$ ethanol solution. A typical FESEM image of the initial $Cu_{2-x}Se$ NTs shows their 1D/2D morphology with an inner diameter of 300 nm and an outer diameter of 600 nm on average [Figure 6.1(a)]. After a partial exchange of copper ions with silver ions, the nanosheets on the surfaces of the resultant CuAgSe NTs become smaller [Figure 6.1(d)], and their 1D/2D tubular structure is well retained. The TEM images of $Cu_{2-x}Se$ and CuAgSe NTs [Figure 6.1(b, e)] further confirm the good retention of 1D/2D morphology before and after cation exchange. Their HRTEM images clearly display continuous lattice fringes with spacings of 0.33 nm and 0.2 nm [Figure 6.1(c, f)], which match well with those of the (111) planes of $Cu_{2-x}Se$ and the (152) planes of CuAgSe, respectively. Their FFT patterns also support the transition of the crystal structure from cubic $Cu_{2-x}Se$ to orthorhombic CuAgSe after cation exchange. A scanning

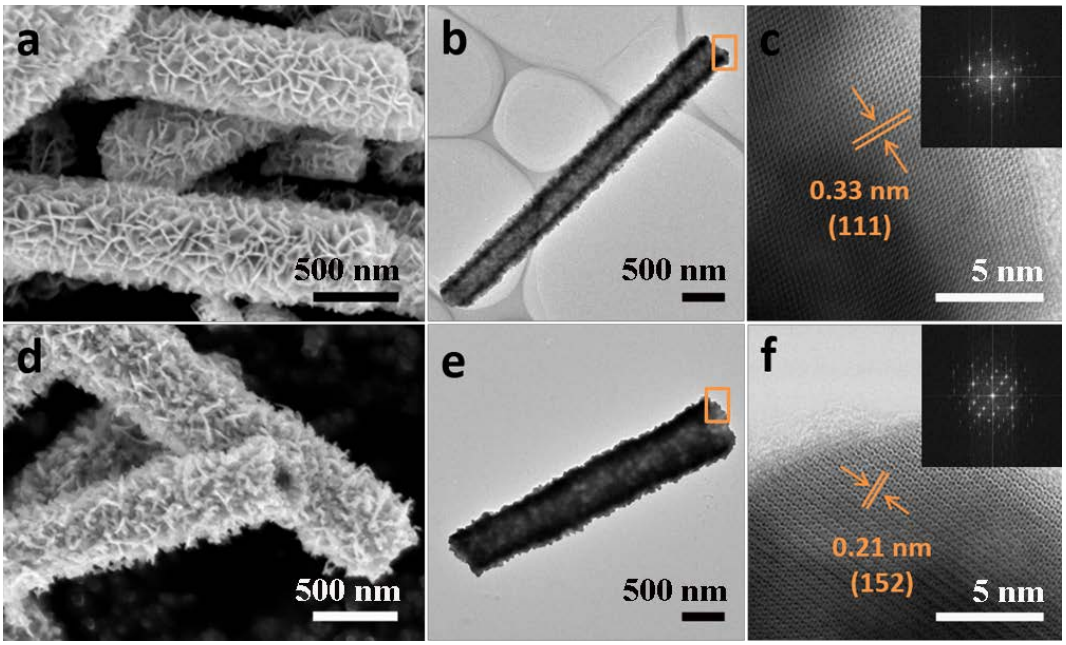

Figure 6.1 (a, d) FESEM images of the $Cu_{2-x}Se$ NTs and the resultant CuAgSe NTs, respectively. (b, e) TEM images of $Cu_{2-x}Se$ NT and CuAgSe NT. (c, f) HRTEM images of the selected areas in (b) and (e), respectively. Insets are FFT patterns of the HRTEM images.

TEM image and the corresponding EDX elemental mapping images of a single $Cu_{2-x}Se$ NT and a CuAgSe NT are shown in Figure 6.2, respectively, revealing the homogeneous distribution of Cu and Se throughout the whole $Cu_{2-x}Se$ NT and Cu, Ag, and Se throughout the whole CuAgSe NT. The EDX spectrum of an individual CuAgSe NT (Figure 6.3) further confirms that the NT is composed of Cu, Ag, and Se in the ratio of 1.46/1.1/1, which is consistent with that (1.22/1/1.04) determined by ICP-AES.

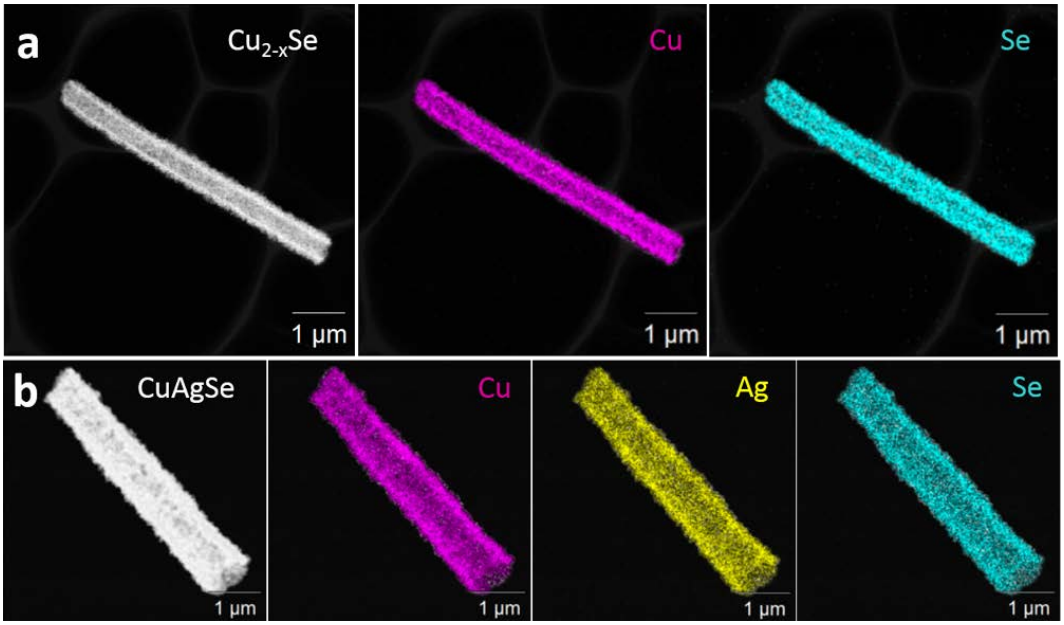

Figure 6.2 Scanning TEM image and EDX elemental mapping of (a) Cu and Se for a typical $Cu_{2-x}Se$ NT, (b) Cu, Ag, and Se for a typical CuAgSe NT.

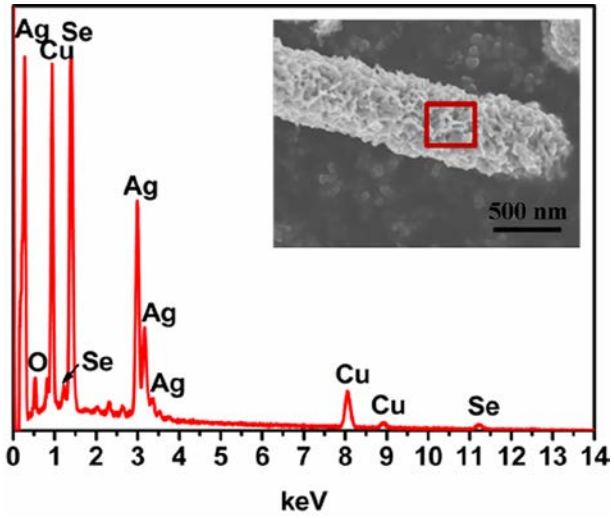

Figure 6.3 EDS of the CuAgSe NTs. Inset is an FESEM image of a single CuAgSe NT. The red square marks the area for collecting the EDS spectrum.

The transformation of $Cu_{2-x}Se$ NTs into CuAgSe NTs is further proved by the XRD patterns (Figure 6.4). The diffraction peaks in the orange pattern match well with orthorhombic CuAgSe (JCPDS 10-0451) and tetragonal CuAgSe (JCPDS 25-1180) [Figure 6.4(b)], which are absolutely different from those in the cubic structure of $Cu_{2-x}Se$ (JCPDS 88-2043) [Figure 6.4(a)].

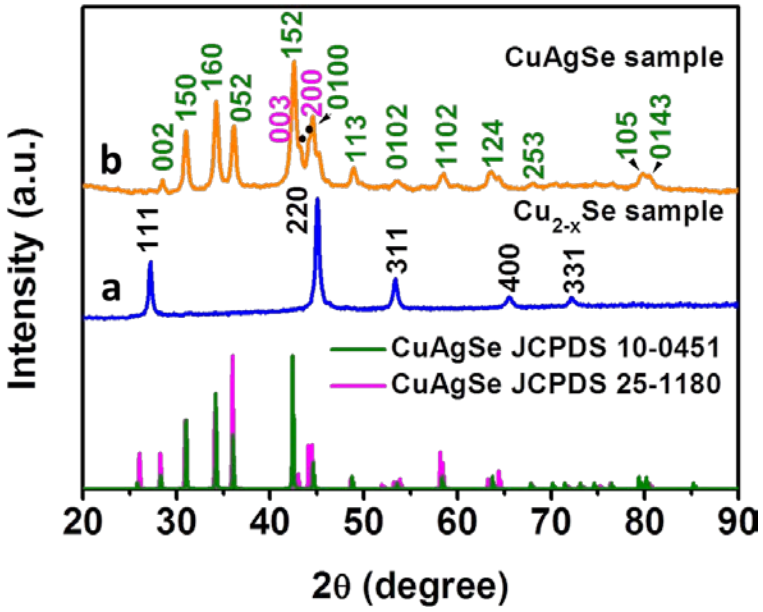

Figure 6.4 XRD patterns of (a) $Cu_{2-x}Se$ NTs and (b) CuAgSe NTs with standard XRD peaks.

It should be noted that there is no big difference between these two structures, except that the orthorhombic structure features a sequence which repeats itself periodically every five tetragonal cells in the b direction (Figure 6.5).[14] They have a similar layered structure with the alternating stacking of the Ag and CuSe layers, in which Ag atoms almost lie in the same plane and are bonded closely to Se atoms, allowing high mobility

of Ag atoms and the formation of Ag-Ag metallic bonds. Se atoms form a squashed tetrahedron, in which each corner is shared with adjacent tetrahedron, and Cu atoms are offset from the center within the tetrahedron.[10]

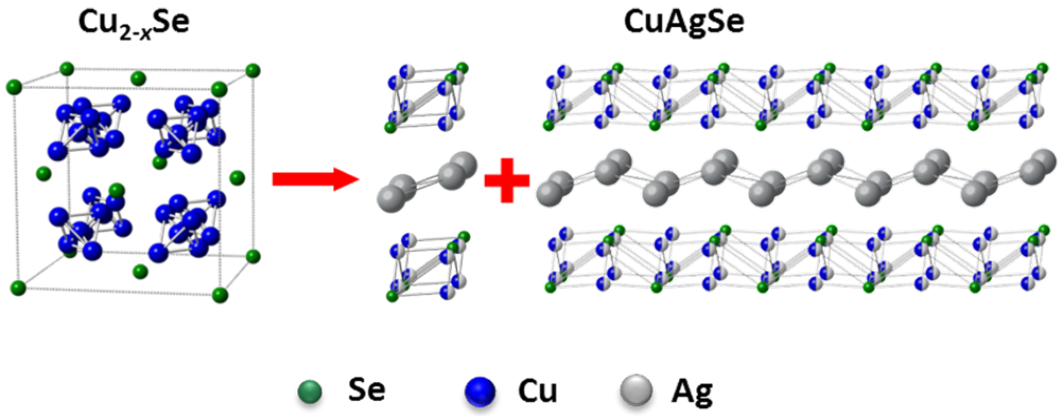

Figure 6.5 Structure diagrams of cubic $Cu_{2-x}Se$, tetragonal and orthorhombic CuAgSe unit cells.

As stoichiometric Cu_2Se is easily oxidized into non-stoichiometric $Cu_{2-x}Se$,[30] XPS was used to determine the valence states of elements in both $Cu_{2-x}Se$ and CuAgSe NTs (Figure 6.6). The spectra of Cu 2p [Figure 6.6(b)] confirm the presence of both Cu^+ and Cu^{2+} (with their ratio calculated to be 3.16) in $Cu_{2-x}Se$ NTs, from which the Cu^{2+} ions were completely transformed into Cu^+ in CuAgSe NTs after cation exchange, as evidenced by the disappearance of the characteristic peak of Cu^{2+} at around 942 eV. Two peaks at 373.2 eV and 367.6 eV of Ag 3d in the product indicate the high purity of the CuAgSe NTs and the absence of other Ag species [Figure 6.6(c)]. The binding energy of Se $3d_{3/2}$ at 53.7 eV corresponds to Se^{2-} in both $Cu_{2-x}Se$ and CuAgSe NTs [Figure 6.6(d)],

and the small peak at 58.2 eV in the $Cu_{2-x}Se$ sample is attributed to the surface adsorbed Se (with the ratio of Se^{2-} to Se^{0} in $Cu_{2-x}Se$ calculated to be 3.33).[14,31]

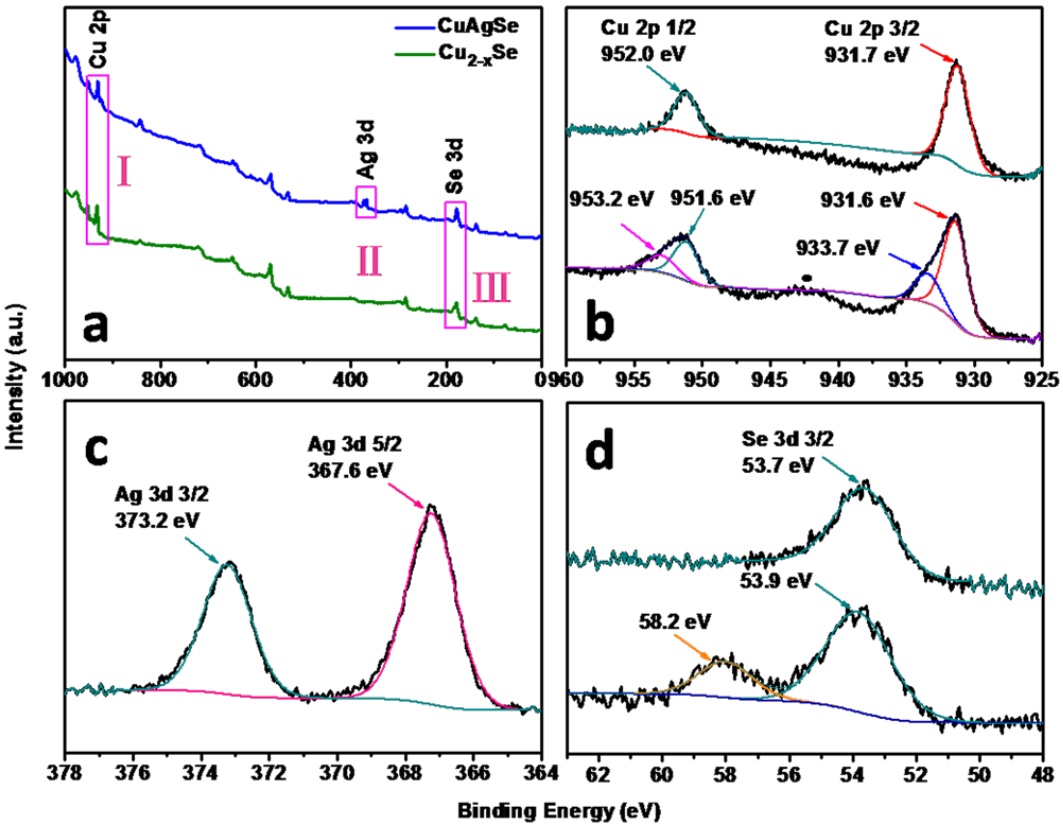

Figure 6.6 XPS spectra of the $Cu_{2-x}Se$ and CuAgSe NTs: (a) survey spectra; (b) Cu 2p spectrum of area Ⅰ in (a), with the black dot marking the satellite peak of Cu^{2+}; (c) Ag 3d spectrum of area Ⅱ in (a); (d) Se 3d spectrum of area Ⅲ in (a).

6.3.2 Morphology evolution of CuAgSe NTs

The exchange reaction was investigated by analyzing the intermediate products collected after different reaction times. Figure 6.7 shows the XRD patterns of samples collected at 1 min, 2 min, 10 min, and 20 min during the exchange reaction. When

$Cu_{2-x}Se$ ethanol solution was reacted with $AgNO_3$ ethanol solution for 1 min, the product obtained is a mixture of CuAgSe, Ag_2Se, and a small amount of Ag. This result demonstrates the fast exchange reaction between copper ions and silver ions, which is attributed to their strong mobility and capability for diffusion into/out of the lattice. After reaction for 2 minutes, the product is still composed of these three compounds, but the amount of Ag_2Se and Ag is decreased, as indicated by the lower intensity of the peaks in their XRD patterns. The intermediate sample collected at 10 min is a mixture of CuAgSe and Ag_2Se, and the Ag has disappeared or is not detectable. The final product collected at 20 min shows single phase CuAgSe, demonstrating the complete transformation of $Cu_{2-x}Se$ NTs into CuAgSe NTs.

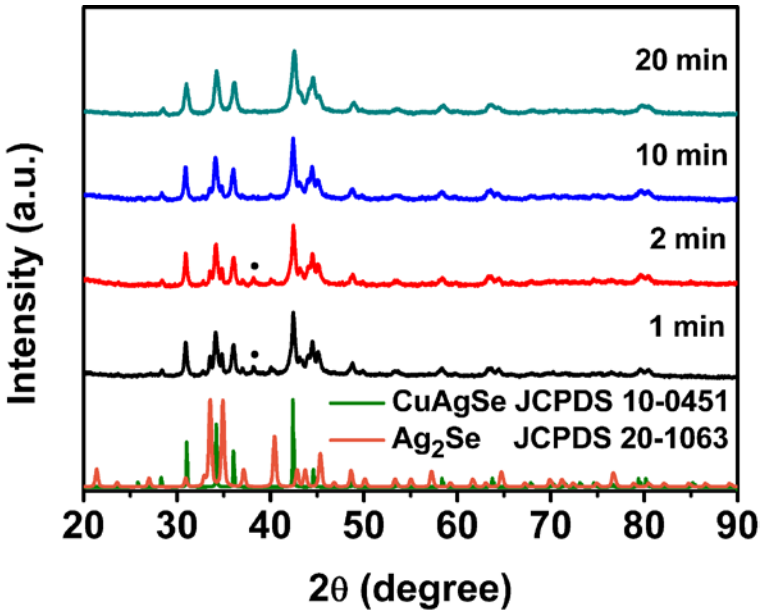

Figure 6.7 XRD patterns of CuAgSe samples prepared from silver nitrate and collected after different reaction times. The diffraction peaks marked with • arise from Ag.

The transformation is also supported by the XPS spectra of Ag^+ and Ag^0 in all the samples collected at different reaction times (Figure 6.8). Within the initial 2 min, Ag $3d_{5/2}$ peaks in the collected samples can be fitted into two peaks at 368.7 eV and 367.3 eV, which match well with those from Ag^0 and Ag^+. The Ag^0/Ag^+ ratios in the samples collected at 1 min and 2 min is decreased from 12.83 to 10.48, which means that there is the conversion of Ag^0 into Ag^+ (i.e., Ag_2Se and CuAgSe) as the reaction time is extended. When the mixture was reacted for 10 min, the absence of any Ag^0 peak suggests that all the Ag that had been formed was completely converted, which is consistent with the XRD results.

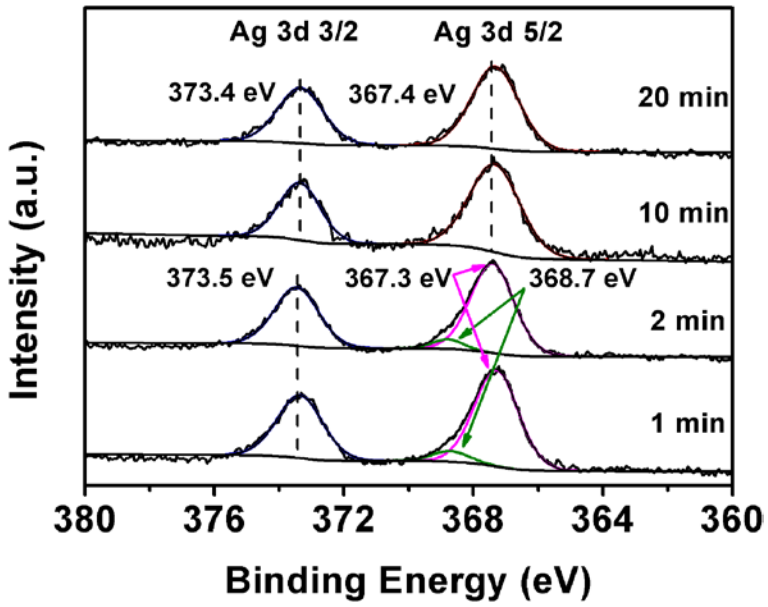

Figure 6.8 XPS spectra of Ag 3d in the samples prepared from silver nitrate and collected after different reaction times.

The evolution of the morphology during the cation exchange was monitored by SEM. Figure 6.9 shows SEM images of four samples collected at 1 min, 2 min, 10 min, and 20 min, respectively. There is no big difference in their morphologies, except that the surface nanosheets became thicker and rougher with increasing reaction time.

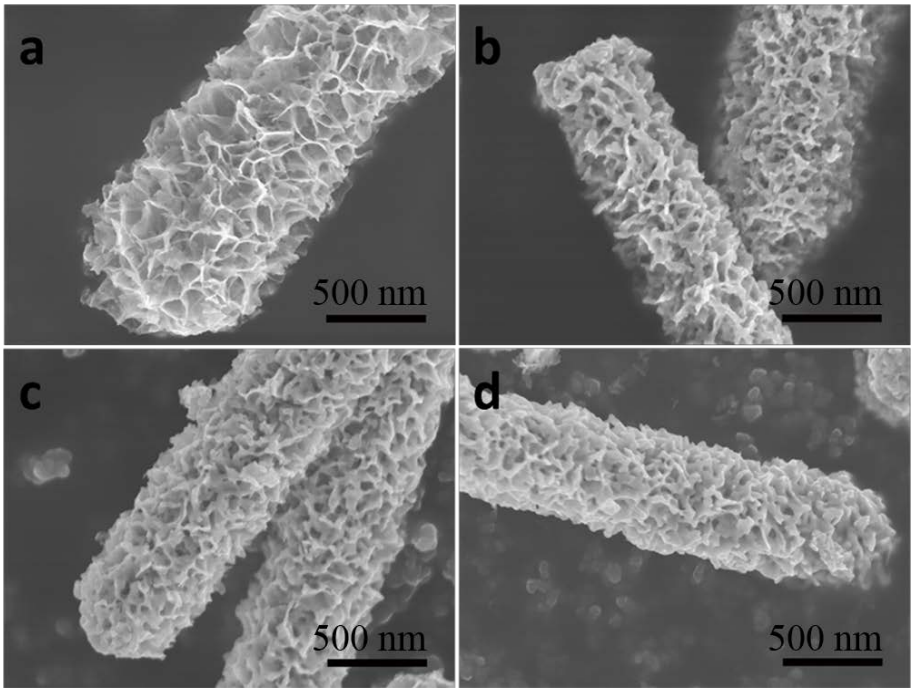

Figure 6.9 SEM images of NTs from cation exchange by silver nitrate that were collected after different reaction times: (c) 1 min; (d) 2 min; (e) 10 min, and (f) 20 min.

6.3.3 Formation mechanism CuAgSe NTs

From the formula perspective, $Cu_{2-x}Se$ ($0 \leq x \leq 1$) could be considered as a mixture of CuSe and Cu_2Se, and the transformation of $Cu_{2-x}Se$ into CuAgSe could be treated as their reactions with $AgNO_3$ [Equations (6.1-6.2)]. Cu_2Se could react with $AgNO_3$ to form CuAgSe, Ag, and $Cu(NO_3)_2$ due to the redox reaction between Cu^+, Ag^+, and

NO_3^-,evidenced by the XRD and XPS peaks of metallic Ag. CuSe reacted with $AgNO_3$ to form Ag_2Se due to its larger solubility [K_{sp} (CuSe) = 7.94×10^{-49}] than that of Ag_2Se [K_{sp} (Ag_2Se) = 2.0×10^{-64}], which was proved by mixing pure CuSe ethanol solution with $AgNO_3$ ethanol solution at room temperature to form Ag_2Se [Figure 6.10]. The characteristic blue solution suggests the formation of $Cu(NO_3)_2$ during exchange reactions. The thus-formed Ag reacted with residual Se (adsorbed by $Cu_{2-x}Se$ NTs) to form Ag_2Se [Equation (6.3)], which further reacted with Cu_2Se to form CuAgSe [Equation (6.4)].[14]

$$Cu_2Se + 2AgNO_3 \rightarrow CuAgSe + Ag + Cu(NO_3)_2 \quad (6.1)$$

$$CuSe + 2\ AgNO_3 \rightarrow Ag_2Se + Cu(NO_3)_2 \quad (6.2)$$

$$2Ag + Se \rightarrow Ag_2Se \quad (6.3)$$

$$Cu_2Se + Ag_2Se \rightarrow 2CuAgSe \quad (6.4)$$

These exchange reactions took place spontaneously due to three factors. First, the high mobility of Cu^{2+}, Cu^+, and Ag^+ ions and their strong capability for diffusion into/out of the lattice ensure the fast reactions. The presence of copper vacancies also significantly accelerated the cation exchange process at room temperature.[32] Second, the changes of Gibbs free energies (ΔG) for reactions (6.1-6.4) calculated to be -85.7, -55.8, -43.5 and -84.4 kJ mol^{-1} based on the assumption that the reaction temperature was constant at 298 K and no entropy change occurred during the reaction. The standard $\Delta_f H^0$ at 298 K for Cu_2Se, CuSe, Ag_2Se, $AgNO_3$, $Cu(NO_3)_2$ and CuAgSe are -65.3, -41.8, -43.5, -124.4,

-302.9 and -96.9 kJ mol^{-1}, respectively.[6-7,33-34] Third, the similar crystal structure (i.e., orthorhombic) of intermediate Ag_2Se and the CuAgSe product minimize the distortion of the crystal structure.

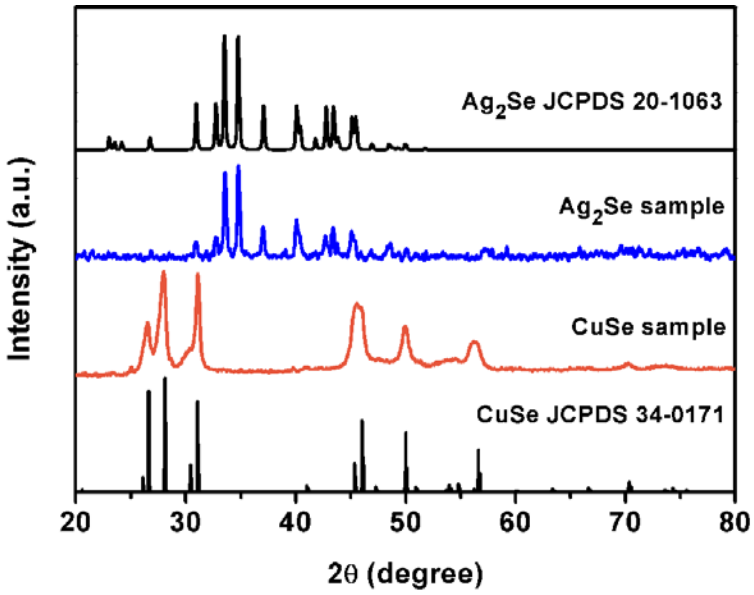

Figure 6.10 XRD patterns of CuSe and the resultant Ag_2Se.

6.3.4 Effects of reaction parameters

To demonstrate these exchange reactions, the effects of the molar ratio of $Cu_{2-x}Se$ NTs to $AgNO_3$ on the product were investigated. In the cases of more $Cu_{2-x}Se$ NTs (i.e., $Cu_{2-x}Se$/ $AgNO_3$ = 2.5/1 or 1.5/1), there is insufficient $AgNO_3$ for the reactions, and the main product is $Cu_{2-x}Se$, which is labeled with * in Figure 6.11. In the opposite cases (i.e., $Cu_{2-x}Se$/ $AgNO_3$ = 1/2 or 1/3), the excess of $AgNO_3$ leads to the formation of Ag (marked with ∆ in Figure 6.11). Therefore, it is crucial to control the molar ratio of $Cu_{2-x}Se/AgNO_3$, and the optimal ratio is 1/1.

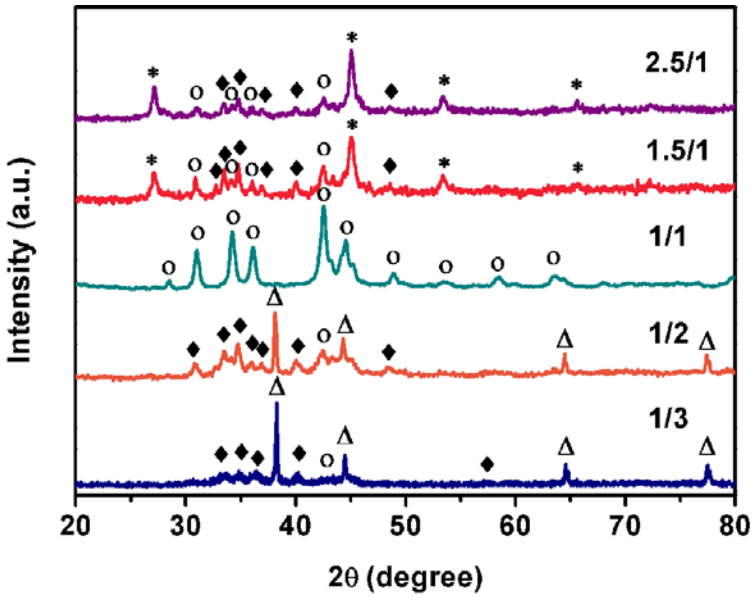

Figure 6.11 XRD patterns of the products prepared from different molar ratios of $Cu_{2-x}Se$ to $AgNO_3$. The diffraction peaks of CuAgSe, $Cu_{2-x}Se$, Ag_2Se, and Ag are marked with º, *, ♦, and ∆, respectively.

In order to better control the exchange process, silver acetate was selected to repeat the experiment and collected the intermediate products after different exchange times (i.e., 1 min, 2 min, 10 min, 20 min, and 60 min) (Figures 6.11-6.12). The results show that the complete transformation of $Cu_{2-x}Se$ NTs into CuAgSe NTs took 60 min due to the lower dissociation capability of silver acetate in ethanol compared to $AgNO_3$. The same intermediate products (Ag_2Se and Ag) formed at an early stage (i.e., 1 min and 2 min) and confirm the same exchange process as discussed above. Similar to the product prepared from $AgNO_3$, the morphology of CuAgSe NTs from silver acetate is well retained (Figure 6.14).

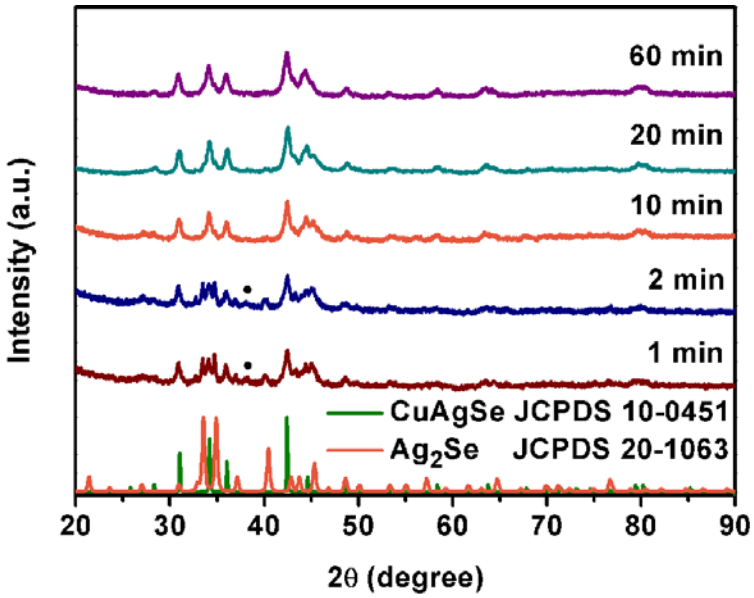

Figure 6.12 XRD patterns of CuAgSe samples prepared from silver acetate and collected after different reaction times. The diffraction peaks marked with • arise from Ag.

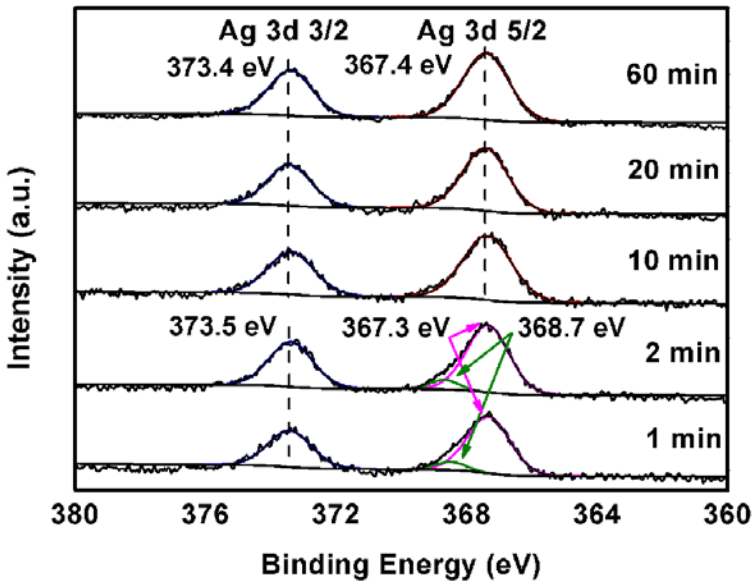

Figure 6.13 XPS spectra of Ag 3d in the samples prepared from silver acetate and collected after different reaction times.

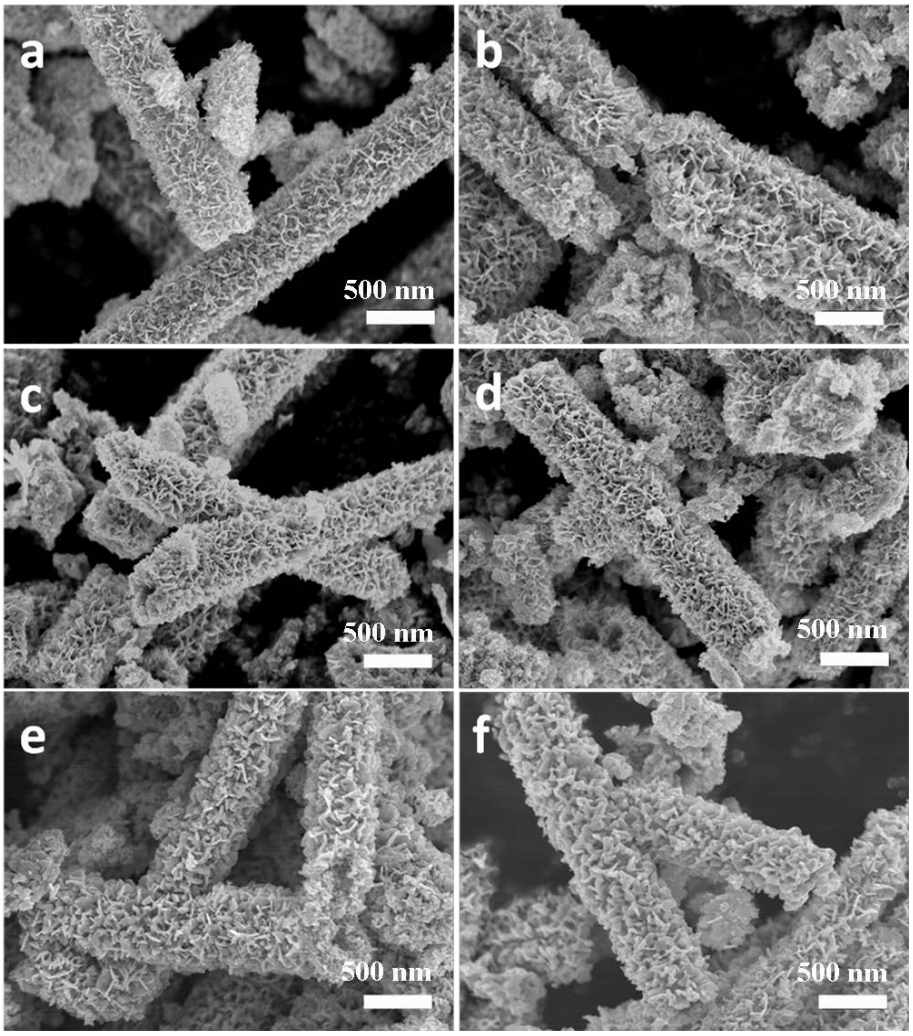

Figure 6.14 SEM images of NTs from cation exchange by silver actate that were collected after different reaction times: (a) 0 min; (b) 1 min; (c) 2 min; (d) 10 min; (e) 20 min, and (f) 60 min.

6.3.4 Performances of QDSSCs with CuAgSe CEs

As mentioned above, ternary CuAgSe might exhibit better electrochemical performance than its binary counterparts. To evaluate their electrocatalytic activity, the above resultant 1D/2D CuAgSe NTs were fabricated into CEs and then assembled with

CdS/CdSe QD co-sensitized photoanodes to construct QDSSC devices containing polysulfide electrolyte. Their electrocatalytic activities were compared with those of CEs fabricated from $Cu_{2-x}Se$ NTs and the noble-metal Au under the same conditions.[35-36] The average photovoltaic performance parameters are extracted in Table 6.1. Compared to the $Cu_{2-x}Se$ NT CE and the Au CE, QDSSCs incorporating CuAgSe NT CEs delivered a larger short-circuit density (J_{sc}) of 17.57 mA cm^{-2}, which indicates the fast reduction of S_n^{2-} to nS^{2-}. In addition, the remarkable enhancement of the open-circuit voltage (V_{oc}) of 581 mV, as well as the fill factor (*FF*) of 55.0 %, can be ascribed to the better electrical conductivity and thus suppressed charge recombination [Figure 6.15(a)]. Figure 6.15(b) shows the IPCE spectra of typical QDSSCs based on the three different CEs. Compared with both Au and $Cu_{2-x}Se$ NT CEs, the IPCE profile of QDSSCs employing the CuAgSe NT CE is higher over the entire wavelength region. This is consistent with the achieved J_{sc}. The significant increase in IPCE further verified that CuAgSe NTs possess both super catalytic activity and high electrical conductivity.

For understanding the improved QDSSC performance, EIS and Tafel polarization measurements were carried out using dummy cells assembled with two identical electrodes. Figure 6.15(c) shows the Nyquist plots for dummy cells with different CEs. The inset equivalent circuit includes the series resistance (R_s), charge transfer resistance (R_{ct}), and Warburg diffusion impedance (Z_w). The smaller these resistances are, the better the electrocatalytic activity of the CEs will be.[37-38] The R_s of the CuAgSe CE (10.8 Ω) is

smaller than those of the $Cu_{2-x}Se$ CE (12.9 Ω) and the Au CE (16.0 Ω), indicating the superior electrical conductivity of CuAgSe. Moreover, the CuAgSe CE has the smallest charge transfer resistance (R_{ct}) (0.67 Ω compared to 0.81 Ω for the $Cu_{2-x}Se$ CE and 42.43 Ω for the Au CE), which means that the CuAgSe CE has the best electrocatalytic activity towards the reduction of polysulfide among the three CEs. This is consistent with the J_{sc} values in the order of CuAgSe CE (17.57 mA cm^{-2}) > $Cu_{2-x}Se$ CE (17.13 mA cm^{-2}) > Au CE (13.34 mA cm^{-2}). The smallest Warburg diffusion impedance (Z_w) of the CuAgSe CE (4.17 Ω) reveals the efficient diffusion of polysulfide electrolyte. The highest *FF* of the QDSSCs with the CuAgSe CE can be attributed to the smallest Z_w as well as the R_s. Figure 6.15(d) shows the logarithmic current density (log *J*) as a function of the voltage (*U*) for the oxidation/reduction of polysulfide to sulfide. The slopes of the anodic and cathodic branches are in the order of CuAgSe NT, followed by $Cu_{2-x}Se$ NT, followed by Au. The larger slope for the CuAgSe NT indicates the larger exchange current density, which is consistent with the EIS. The better electrochemical performance of CuAgSe CE than $Cu_{2-x}Se$ CE is due to the higher mobility of both Cu^+ and Ag^+ ions in the CuAgSe NTs. The higher conversion efficiency of QDSSCs containing CuAgSe NTs and $Cu_{2-x}Se$ NTs as CEs is attributed to the higher stability of metal selenides in polysulfide electrolyte than that of the Au CE, because they retain good conductivity by avoiding corrosion and passivation.

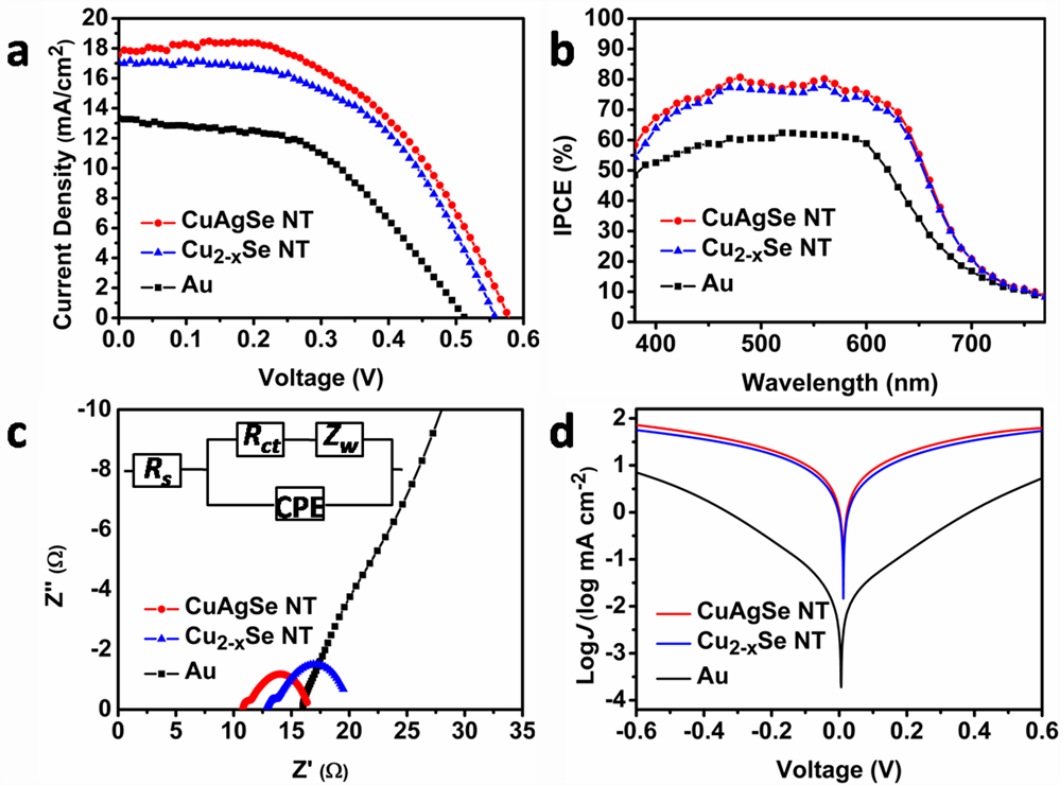

Figure 6.15 (a) The photocurrent density-voltage (*J*-*V*) curves and (b) IPCE spectra of QDSSCs with different CEs. (c) Nyquist plots of the symmetrical dummy cells fabricated with three CEs; the inset shows the equivalent circuit. (d) Tafel polarization of different dummy cells that are the same as those used for the EIS measurements.

The superior electrical conductivity and electrocatalytic activity of CuAgSe NTs to $Cu_{2-x}Se$ NTs led to an enhancement in power conversion efficiency of QDSSCs made with CuAgSe CE (η = 5.61 %) in comparison with that made with $Cu_{2-x}Se$ CE (η = 5.19 %). It should be noted that these values are lower than last chapter reports, due to the fact that photoelectrodes used in the current chapter are made from commercial TiO_2 nanoparticles rather than porous TiO_2 nanosheets, which could effectively scatter the

incident light and improve the conversion efficiency.[39] The use of commercial TiO_2 nanoparticles would be important for evaluating the practical application of our 1D/2D CuAgSe NTs.

Table 6.1 Photovoltaic parameters of QDSSCs with different CEs.

CEs	V_{oc} (mV)	J_{sc} (mA cm^{-2})	FF (%)	η (%)	R_s (Ω)	R_{ct} (Ω)	Z_w (Ω)
CuAgSe NT	581	17.57	55.0	5.61	10.8	0.67	4.17
$Cu_{2-x}Se$ NT	559	17.13	54.2	5.19	12.9	0.81	4.81
Au	507	13.34	49.1	3.32	16.0	42.43	72.13

6.4 Conclusions

In summary, 1D/2D pure ternary CuAgSe NTs were successfully prepared from $Cu_{2-x}Se$ NTs by cation exchange with silver nitrate (or silver acetate) at room temperature within a short time. The fast cation exchange is owing to the ionic characteristics of

copper/silver chalcogenides, and the strong capability of copper ions and silver ions for diffusion into/out of the lattice. The CuAgSe NTs with designed architecture have been used to fabricate CEs for QDSSCs, showing better electrochemical performance and higher conversion efficiency (η = 5.61 %) than original $Cu_{2-x}Se$ NT CE (η = 5.19 %) and Au CE (η = 3.32 %). This research not only opens up a new way for designing more effective CE catalysts for highly efficient QDSSCs, but also provides a facile method to fabricate designed architectural nanostructures of ternary selenides for diverse applications.

References

[1] Xu, J.; Lee, C. S.; Tang, Y. B.; Chen, X.; Chen, Z. H.; Zhang, W. J.; Lee, S. T.; Zhang, W. X.; Yang, Z. H. *ACS Nano* **2010**, *4*, 1845.

[2] Bi, W. T.; Zhou, M.; Ma, Z. Y.; Zhang, H. Y.; Yu, J. B.; Xie, Y. *Chem. Commun.* **2012**, *48*, 9162.

[3] Mukherjee, B.; Peterson, A.; Subramanian, V. *Chem. Commun.* **2012**, *48*, 2415.

[4] Lieber, C. M.; Wang, Z. L. *MRS Bull.* **2007**, *32*, 99.

[5] Zhang, G. Q.; Xia, B. Y.; Xiao, C.; Yu, L.; Wang, X.; Xie, Y.; Lou, X. W. *Angew. Chem., Int. Edit.* **2013**, *52*, 8643.

[6] Fang, C. X.; Zhang, S. Y.; Zuo, P. F.; Wei, W.; Jin, B. K.; Wu, J. Y.; Tian, Y. P. *J. Cryst. Growth* **2009**, *311*, 2345.

[7] Neshkova, M. T.; Nikolova, V. D.; Bond, A. M.; Petrov, V. *Electrochim. Acta* **2005**, *50*, 5606.

[8] Peng, S. J.; Zhang, T. R.; Li, L. L.; Shen, C.; Cheng, F. Y.; Srinivasan, M.; Yan, Q. Y.; Ramakrishna, S.; Chen, J. *Nano Energy* **2015**, *16*, 163.

[9] Earley, J. W. *Am. Mineral.* **1950**, *35*, 345.

[10] Frueh, A. J.; Czamanke, G. K.; Knight, C. H. *Z. Kristallogr.* **1957**, *108*, 389.

[11] Ishiwata, S.; Shiomi, Y.; Lee, J. S.; Bahramy, M. S.; Suzuki, T.; Uchida, M.; Arita, R.; Taguchi, Y.; Tokura, Y. *Nat. Mater.* **2013**, *12*, 512.

[12] Hong, A. J.; Li, T.; Zhu, H. X.; Zhou, X. H.; He, Q. Y.; Liu, W. S.; Yan, Z. B.; Liu, J. M.; Ren, Z. F. *Solid State Ionics* **2014**, *261*, 21.

[13] Baikulov, R. B.; Asadov, Y. G. *Inorg. Mater.* **2005**, *41*, 338.

[14] Han, C.; Sun, Q.; Cheng, Z. X.; Wang, J. L.; Li, Z.; Lu, G. Q.; Dou, S. X. *J. Am. Chem. Soc.* **2014**, *136*, 17626.

[15] Gao, Y. H.; Zheng, Z.; Tian, Y. P.; Zhang, Y. D.; Zhang, Y. G. *Eur. J. Inorg. Chem.* **2011**, *27*, 4198.

[16] Gupta, S.; Kershaw, S. V.; Rogach, A. L. *Adv. Mater.* **2013**, *25*, 6923.

[17] Ha, D. H.; Caldwell, A. H.; Ward, M. J.; Honrao, S.; Mathew, K.; Hovden, R.; Koker, M. A.; Muller, D. A.; Hennig, H. G.; Robinson, R. D. *Nano Lett.* **2014**, *14*, 7090.

[18] Stam, W.; Akkerman, Q. A.; Ke, X. X.; Huis, M. A.; Bals, S.; Donega, C. M.

Chem. Mater. **2015**, *27*, 283.

[19] Trizio, L. D.; Li, H. B.; Casu, A.; Genovese, A.; Sathya, A.; Messina, G. C.; Manna, L. *J. Am. Chem. Soc.* **2014**, *136*, 16277.

[20] Son, D. H.; Hughes, S. M.; Yin, Y. D.; Alivisatos, A. P. *Science* **2004**, *306*, 1009.

[21] Kriegel, I.; Rodriguez-Fernandez, J.; Wisnet, A.; Zhang, H.; Waurisch, C.; Eychmuller, A.; Dubavik, A.; Govorov, A. O.; Feldmann, J. *ACS Nano* **2013**, *7*, 4367.

[22] Xiong, S. L.; Zeng, H. C. *Angew. Chem., Int. Edit.* **2012**, *51*, 949.

[23] Wu, X. J.; Huang, X.; Liu, J. Q.; Li, H.; Yang, J.; Li, B.; Huang, W.; Zhang, H. *Angew. Chem., Int. Edit.* **2014**, *53*, 5083.

[24] Robinson, R. D.; Sadtler, B.; Demchenko, D. O.; Erdonmez, C. K.; Wang, L. W.; Alivisatos, A. P. *Science* **2007**, *317*, 355.

[25] Tang, J. Y.; Huo, Z. Y.; Brittman, S.; Gao, H. W.; Yang, P. D. *Nat. Nanotechnol.* **2011**, *6*, 568.

[26] Li, H. B.; Brescia, R.; Krahne, R.; Bertoni, G.; Alcocer, M. J. P.; D'Andrea, C.; Scotognella, F.; Tassone, F.; Zanella, M.; De Giorgi, M.; Manna, L. *ACS Nano* **2012**, *6*, 1637.

[27] Li, H. B.; Brescia, R.; Povia, M.; Prato, M.; Bertoni, G.; Manna, L.; Moreels, I. *J. Am. Chem. Soc.* **2013**, *135*, 12270.

[28] Zhang, D. D.; Wong, A. B.; Yu, Y.; Brittman, S.; Sun, J. W.; Fu, A.; Beberwyck,

B.; Alivisatos, A. P.; Yang, P. D. *J. Am. Chem. Soc.* **2014**, *136*, 17430.

[29] Miszta, K.; Brescia, R.; Prato, M.; Bertoni, G.; Marras, S.; Xie, Y.; Ghosh, S.; Kim, M. R.; Manna, L. *J. Am. Chem. Soc.* **2014**, *136*, 9061.

[30] Riha, S. C.; Johnson, D. C.; Prieto, A. L. *J. Am. Chem. Soc.* **2011**, *133*, 1383.

[31] Mi, L. W.; Wei, W. T.; Zheng, Z.; Zhu, G. S.; Hou, H. W.; Chen, W. H.; Guan, X. X. *Nanoscale* **2014**, *6*, 1124.

[32] Lesnyak, V.; Brescia, R.; Messina, G. C.; Manna, L. *J. Am. Chem. Soc.* **2015**, *137*, 9315.

[33] Gronvold, F.; Stolen, S.; Semenov, Y. *Thermochim. Acta* **2003**, *399*, 213.

[34] K. C. Mills, Thermodynamic Data for Inorganic Sulphides, Selenides and Tellurides, Butterworths, London, **1974**.

[35] Bai, Y.; Xing, Z.; Yu, H.; Li, Z.; Amal, R.; Wang, L. Z. *ACS Appl. Mater. Interfaces* **2013**, *5*, 12058.

[36] Bai, Y.; Yu, H.; Li, Z.; Amal, R.; Lu, G. Q.; Wang, L. Z. *Adv. Mater.* **2012**, *24*, 5850.

[37] Lee, J. K.; Son, D. Y.; Ahn, T. K.; Shin, H. W.; Kim, I. Y.; Hwang, S. J.; Ko, M. J.; Sul, S.; Han, H.; Park, N. G. *Scientific Reports* **2013**, *3*, 1.

[38] Santra, P. K.; Kamat, P. V. *J. Am. Chem. Soc.* **2012**, *134*, 2508.

[39] Deepak, T. G.; Anjusree, G. S.; Thomas, S.; Arun, T. A.; Nair, S. V.; Nair, A. S. *RSC Adv.* **2014**, 4, 17615.

CHAPTER 7 Conclusions and Recommendations

7.1 Conclusions

Binary and ternary copper chalcogenides applied for thermoelectric conversion and QDSSCs have been researched in the above chapters. The entire doctoral work is focused on two energy conversion applications: design and synthesis of a large scale of morphology-controlled copper selenide nanostructures for thermoelectric conversion and copper sulfide, copper selenide, and copper silver selenide NTs with hierarchical architecture replacing noble metals as CEs of QDSSCs. Based on the summaries of the above studies in the previous chapters, following general conclusions are given below:

7.1.1 Copper selenide nanostructures for thermoelectric conversion

Surfactant-free $Cu_{2-x}Se$ NW bundles with lengths of tens of micrometers and diameters of 100–300 nm have been synthesized on a large scale by an aqueous approach. The NW bundles are composed of many thin $Cu_{2-x}Se$ NWs. The evolution of the morphology shows that the formation of $Cu_{2-x}Se$ nanobundles arises from the assembly of CuSe nanoplates induced by water evaporation, accompanied by the self-redox reactions of CuSe. The formation of $Cu_{2-x}Se$ nanobundles is strongly influenced by the molar ratio of sodium hydroxide to selenium powder, and the molar ratio of selenium powder to copper nitrate. The resultant $Cu_{2-x}Se$ nanobundles were sintered into pellets and tested for thermoelectric application in comparison with commercial Cu_2Se powder. The results

show that the synthetic sample has a temperature-dependent *ZT* comparable to that of the commercial sample, which reaches to 0.29 at 480 ˚C.

Grams of $Cu_{2-x}Se$ nanostructures have been synthesized by a one-pot reaction of commercial copper powder with Se powder in the presence of 2-mercaptoethanol. The resultant nanostructures were treated with hydrazine solution to remove adsorbed surface ligands. The hydrazine treatment destroyed the sheet-like structure, and resulted in pristine $Cu_{2-x}Se$ nanoparticles, which were sintered into a pellet. Their thermoelectric properties were measured in comparison with commercial Cu_2Se powder under the same conditions. Their thermoelectric properties show that the $Cu_{2-x}Se$ sample has a similar temperature-dependent *ZT* (0.28 at 480 ˚C) to that of the commercial sample. The $Cu_{2-x}Se$ sample retained the same crystal structure and morphology after SPS sintering and thermoelectric measurements at high temperature.

This part of work indeed provides alternative simple methods to fabricate large-scale copper selenide nanostructures for thermoelectric applications. The results demonstrated nano grains are the key point to reduce lattice thermal conductivity, by enhancing phonon scattering. Meanwhile, the second preparation method for nanostructured copper selenide can retain crystal structure without phase change after SPS sintering and thermoelectric measurement at high temperature, which is distinguished from ball-milling method and elements melting method. However, the enhancement of *ZT* is not only decided by the reduction in thermal conductivity, but also by the concomitant reduction in the power

factor. Another problem is that there are inevitable small holes inside nanostructured materials after SPS sintering, which might result in overestimating *ZT* of materials. Thus, the highest *ZT* of materials is not the only purpose in thermoelectric application, instead, the research about stable crystal structures, accurate density, and steady specific heat capacity of thermoelectric materials is more meaningful in this area.

7.1.2 Copper chalcogenide NTs as CEs for QDSSCs

$Cu_{2-x}E$ (E = S, Se) NTs with a hierarchical architecture were successfully synthesized at room temperature through the reaction of Cu NWs with sulfur or selenium powder in the presence of thiol ligands under catalysis by NaOH. The theoretical calculation confirmed the reaction mechanism. Cu NWs served as sacrificial templates during the formation of the NTs. NaOH played a role in deprotonating –SH groups of thiol ligands and helped to dissolve of chalcogen precursors. Comprehensive investigations on the effects of reaction parameters demonstrate that this room-temperature reaction can occur as long as the thiol groups are deprotonated. The resultant $Cu_{2-x}E$ (E =S, Se) NTs have been used to fabricate high-performance CEs for QDSSCs, showing a higher conversion efficiency (up to 5.02% and 6.25%, respectively) than ever reported for Au CEs (η = 2.94%).

1D/2D ternary CuAgSe NTs were successfully prepared from $Cu_{2-x}Se$ NTs by cation exchange with silver nitrate (or silver acetate) at room temperature within a short time. The fast cation exchange is owing to the ionic characteristics of copper/silver

chalcogenides, and the strong capability of copper ions and silver ions for diffusion into/out of the lattice. The CuAgSe NTs with designed architecture have been used to fabricate CEs for QDSSCs, showing better electrochemical performance and higher conversion efficiency (η = 5.61%) than original $Cu_{2-x}Se$ NT CE (η = 5.19%) and Au CE (η = 3.32%). It should be noted that these efficiency values are lower than previous results (conversion efficiency of $Cu_{2-x}Se$ NT CE is 6.25%), due to the fact that photoelectrodes used in the current work are made from commercial TiO_2 nanoparticles rather than porous TiO_2 nanosheets, which could effectively scatter the incident light and improve the conversion efficiency. The use of commercial TiO_2 nanoparticles would be important for evaluating the practical application of our 1D/2D CuAgSe NTs.

In conclusion, binary $Cu_{2-x}E$ (E = S, Se) NTs and ternary CuAgSe NTs with a hierarchical architecture have been used to fabricate CEs for QDSSCs, showing better electrochemical performance and higher conversion efficiency than noble metal Au CE, which is because copper chalcogenides CEs show lower resistance and higher electrocatalytic activity towards the redox reaction of polysulfide electrolyte and larger designed surface area than noble metal Au CE.

7.2 Recommendations

Based on my doctoral work that has been focused on copper selenide nanostructures in thermoelectric conversion and binary/ternary copper chalcogenide NTs as CEs in

QDSSCs, there are some challenges to be solved: first, how to enhance the Seebeck coefficient in the terms of increasing the electrical conductivity and decreasing the overall thermal conductivity of $Cu_{2-x}Se$ nanostructures; second, what will affect the conversion efficiency when tuning the size or ordering the array of copper chalcogenide NTs. As copper chalcogenides have various applications, whether different sizes of copper selenide nanostructures can be explored for electrocatalytic activity toward the ORR and serve as novel nanotheranostic agent.

APPENDIX A: List of Publications

1. **X. Q. Chen**, Z. Li*, and S. X. Dou, "Ambient Facile Synthesis of Gram-Scale Copper Selenide Nanostructures from Commercial Copper and Selenium Powder", ***ACS Applied Materials & Interfaces***, 2015, 7, 13295-13302.
2. **X. Q. Chen**, Z. Li*, Y. Bai, Q. Sun, L. Z. Wang* and S. X. Dou, "Room-Temperature Synthesis of $Cu_{2-x}E$ (E=S, Se) Nanotubes with Hierarchical Architecture as High-Performance Counter Electrodes of Quantum-Dot-Sensitized Solar Cells", ***Chemistry − A European Journal***, 2015, 21, 1055-1063. (As the back cover of the issue and hot paper)
3. **X. Q. Chen**, Z. Li*, J. P. Yang, Q. Sun and S. X. Dou, "Aqueous Route for Preparation of Surfactant-Free Copper Selenide Nanowires", ***Journal of Colloid and Interface Science***, 2015, 442, 140-146.
4. **X. Q. Chen**, Y. Bai, Z. Li*, L. Z. Wang, and S. X. Dou, "Ambient Synthesis of One-Dimensional/Two-Dimensional CuAgSe Ternary Nanotubes as Counter Electrodes of Quantum-Dot-Sensitized Solar Cells" ***ChemPlusChem***, 2016, DOI: 10.1002/cplu.201500466. (As the front cover of the issue and cover profile)
5. M. Tan* and **X. Q. Chen**, "Growth Mechanism of Single Crystal Nanowires of fcc Metals (Ag, Cu, Ni) and hcp Metal (Co) Electrodeposited", ***Journal of the Electrochemical Society***, 2012, 159, K15-K20.
6. Y. Bai, C. Han, **X. Q. Chen**, H. Yu, X. Zong, Z. Li*, and L. Z. Wang*, "Boosting the Efficiency of Quantum Dot Sensitized Solar Cells up to 7.11% through Simultaneous Engineering of Photocathode and Photoanode", ***Nano Energy***, 2015, 13, 609-619.
7. X. Y. Hu, B. J. Heng, **X. Q. Chen**, B. X. Wang, D. M. Sun, Y. M. Sun, W. Zhou and Y. W. Tang*, "Ultralong Porous ZnO Nanobelt Arrays Grown Directly on Fluorine-doped SnO_2 Substrate for Dye-Sensitized Solar Cells", ***Journal of Power Sources***, 2012, 17, 120-127.
8. J. P. Yang*, T. F. Zhou, R. Zhu, **X. Q. Chen**, Z. P. Guo*, J. W. Fan, H. K. Liu, and W. X. Zhang*, "Highly Ordered Dual Porosity Mesoporous Cobalt Oxide for Sodium Ion Batteries", ***Advanced Materials Interfaces***, 2015, 1500464 (1-7).
9. T. Mehmood, B. S. Khan, A. Mukhtar, **X. Q. Chen**, P. Yi and M. Tan*, "Mechanism for Formation of fcc-Cobalt Nanowires in Electrodeposition at Ambient

Temperature", ***Materials Letters***, 2014, 130, 256–258.

10. B. J. Heng, T. Xiao, W. Tao, X. Y. Hu, **X. Q. Chen**, B. X. Wang, D. M. Sun and Y. W. Tang*, "Zn Doping-Induced Shape Evolution of Microcrystals: The Case of Cuprous Oxide", ***Crystal Growth & Design***, 2012, 12, 3998–4005.
11. X. Y. Hu, T. Xiao, W. Huang, W. Tao, B. J. Heng, **X. Q. Chen** and Y. W. Tang*, "Synthesis, Characterization of Core–Shell Carbon-Coated $CaSnO_3$ Nanotubes and Their Performance as Anode of Lithium Ion Battery", ***Applied Surface Science***, 2012, 258, 6177–6183.

APPENDIX B: Conferences Attended

1. Australian Nanotechnology Network Early Career Researcher Symposium, Melbourne, Australia, 2012, poster presentation.
2. 5th Australia-China Conference on Science, Technology and Education in conjunction with the 5th Australia-China Symposium for Materials Science, Wollongong, Australia, 2014, poster presentation.
3. Energy Future Conference, University of New South Wales (UNSW), Sydney, Australia, 2014, poster presentation.
4. 3rd Baosteel-Australia Joint Research and Development Centre Conference, UNSW, Sydney, Australia, 2015.
5. Nanomaterials for the Energy & Environment, France, 2015, oral presentation.

APPENDIX C: Awards Received

1. Faculty Top-up Scholarship from University of Wollongong.
2. Runner-up, 2014 AIIM HDR Seminar Competition.
3. 2014 Postgraduate Student Merit Award, Institute for Superconducting and Electronic Materials.
4. AIIM HDR Student Conference and International Travel Grants.
5. Winner, 2015 UOW Electron Microscopy Centre HDR Student Presentation Competition.